FABRICATION AND ELECTROMECHANICAL

STUDY OF SYMMETRIC TAPE ROUND (STAR) REBCO WIRES

A Dissertation

Presented to

the Faculty of the Department of Mechanical Engineering

University of Houston

In Partial Fulfillment

of the Requirements for the Degree

Doctor of Philosophy

in Mechanical Engineering

by

Wenbo Luo

May 2019

FABRICATION AND ELECTROMECHANICAL

STUDY OF SYMMETRIC TAPE ROUND (STAR) REBCO WIRES

____

Wenbo Luo

Approved:

____

Chair of the Committee
Venkat Selvamanickam, Professor,
Mechanical Engineering

Committee Members:

____

Dong Liu, Associate Professor,
Mechanical Engineering

____

Jae-Hyun Ryou, Associate Professor,
Mechanical Engineering

____

Yashashree Kulkarni, Associate Professor,
Mechanical Engineering

____

Jiming Bao, Associate Professor,
Electrical & Computer Engineering

____

Suresh K. Khator, Associate Dean,
Cullen College of Engineering

____

Pradeep Sharma, Professor and Chair,
Mechanical Engineering

Acknowledgments

I would like to express my utmost gratitude to my advisor, Prof. Venkat Selvamanickam, for providing me the opportunity to work in his group and complete the Ph.D. degree. His enthusiasm, persistence, and motivation have encouraged me countless times during the past four and half years. I also would like to thank him for his insightful suggestions and patient guidance, which helped me to overcome the difficulties in research. It has been an honor and pleasure to work with a mentor like him.

I would like to thank my committee members, Dr. Dong Liu, Dr. Jae-Hyun Ryou, Dr. Yashashree Kulkarni, Dr. Jiming Bao, for their valuable evaluations and comments on this dissertation.

My research results cannot be achieved without the help and support from the research scientists and colleagues in our research group, including Dr. Goran Majkic, Dr. Eduard Galstyan, Dr. Aixia Xu, Dr. Pavel Dutta, Dr. Monika Rathi, George Pope, Lazaro Saldana, Joanna Taormina, Dr. Meysam Heydari Gharahcheshmeh, Dr. Ying Gao, Dr. Yongkuan Li, Rudra Pratap, Vasish Mohan, Anis Ben Yahia, Yuan Zhang, Mehdi Kochat, Siwei Chen, Sicong Sun, Khatiwada Devendra, and Jithin Sai Sandra. Special thanks to Dr. Soumen Kar, Dr. Xiao-fen Li, and Dr. Xinwei Cai for their generous and invaluable help during the research. I also would like to thank Dr. Jan J Jaroszynski and Dr. Dmytro V Abraimov in National High Magnetic Field Laboratory for providing help during experiments.

In addition, I appreciate the Small Business Innovation Research funding for this research work, which is provided by the Office of Science in U.S. Department of Energy.

At last, I would like to express my deepest gratitude and love to my parents, Aihua Yu and Qiancong Luo, and my wife, Yixing Chen, for their endless love and support. It is impossible to complete my Ph.D. without their help and encouragement. I hope that I can make you proud.

FABRICATION AND ELECTROMECHANICAL

STUDY OF SYMMETRIC TAPE ROUND (STAR) REBCO WIRES

An Abstract

Of a

Dissertation

Presented to

the Faculty of the Department of Mechanical Engineering

University of Houston

In Partial Fulfillment

of the Requirements for the Degree

Doctor of Philosophy

in Mechanical Engineering

by

Wenbo Luo

May 2019

Abstract

High temperature superconducting (HTS) materials are essential for applications that require to operate at magnetic fields higher than 20 T. In commonly used HTS materials, Rare-Earth$_1$Ba$_2$Cu$_3$O$_{7-x}$ (REBCO) coated conductor is an attractive candidate because of its exceptional mechanical strength and high current carrying capability. Due to the planar geometry, the REBCO tapes are usually reformatted into wire forms. For specific compact accelerator applications such as Canted Cosine θ (CCT) coils, the existing REBCO wires cannot provide required J_e values at small bending diameters. Therefore, flexible REBCO wires that maintain high J_e values at small bending diameters are needed.

To improve the bending performance of REBCO tapes, the key is to reduce the distance between the REBCO layer and neutral axis. It can be achieved by reducing the thickness of Hastelloy substrate and depositing copper onto the REBCO side. The REBCO tapes that consist of a thin substrate and a copper layer with specific thickness on the REBCO side are called "symmetric tapes", as nearly the same bending strain is expected at each side of the REBCO layer. The fabrication process and optimization of symmetric tapes were discussed. With 22 μm substrates, symmetric tapes maintained 98% of the original I_c values at a 0.8 mm bending diameter.

On the basis of symmetric tapes, STAR wires were developed. A custom wire winding machine was built to produce long length STAR wires with constant quality. Parameters of STAR wire, including the wire former size, width of tape, and number of layers, were investigated in detail. The bending property and current carrying capabilities of STAR wires at 77 K and 4.2 K were analyzed. At 4.2 K in a 31.2 T background field, a J_e value of 299 A/mm^2, which was the highest reported value, was achieved. Other factors that influence the performance of STAR wires, such as the

terminal structure and interlayer resistance, were studied as well. The results exhibit the potential and feasibility of using STAR wires in compact accelerator applications at 4.2 K.

Table of Contents

Acknowledgments .... **v**

Abstract .... **vii**

Table of Contents .... **ix**

List of Figures .... **xiv**

List of Tables .... **xxi**

List of Abbreviations .... **xxiii**

Chapter 1. Introduction **1**

1.1 Overview of superconductivity 1

1.1.1 Critical values 1

1.1.2 Type I and type II superconductors 4

1.1.3 Superconductors used in applications 6

1.2 High temperature superconductors (HTSs) 8

1.2.1 BSCCO 8

1.2.2 REBCO 10

1.3 REBCO cables 13

1.3.1 RACC cables 13

1.3.2 TSTC cables 16

1.3.3 CORC cables 17

1.3.4 REBCO cable comparison 19

1.4 Dissertation objectives and outline 20

Chapter 2. STAR wire fabrication 22

2.1 REBCO tape grinding 22

2.1.1 Reel-to-reel tape grinding system 23

2.1.1.1 Grinding machine prototype 23

2.1.1.2 Four-wheel grinding system 24

2.1.2 Ground tape uniformity analysis 25

2.1.2.1 Ground tape thickness 25

2.1.3 Ground tape weak point examination 28

2.1.4 Improved reel-to-reel grinding process 31

2.2 REBCO tape laser slitting 33

2.2.1 Laser slitting platform 34

2.2.2 Laser slitting optimization 35

2.2.2.1 Slitting parameters 35

2.2.2.2 Laser slitting pattern 37

2.2.2.3 Tape edge SEM examination 38

2.3 Copper electroplating 39

2.3.1 Reel-to-reel electroplating system 39

2.3.2 Copper quality control 42
2.3.2.1 Copper thickness 42
2.3.2.2 Shield design for single-side electroplating 45
2.4 STAR wire winding 47
2.4.1 Manual winding process 47
2.4.1.1 Wire without terminal 47
2.4.1.2 Wire with terminals 51
2.4.2 Automatic winding process 53
2.4.2.1 Automatic winding machine 53
2.4.2.2 Terminal fabrication in automatic winding 54
Chapter 3. Electromechanical properties of symmetric tape 58
3.1 Symmetric tape structure 58
3.1.1 Bending strain and neutral axis in REBCO tapes 58
3.1.2 Bending tests of tapes with different configurations 62
3.1.2.1 Bending test under compressive strain 62
3.1.2.2 Bending test under tensile strain 65
3.2 Symmetric tape parameter optimization 67
3.2.1 Optimization of copper stabilizer thickness 67
3.2.2 Optimization of twist pitch 72

Chapter 4. STAR wire electrical performance and analysis 76

4.1 77 K self-field performance of STAR wires 76

4.1.1 Manually-wound fixed-tape-width structure 76

4.1.1.1 Layer-wise performance in straight form.. 76

4.1.1.2 Bending performance... 79

4.1.2 Variable-tape-width structure 82

4.1.2.1 Tape width configurations 82

4.1.2.2 Performance in straight and bent forms 84

4.1.2.3 Analysis of longitudinal and circumferential stresses in bending 86

4.1.3 Multiple-tapes-in-a-single-layer (MTISL) structure 92

4.1.4 Optimal-tape-width structure.. 95

4.1.5 10 m STAR wire 99

4.1.6 Summary 103

4.2 In-field performance of STAR wires 104

4.2.1 Single-layer STAR wire performance.. 104

4.2.2 Performance of multi-layer STAR wires without indium filling 106

4.2.2.1 Sample holder structure and STAR wire specifications 106

4.2.2.2 Test results at 4.2 K in background magnetic fields 109

4.2.2.3 Analysis of degradation in high magnetic fields 113

4.2.3 Performance of multi-layer STAR wires with indium filling 115

4.2.3.1 STAR wire specifications 115

4.2.3.2 Test results at 4.2 K in background magnetic fields 117

4.2.3.3 Repeatability test and temperature changes of STAR wires 120

4.2.3.4 Summary 121

4.3 Resistance and defect detection of STAR wires 122

4.3.1 Terminal resistance of STAR wires 122

4.3.2 Inter-layer resistance of STAR wires 127

4.3.3 STAR wire defect test 130

4.3.3.1 Section-by-section *I-V* method 130

4.3.3.2 Magnetic bridging method 132

Chapter 5. Conclusions and future works 136

5.1 Conclusions 136

5.2 Future work 138

References 140

List of Figures

Fig. 1-1 Definition of critical temperature $T_{c,50}$ 2

Fig. 1-2 Critical surfaces of several superconductors 3

Fig. 1-3 Schematic diagram of temperature and magnetic field dependence of type I and type II superconductors 4

Fig. 1-4 Timeline of discovery of superconductors 6

Fig. 1-5 Outline of PIT method in Bi-2223 fabrication 8

Fig. 1-6 Cross-section photograph of a Bi-2212 wire 9

Fig. 1-7 Lattice structure of yttrium barium copper oxide 10

Fig. 1-8 Schematic layout of a REBCO tape from Superpower 11

Fig. 1-9 Comparison of field dependence of J_e; several superconductors are included 12

Fig. 1-10 A dummy RACC made with copper and stainless tapes 14

Fig. 1-11 Damaged edge of a RACC cable after in-field measurement 15

Fig. 1-12 Twisted Stacked Tape Cables (TSTC) 16

Fig. 1-13 Photograph of a 2 mm wide REBCO conductor with 10 full twists 18

Fig. 1-14 Conductor on Round Core (CORC) cable 18

Fig. 2-1 A flowchart of the STAR wire fabrication process 22

Fig. 2-2 Reel-to-reel grinding machine prototype 23

Fig. 2-3 Surface change of the back side of REBCO tape 24

Fig. 2-4 Four-wheel reel-to-reel grinding system 25

Fig. 2-5 Plot of tape thickness versus grinding turns 26

Fig. 2-6 Tape thickness at three different points along the length 27

Fig. 2-7 25 m tape I_c comparison before and after grinding; the circled region was examined. 28

Fig. 2-8 Magnetic field plot of weak region by SHPM 29

Fig. 2-9 SEM examination of weak region of thin tape 30

Fig. 2-10 EDX results at two areas in chipped region 30

Fig. 2-11 Thickness of 65 m ground tape under new grinding parameters 31

Fig. 2-12 Calculated I_c value of 50 m tape after grinding 32

Fig. 2-13 SHPM trapped magnetic field plots of two slitting methods 33

Fig. 2-14 Laser slitting platform 34

Fig. 2-15 Three laser slitting patterns 37

Fig. 2-16 SEM image of the edge of sample S9-1 39

Fig. 2-17 Reel-to-reel electroplating system 40

Fig. 2-18 Optical micrographs of surface of copper electroplated with two different pH solutions 42

Fig. 2-19 Tape thickness at different electroplating current densities 43

Fig. 2-20 Rough edge of electroplated tape with simple plate cover 43

Fig. 2-21 Simulation of current density with Teflon plate cover 44

Fig. 2-22 Teflon shield for single-side electroplating 45

Fig. 2-23 Current density distribution with modified Teflon shield 46

Fig. 2-24 Tape thickness of electroplated tape with improved shield 46

Fig. 2-25 STAR wire manual winding platform 48

Fig. 2-26 Two typical 6-layer short STAR wire 49

Fig. 2-27 *I-V* plots of each tape in Wire-A 50

Fig. 2-28 *I-V* plots of each tape in Wire-B 51

Fig. 2-29 Two terminal structures used in manual winding process 52

Fig. 2-30 Manually-wound 1 m STAR wire 52

Fig. 2-31 Automatic winding machine 54

Fig. 2-32 STAR wire end connection structures 55

Fig. 2-33 Comparison of STAR wire ends 56

Fig. 2-34 Wire end remaking steps 56

Fig. 3-1 Layer structure of Superpower SF12050 tape (not to scale) 59

Fig. 3-2 REBCO tape bending test on a 9.5 mm diameter G10 rod 60

Fig. 3-3 I_c dependence of SF12050 tape on bending diameter 61

Fig. 3-4 Schematic structure of samples for bending test (not to scale) 62

Fig. 3-5 I_c dependence of different tape configurations on bending diameter 63

Fig. 3-6 Cross-section of a symmetric tape 65

Fig. 3-7 Comparison of I_c dependence on bending diameter under tensile and compressive strain 66

Fig. 3-8 Photograph of a single-layer STAR wire for copper optimization 68

Fig. 3-9 *I-V* curves at 77K, self-field of STAR wires made of tapes with initial thickness of 24 μm.. 69

Fig. 3-10 I_c retention versus copper thickness of tapes with different initial thicknesses 70

Fig. 3-11 Optimized copper thickness and corresponding maximum I_c retention 71

Fig. 3-12 Short STAR wires with different twist pitches 73

Fig. 3-13 I_c retention dependence on twist pitch 74

Fig. 4-1 A manually-wound STAR wire with conical terminals 77

Fig. 4-2 *I-V* curves of manually-wound wire at 77 K in self-field....................................... 78

Fig. 4-3 The manually-wound STAR wire at a 5 cm bending diameter............................... 79

Fig. 4-4 *E-I* characteristics of manually-wound STAR wire at different bending diameters 80

Fig. 4-5 Zoomed-in *E-I* characteristics of the manually-wound STAR wire in log-log scale80

Fig. 4-6 Finite elemental model of a bent STAR wire and its magnetic field distribution.... 81

Fig. 4-7 Relationship between the twist pitch, wire diameter, and tape width 83

Fig. 4-8 *E-I* characteristics of variable-tape-width STAR wire of configuration-1 84

Fig. 4-9 *E-I* characteristics of variable-tape-width STAR wire of configuration-2 85

Fig. 4-10 Stresses induced during tube bending 87

Fig. 4-11 Stress function comparison of two layers in STAR wire..................................... 89

Fig. 4-12 Variable-tape-width STAR wire in configuration-2 in bent form; delamination happened at innermost point 89

Fig. 4-13 The fifth and sixth layers of MTISL STAR wire 94

Fig. 4-14 *E-I* characteristics of MTISL STAR wire... 94

Fig. 4-15 Copper terminals with large contacting area and low resistance 97

Fig. 4-16 *E-I* characteristics of the optimal-tape-width structure STAR wires 97

Fig. 4-17 Trapped field maps of SHPM and the corresponding calculated I_c of a 2.5 mm wide tape 99

Fig. 4-18 10 m long STAR wire 101

Fig. 4-19 *E-I* characteristics of the 10 m STAR wire.. 102

Fig. 4-20 Angular dependence of I_c of a single-layer STAR wire at 77K, 1T and 30K, 3T 105

Fig. 4-21 Magnetic field dependence of I_c of a single-layer STAR wire in fields perpendicular to the wire axis 106

Fig. 4-22 G-10 sample support with a STAR wire mounted on it 107

Fig. 4-23 Cross-section photographs of 6-layer and 8-layer STAR wires.......................... 108

Fig. 4-24 Magnetic field dependence of I_c of STAR wires without indium filling between 16 and 31.2 T at 4.2 K 110

Fig. 4-25 Magnetic field dependence of J_e of STAR wires without indium filling between 16 and 31.2 T at 4.2 K 110

Fig. 4-26 Burnt STAR wire R2 after testing at a 31.2 T background field......................... 112

Fig. 4-27 Imprints found on the outmost layer of R1 after in-field tests 113

Fig. 4-28 Calculated maximum Lorentz forces applied on single layer of tape with 1 cm projection length.. 114

Fig. 4-29 Location of temperature sensors 117

Fig. 4-30 Magnetic field dependence of I_c of STAR wires with indium filling between 18 and 31.2 T at 4.2 K... 118

Fig. 4-31 Magnetic field dependence of J_e of STAR wires with indium filling between 18 and 31.2 T at 4.2 K... 118

Fig. 4-32 Repeatability test of R7 at 31.2 T background field.. 120

Fig. 4-33 Temperature change of R9 and R10; sensor was installed on the copper terminal of R9 and in the center part of R10.. 121

Fig. 4-34 Three different terminal structures measured in resistance tests......................... 123

Fig. 4-35 Schematic diagram of current distribution in a 3-layer STAR wire, not to scale 124

Fig. 4-36 Unwound STAR wire for direct measurement of the terminal resistance 124

Fig. 4-37 Resistance between pairs of tape in a STAR wire with tube terminal................. 125

Fig. 4-38 *I-V* characteristics of a STAR wire used to determine terminal resistance.......... 126

Fig. 4-39 Four STAR wires used for interlayer resistance test 127

Fig. 4-40 Schematic diagram of locations of voltage tap on 10 m STAR wire 130

Fig. 4-41 Section-by-section *I-V* characteristics of 10 m STAR wire................................ 131

Fig. 4-42 Section I_c of the 10 m STAR wire.. 132

Fig. 4-43 Schematic plot of magnetic bridging method 133

Fig. 4-44 Magnetic bridging measurement on a STAR wire 134

Fig. 4-45 Comparison of estimated I_c and measured I_c under magnetic bridging............... 135

List of Tables

Tab. 1-1 Critical temperature, critical magnetic field, and target fields of commonly used superconductors 7

Tab. 1-2 Properties comparison of REBCO cables 19

Tab. 2-1 25 m tape grinding parameters 25

Tab. 2-2 Tape edge roughness with different laser slitting parameters 36

Tab. 2-3 Tape edge roughness of different laser slitting patterns 37

Tab. 2-4 100 L electroplating solution formula 41

Tab. 3-1 Thickness of copper layers and Hastelloy substrate 62

Tab. 3-2 Electroplating parameters of tapes used for copper thickness optimization 67

Tab. 4-1 Layer-wise electrical performance of manually-wound STAR wire 77

Tab. 4-2 Maximum tape width and two tape width configurations calculated by typical wire diameters 83

Tab. 4-3 Adjusted maximum tape widths at different bending diameters (in mm) 91

Tab. 4-4 Tape number and width of a MTISL structure STAR wire 93

Tab. 4-5 Specifications of optimal-tape-width structure wires 96

Tab. 4-6 Test results and retention of optimal-tape-width structure STAR wires 98

Tab. 4-7 Specifications of the 10 m STAR wire 100

Tab. 4-8 Specifications of STAR wires without indium filling 108

Tab. 4-9 I_c, J_e values and retentions of STAR wires without indium filling at 77 K, self-field 109

Tab. 4-10 Specifications of STAR wires with indium filling 115

Tab. 4-11 I_c, J_e values and retentions of STAR wires with indium filling at 77 K, self-field 116

Tab. 4-12 Results of interlayer resistance measurements 128

List of Abbreviations

1G	First Generation
2G	Second Generation
BSCCO	Bismuth strontium calcium copper oxide
CC	Coated Conductor
DC	Direct Current
DI	Deionized
DOF	Depth of Field
EDX	Energy Dispersive X-ray
H_c	Critical Magnetic Field
H_{c1}	Lower Critical Magnetic Field
H_{c2}	Upper Critical Magnetic Field
HTS	High Temperature Superconductors
I_c	Critical Current
J_e	Engineering Critical Current Density
LTS	Low Temperature Superconductors
MOCVD	Metal Organic Chemical Vapor Deposition

MOD	Metal Organic Deposition
MTISL	Multiple Tape in Single Layer
NHMFL	National High Magnetic Field Lab
O.D.	Outer Diameter
OP	Overpressure
PIT	Powder in Tube
PLD	Pulsed Laser Deposition
REBCO	$REBa_2Cu_3O_{7-\delta}$ (RE=Gd, Y)
RPM	Round Per Minute
SEM	Scanning Electron Microscope
STAR	Symmetric Tape Round (wire)
T_c	Critical Temperature

Chapter 1. Introduction

This chapter introduces basic knowledge regarding superconductivity, describes several commonly used high temperature superconductors (HTSs), and compares the characteristics of different HTS cables. At the end of this chapter, the research objectives and dissertation outline are described.

1.1 Overview of superconductivity

In 1911, H. K. Onnes discovered that the resistivity of mercury vanished at 4.2 K [1], and he called this effect superconductivity. In the superconducting state, a material has no electrical resistivity when carrying direct currents. In addition, magnetic fields are expelled from the interior of the material, making it exhibit a perfect diamagnetism except for a very thin layer near the surface; this phenomenon is called the Meissner effect [2]. Unlike a "perfect conductor", whose state of magnetization would depend on the thermodynamic path, a superconductor always expels magnetic flux lines out when entering the superconducting state.

1.1.1 Critical values

To retain the superconducting state of a superconductor, three critical values must be met. These critical values are the critical temperature T_c, critical current density J_c, and critical magnetic field B_c. The critical values are inter-related, and thus the change of one critical value affects the other two critical values.

The T_c is the temperature at which the transition between the superconducting state ($T< T_c$) and the normal state ($T> T_c$) occurs. The transition does not happen at a single temperature but within a range of temperatures, which is called the transition width (ΔT_c). Therefore, several methods can be used to define T_c as a single value [3]. One common definition is that at the critical temperature, the resistivity of a material is half of the resistivity extrapolated from the temperature-resistivity curve of that material in the normal state. In this definition, the critical temperature is also called $T_{c,50}$, as shown in Fig. 1-1 [3].

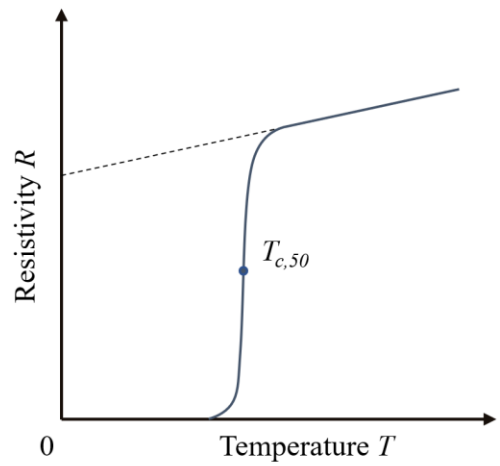

Fig. 1-1 Definition of critical temperature $T_{c,50}$

The critical current density J_c is the maximum current density that a superconductor can carry. Since there is no electrical resistivity in the superconducting state, the electric field E must equal zero. Near the transition to the normal state, the electric field starts to appear and can be described by a power law function [4]:

$$E = E_c \cdot \left(\frac{J}{J_c}\right)^n, \tag{1-1}$$

where E_c is the critical electric field, J is the current density, and n is the power factor or the "*n*-value" [5]. Therefore, at the critical current density J_c, a critical electric field E_c is generated in the superconductor. For low temperature superconductors (LTSs), such as Nb_3Sn and NbTi, a E_c of 0.1 μV/cm is used [6, 7], whereas for HTSs, such as REBCO or Bi-2212, although not standardized, a E_c of 1 μV/cm is commonly used [8, 9]. In technical applications, superconductors are usually used in combination with other materials for support or for electrical and thermal stabilization purposes. Therefore, the critical engineering current density J_e is commonly used instead of J_c. J_e

is defined as the critical current per unit area of the total cross-section that includes all the constituents.

If the magnetic field exceeds the critical magnetic field B_c, the material transfers from the superconducting state to the normal state. The temperature dependence of B_c is expressed as [3]:

$$B_c(T) = B_c(0) \cdot \left(1 - \left(\frac{T}{T_c}\right)^2\right), \tag{1-2}$$

where $B_c(0)$ and $B_c(T)$ are the critical fields at absolute zero and temperature T, respectively. It is worth noting that the magnetic field includes the external field and the field generated by the superconductor itself, i.e., the self-field. Therefore, the J_c and the external field are dependent on each other.

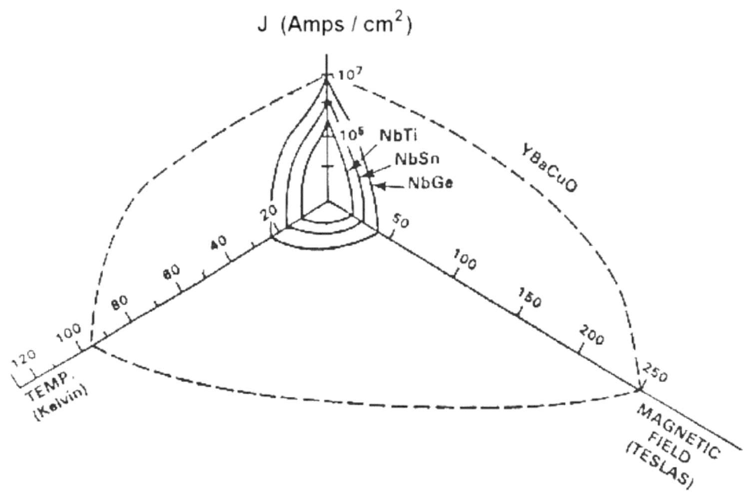

Fig. 1-2 Critical surfaces of several superconductors

By plotting the T_c, J_c, and B_c in the same coordinate system, a critical surface is obtained. Fig. 1-2 shows the critical surfaces of several superconductors, including YBCO, NbTi, Nb_3Ge, and Nb_3Sn [10]. Every point at or below the critical surface means that the material is in a superconducting state, whereas every point outside the critical surface means that the material is in the normal state. In order to stably operate a superconductor, the operation point in applications is usually chosen to be lower than the critical surface so that certain fluctuations in critical values do not force the superconductor to leave the superconducting state.

1.1.2 Type I and type II superconductors

Superconductors are divided into type I and type II superconductors based on their transition from the superconducting state to the normal state. Type I superconductors have only one critical field (H_c), whereas type II superconductors have two critical fields: the lower critical field (H_{c1}) and the upper critical field (H_{c2}).

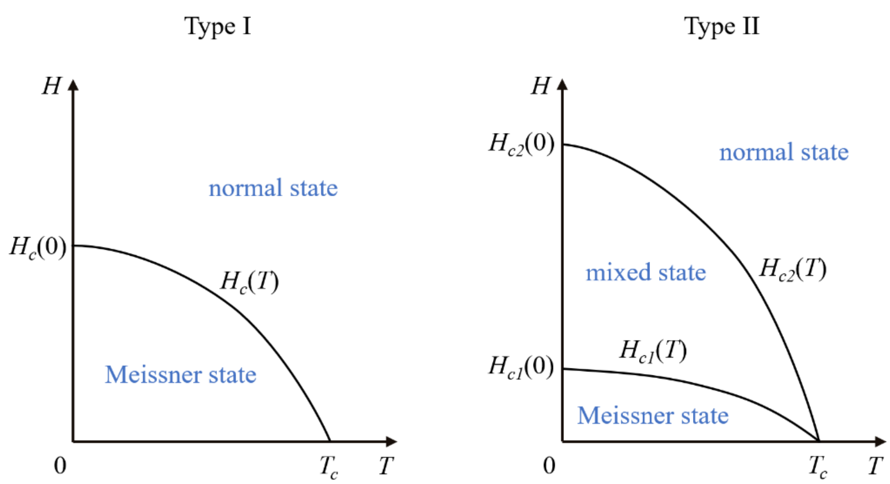

Fig. 1-3 Schematic diagram of temperature and magnetic field dependence of type I and type II superconductors

Type I superconductors are usually pure metals, such as lead (7.20 K), aluminum (1.18 K), titanium (0.4 K), and tin (3.72 K) [11]. When the temperature is below the T_c and the magnetic field is below the H_c, a type I superconductor exhibits zero electrical resistivity and the Meissner effect. Since the H_c of a type I superconductor is in the range of a few mT, flowing a very small current in the superconductor makes it lose its superconductivity. For this reason, type I superconductors are not suitable for practical applications.

Type II superconductors are in the Meissner state when the magnetic field is smaller than H_{c1} and in the normal state when the magnetic field is larger than H_{c2}. In a magnetic field between H_{c1} and H_{c2}, type II superconductors enter a state called the "mixed state" [12], as shown in Fig. 1-3, where magnetic flux lines penetrate the sample. The mixed state is still a superconducting state and there is no electrical resistance. Since H_{c2} can be as high as several hundred Tesla, type II superconductors have much larger potential for use in various applications than type I superconductors.

In the mixed state, the magnetic flux lines enter a superconductor in quantized flux tubes, i.e., fluxons. Each fluxon has a normal conducting core that is surrounded by a superconducting circulating current. Therefore, it is favored energetically if a fluxon is located at a defect in the superconductor as defects are also in the normal conducting state. To maximize the negative surface free energy between the fluxons and surrounding areas, the number of fluxons is maximized. Each fluxon has a constant flux value: $\Phi_0 = 2.068 \times 10^{-15}$ Wb [13]. The fluxons arrange themselves in a two-dimensional triangular pattern with a flux lattice spacing [14]:

$$a_0 = 1.075\sqrt{\frac{\Phi_0}{B}}. \tag{1-3}$$

As magnetic field B increases, the spacing between fluxons decreases and the number of fluxons increases.

In a magnetic field, if a superconductor in the mixed state carries a current with a current density of J, there is a Lorentz force F_L acting on the fluxons in the superconductor. The mean Lorentz force per unit length f_L is expressed as

$$f_L = \Phi_0 J \sin\theta, \tag{1-4}$$

where θ is the angle between the field and current. Since fluxons are energetically favored if they are located at defects, the force that holds fluxons at defects or pinning centers is called the "pinning force” F_P. If the Lorentz force is not very high, i.e., $F_L < F_P$, the fluxons are pinned in the material and do not move. As the current increases, the Lorentz force eventually exceeds the pinning force, i.e., $F_L > F_P$, and the fluxons start to move. During the movement of fluxons and the disappearance and regeneration of new fluxons, energy is dissipated. This phenomenon is called “flux creep” [15], where the corresponding resistance is much smaller than the normal state resistance. The pinning force is increased by inducing more defects in superconductors through a complicated vortex-defect behavior [16]; therefore, the performance of type II superconductors can be increased substantially by doping them with other materials [17-21].

1.1.3 Superconductors used in applications

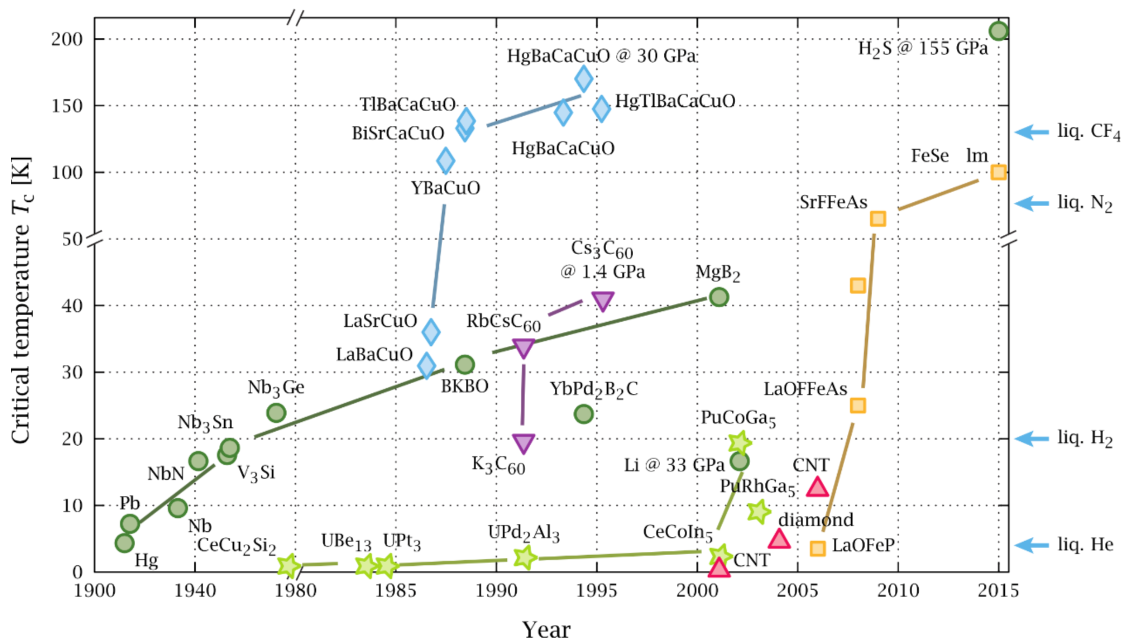

Fig. 1-4 Timeline of discovery of superconductors

Over a century, many superconducting materials were discovered. Fig. 1-4 is a timeline of the discovery of superconductors in history [22]. The first widely used superconductors were the LTS Nb_3Sn [23] and NbTi [24, 25], whose superconducting mechanism can be explained by the Bardeen–Cooper–Schrieffer (BCS) theory [26]. Therefore, they are also called BCS superconductors, which are marked as green circles in Fig. 1-4. Cuprate superconductors, which are marked as blue diamonds in Fig. 1-4, were first discovered in 1986 [27]. Their critical temperatures are higher than 30 K and cannot be explained by BCS theory. This type of superconductor is called a "non-BCS superconductor" or HTS.

Tab. 1-1 Critical temperature, critical magnetic field, and target fields of commonly used superconductors

Superconductor	T_c (K)	B_{c2} (T)	Target fields
NbTi	9.6	12-15	Medium
Nb_3Sn	18	25-29	High
Bi-2212	95	175-225	Highest
Bi-2223	107	107	Medium (at medium-to-high temperature)
REBCO	92-95	120-250	Highest
MgB_2	35-39	14-40	Low to medium

As previously discussed, only type II superconductors are useful in practical applications. There are six type II superconductors that are commonly used: NbTi, Nb_3Sn, Bi-2212, Bi-2223, REBCO, and MgB_2. Their critical temperatures, critical magnetic fields, and target fields are listed in Tab. 1-1 [28]. Because of their significantly different critical magnetic fields, the target applications are also distinctive among these superconductors. MgB_2 is potentially suitable for use in low-to-medium magnetic field applications, such as in sensitive magnetic field detectors [29]. NbTi is widely used in magnets up to 9 T: most of the magnets in magnetic resonance imaging systems are made of NbTi wires [30]. For magnets that require a higher field, Nb_3Sn can be used, although the brittleness of this material makes the winding of Nb_3Sn wire difficult [31]. Bi-2223 can be used in power cables in the power industry [32]. When the magnetic field exceeds 20 T, the most viable superconductors are Bi-2212 and REBCO; they can be wound into inserts for hybrid magnets and generate very high magnetic fields [33, 34].

1.2 High temperature superconductors (HTSs)

1.2.1 BSCCO

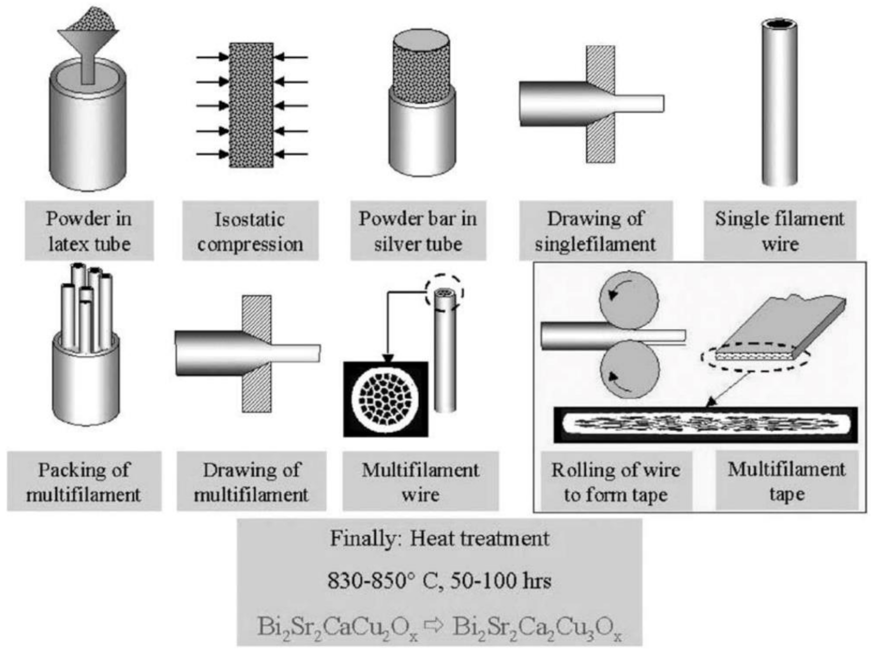

Fig. 1-5 Outline of PIT method in Bi-2223 fabrication

$Bi_2Sr_2Ca_2Cu_3O_x$ (Bi-2223) HTS tapes are mainly fabricated by the powder-in-tube (PIT) method and are also known as first-generation (1G) HTSs. The outline of the PIT process is illustrated in Fig. 1-5 [35]. Raw materials are milled and filled into small silver tubes; these small tubes are drawn into single filaments, packed in another silver tube, and drawn again. After several rounds of packing and drawing, the wire is rolled into a tape form; through heat treatments in a high-oxygen atmosphere, superconductivity in Bi-2223 is established. A cross-section of multiple filaments in a silver matrix can be seen at the bottom right corner of Fig. 1-5. In the final heat treatment process, oxygen needs to penetrate the tubes and react with the materials; therefore, silver is the most feasible choice for the tube material due to its high oxygen permeability [36]. This heavy dependence on silver makes BSCCO tapes expensive for industrial applications. Because of the low irreversible field of Bi-2223 [37], at which the critical current density drops to zero, Bi-2223 is mainly suitable for low-to-medium magnetic field applications.

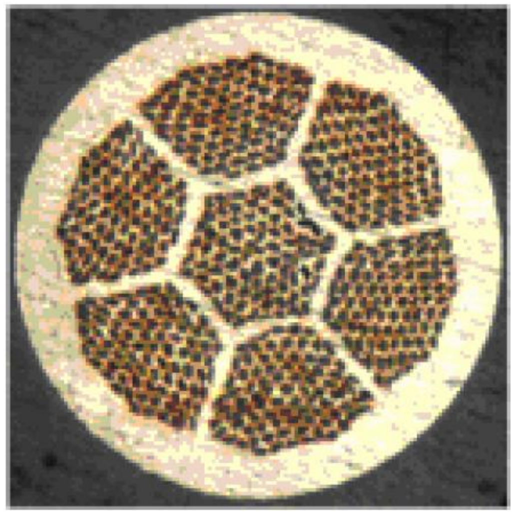

Fig. 1-6 Cross-section photograph of a Bi-2212 wire

The Bi-2212 is the only round HTS wire available, the conductor geometry which is preferred by magnet designers. Fig. 1-6 shows a cross-section photograph of a Bi-2212 wire [37] where the multi-filamentary structure can be clearly viewed. To obtain a good superconducting property, the materials must be partially melted and therefore a complicated heat treatment is necessary for Bi-2212 wire; however, due to a 60-70% density of powder in the wire [38], air bubbles form during the melting process and occupy 30-40% of the space in the wire. This issue makes the J_e of Bi-2212 too low to be used in practical applications. For this reason, the overpressure (OP) process, which was initially developed for Bi-2223 tapes, was applied to Bi-2212 wires [39] and increased the J_e value significantly. Moderate pressure is applied on the wire during the heat treatment and compresses the diameter of the silver tube to squeeze out the bubbles. By using the OP process, the J_e of Bi-2212 wires increases by six- to seven-fold [38]. Similar to Bi-2223 tapes, the raw material cost (silver) and relatively low mechanical properties of Bi-2212 wire hinder its use in large-scale applications.

1.2.2 REBCO

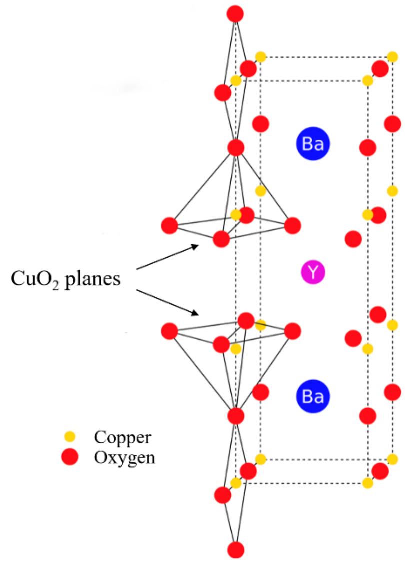

Fig. 1-7 Lattice structure of yttrium barium copper oxide

The REBCO HTS was first discovered in 1986. It is a family of crystalline chemical compounds, which are famous for displaying superconductivity above the boiling temperature of liquid nitrogen (77 K) [40]. REBCO belongs to the category of materials with the perovskite structure of ABO_3, where "A" atoms occupy the corner, "B" atoms occupy the body center, and oxygen atoms occupy the face centers. REBCO crystallizes in a layer structure where the CuO_2 planes are the main reason for superconductivity and the layers between them act as Josephson barriers [41]. Fig. 1-7 shows the lattice structure of yttrium barium copper oxide [42].

REBCO material is usually deposited physically or chemically on substrate tapes as a thin film, which is why it is called a coated conductor (CC). This type of superconductor is also known as a second-generation (2G) superconductor. Because the current carrying capability of REBCO is highly dependent on the alignment between the grains [43], bulk REBCO, which has grains oriented in random directions, has low critical current density. When deposited as a thin film on substrates, the grain alignment in the REBCO layer is critical. Since it is not realistic to produce long single-crystalline substrates, an epitaxial growth method to deposit REBCO onto polycrystalline substrates was developed [44].

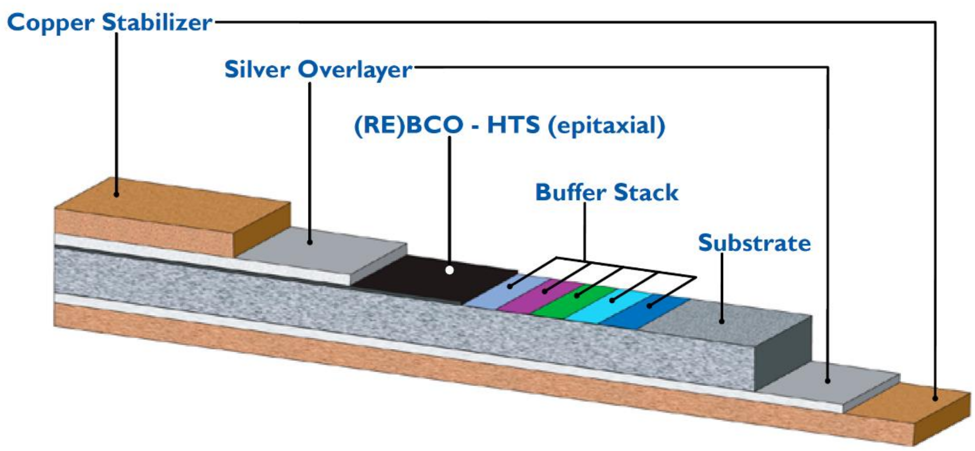

Fig. 1-8 Schematic layout of a REBCO tape from Superpower

Fig. 1-8 is a schematic layer-by-layer layout of a REBCO tape from Superpower [45]. The REBCO coated conductors have a substrate as the main body. The substrate material must have a good lattice that matches the REBCO matrix for epitaxial growth; other important factors include a similar thermal expansion coefficient as REBCO, good mechanical properties, and chemical stability [46, 47]. Therefore, the common choice of substrate material is nickel-based alloy, such as Hastelloy. The usual thickness of the substrate is between 50 and 120 μm [48]. REBCO tapes with a thinner substrate (30 μm) are reported to have similar performance as the tapes with substrates of normal thickness [49], but are yet to be produced at a large scale.

Several layers of buffer material, including Al_2O_3, Y_2O_3, MgO, $LaMnO_3$, are deposited onto the top of the substrate [50-52]. These buffer layers block diffusion from the substrate to REBCO, improve the texture quality, and match the lattice parameter. Using the methods of Rolling Assisted Biaxially Textured Substrates (RABiTS) or Ion-Beam Assisted Deposition (IBAD) methods, a bi-axial texture is achieved in the buffer stacks [53, 54]. The near-single crystalline structure determines the grain orientation of the REBCO layer grown epitaxially on it. The REBCO layer usually has a thickness between 0.85 and 3 μm [48] and is grown by either a physical method, such as pulsed laser deposition (PLD), or a chemical method, such as Metal Organic Chemical Vapor Deposition (MOCVD) or Metal Organic Deposition (MOD) [55-57]. A thin layer of silver is deposited around the tape for electrical contact and protection. In addition, a copper layer is usually laminated or electroplated onto the tape for electrical stabilization.

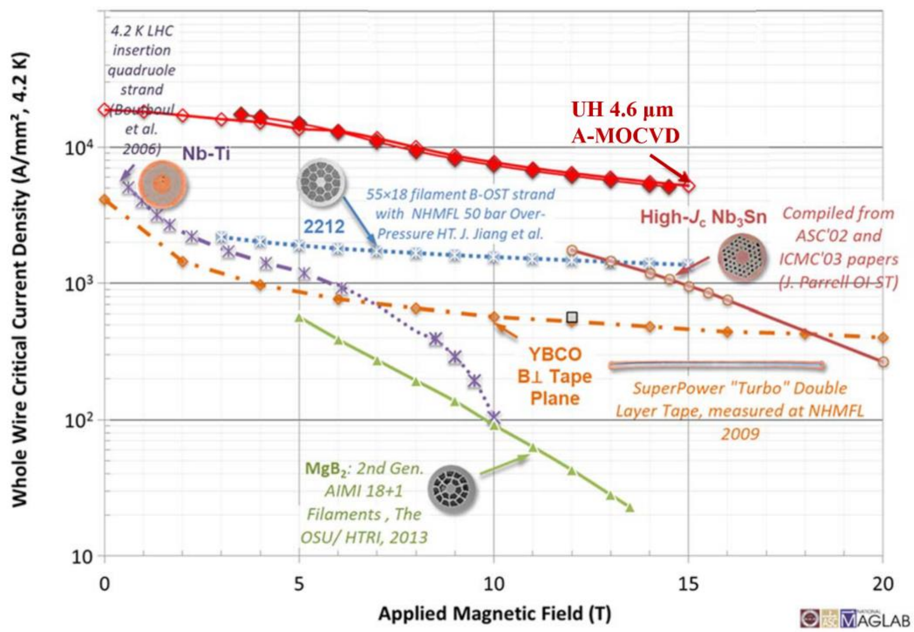

Fig. 1-9 Comparison of field dependence of J_e; several superconductors are included

In terms of current capacity, at 77 K self-field, the J_c of the epitaxially-grown REBCO layer is usually in the magnitude of 10 kA/mm^2. REBCO tapes with a current per unit width higher than 400 A/cm are produced at long lengths [58]; at a length of several meters, tapes with 1000 A/cm are also available [59]. Because of its highly anisotropic structure, the J_c of the REBCO tape is dependent on the angle between the magnetic field and the tape surface. For normal REBCO tapes, when the magnetic field is perpendicular to the tape surface (B ∥ c), the performance is lower than that of the tape in a magnetic field parallel to the tape surface (B ∥ a-b). With a zirconium doping technique [60], which is also called advanced pinning, the performance of REBCO tape at B ∥ c is substantially improved. A J_c of 12.32 MA/cm^2 at 4.2 K, 14 T (B ∥ c) was achieved in an advanced-MOCVD deposited tape with a >4 μm thick REBCO layer [61]. The in-field performance comparison between this sample and several other superconductors is shown in Fig. 1-9 [61].

The strong mechanical strength of the substrate allows the REBCO tapes to sustain 0.5% longitudinal strain with less than 5% I_c degradation [62]. Because of the ceramic nature of the REBCO material, the performance of REBCO tapes is much less influenced by compressive strain than tensile strain [63]. The bending properties of REBCO tapes are strongly related to the tape structure, such as the thickness of the substrate and copper stabilizer. With 100 μm of copper stabilizer on a REBCO tape with 100 μm of Hastelloy, the tape can be bent to a radius of 6 mm with a fully reversible I_c [64].

Compared to BSCCO, the fabrication of REBCO tape is relatively complicated, but its outstanding mechanical properties, current carrying capability, and high in-field performance, as well as the low raw material costs, make it a very attractive HTS material for high magnetic field applications.

1.3 REBCO cables

RECBO-coated conductors are flat and have large aspect ratios. The typical conductor dimensions are 4 to 12 mm wide and 50 to 120 μm thick. To fully utilize the advantages of REBCO tape, multiple cabling concepts were proposed, such as Roebel Assembled Coated Conductor (RACC) cables, Twisted Stacked-Tape Cables (TSTC), and Conductor on Round Core (CORC) cables. These cable structures are described and compared in this section.

1.3.1 RACC cables

Roebel cable was first proposed in 1912 by Ludwig Roebel [65]. In this structure, several copper wires are interweaved in a short transposition distance to reduce the eddy current and heat generated in the copper conductors of power generators. In 2006, at the Karlsruhe Institute of

Technology (KIT), this structure was applied to HTS cable [66]. Fig. 1-10 shows a dummy RACC cable made with copper and stainless tapes [67].

Fig. 1-10 A dummy RACC made with copper and stainless tapes

As can be seen, the RACC cable is assembled with multiple REBCO tapes with a zigzag pattern. To increase the material utilization rate, multiple zigzagged tapes are punched out or laser-slit from a single piece of REBCO tape. With an automatic punching machine, the width of tape can be precisely controlled to less than 1% variation [8]. For short RACC cables, hand assembly is used, whereas long cables are usually assembled by machines [68]. The weave pattern ensures that all the tapes change their position entirely so that the RACC cable is fully transposed; however, because of this weave pattern and the suddenly-changed geometry at the inner corners of each strand, the so-called von Mises stress is concentrated at corners [69]. In addition, the transposition distance of RACC cable and the width of each strand determine the maximum number of strands in a single cable.

The anisotropic geometry of RACC cable results in anisotropic mechanical properties. If the mechanical force is parallel to the cable length, which is also the direction of hoop stress, or perpendicular to the tape surface, the cable is not sensitive to the load. In these two directions, the critical tensile stresses of a 5 mm wide 15-strand RACC cable were measured to be 260 MPa and 240 MPa, respectively [69]. If the mechanical force is perpendicular to the cable but parallel to the tape surface, the cable is much more sensitive to the load since the strand edges are easily damaged. Fig. 1-11 shows the damaged edge of a RACC cable that was tested in a 6 T background field with the Lorentz force perpendicular to the cable but parallel to the tape surface [69].

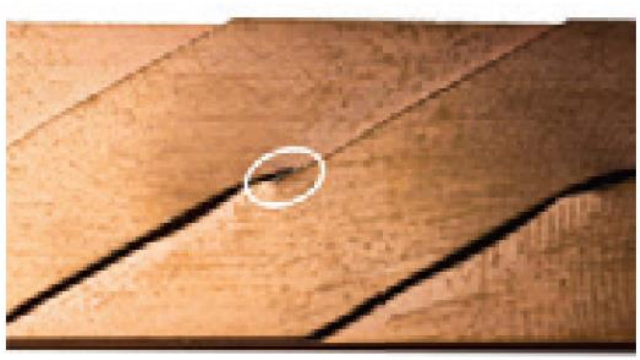

Fig. 1-11 Damaged edge of a RACC cable after in-field measurement

With different widths and numbers of strands, the RACC cable is able to carry 500 A (16 strands) to 2.6 kA (45 strands), with a corresponding J_e of up to 125 A/mm^2 at 77 K in self-field [8]. In a 9.6 T background field that was perpendicular to the cable surface, a J_e of 364 A/mm^2 was measured; because of the self-field effect of RACC cable, the expected J_e was around 500 A/mm^2 [70]. Due to its tape-like geometry, the bending properties of RACC cable are also similar to those of REBCO tape. In the easy-bending direction, where the bending radial direction is perpendicular to the cable surface, the RACC cable can be bent to 3 cm diameter without degradation [71]. In the hard-bending direction, where the bending radial direction is in the same plane as the cable, it is very difficult to bend the RACC cable without damage. In addition, if the transposition length of the cable is larger than the bending circumference, the stress in the RACC cable is not even on each strand.

1.3.2 TSTC cables

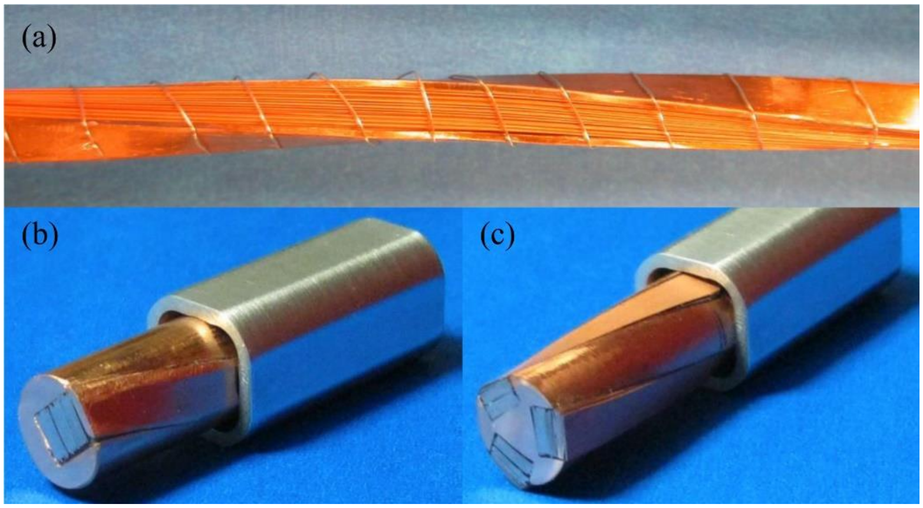

(a) Single TSTC with 32 tapes; (b) Single-tape-stack TSTC; (c) Triple-tape-stack TSTC

Fig. 1-12 Twisted Stacked Tape Cables (TSTC)

The structure of TSTC was first proposed in 2011 [72]. It is a simple cabling method with a high tape usage. Fig. 1-12 shows photographs of several TSTCs [73]. Narrow REBCO tapes (usually 4-5 mm) are stacked together and bundled with copper bars on each side. Structurally speaking, it is preferable to have the same width and thickness in the tape stack, which limits the number of tapes in each cable. A 4.8×4.8 mm^2 TSTC, as shown in Fig. 1-12 (a), can hold 32 tapes with a twist pitch of 200 mm [73]. The minimum twist pitch without I_c degradation is 150 mm, and 100 mm if a 2% I_c degradation is allowed [73]. To increase the mechanical strength, the tape stack is usually inserted into a twisted groove of a round copper former and then protected by a jacket, as shown in Fig. 1-12 (b). Gaps between the former and tape stack are filled with solder material. Multiple tape stacks can be bundled together to improve the current carrying capacity, as displayed in Fig. 1-12 (c). Since the position of each tape in the tape stack does not change, TSTC is considered partially transposed.

For a TSTC inserted into a copper former, the round geometry makes the cable isotropic in the radial direction. When the load is applied in the cable's longitudinal direction, due to the tape alignment, it is expected that the TSTC has a similar mechanical strength as REBCO tapes, which is between 500 MPa and 700 MPa [28]. When the force is loaded in the radial direction, the tape stack inside the TSTC is pushed against the copper former and jacket. In each twist pitch, the force applied on the tape stack changes from the tape edge to the tape surface, whereas the former situation is more critical for TSTC. A single-tape-stack TSTC, which consists of 40 pieces of 4 mm wide tape, was tested in background fields with the Lorentz force in the radial direction. At 4.2 K, in a 6 T field, the TSTC showed 12% I_c degradation with a critical current of 7.7 kA; in a 12 T field, it showed 4% I_c degradation with a critical current of 5.1 kA [28].

The current carrying capability and J_e value of a TSTC vary based on the number of tape stacks in it. At 4.2 K in a 16 T field, for a single-tape-stack TSTC consisting of 40 tapes, the outer diameter was 6 mm and the J_e was 273 A/mm^2; for a triple-tape-stack TSTC consisting of 40×3 tapes, the outer diameter was 13 mm and the J_e was 175 A/mm^2 . The bending properties of TSTC also depend on its structure: if the multiple-tape-stack structure is used, the whole TSTC is hard to bend into a small diameter in any direction due to the different easy-bending directions of each tape stack; if there is only one tape stack, the I_c degradation was 1.9% at a bending diameter of 250 mm and 5.4% at a bending diameter of 140 mm [72].

1.3.3 CORC cables

Spiral winding of REBCO tapes with a small twist pitch was first demonstrated in 2005. As shown in Fig. 1-13, a 2 mm wide, copper-surrounded REBCO conductor with a 100 μm substrate was twisted 10 full turns while maintaining good current-carrying ability, where 95% of the I_c was retained at a twist pitch of 4.6 cm [74]. In the same year, the idea of wrapping a REBCO tape on a round core was demonstrated [75], which proved the possibility of developing REBCO cables with a round former. CORC cables were first presented in 2009 [76]. As shown in Fig. 1-14, multiple layers of normal REBCO tapes are wound on a round former and each layer of tape is wound in alternating directions. The diameter of the former ranges from 2.5 mm to 5.5 mm and the number of layers from 6 to 17 [77, 78]. Since the position of each tape in a CORC cable remains the same, the cable is considered partially transposed.

Fig. 1-13 Photograph of a 2 mm wide REBCO conductor with 10 full twists

Fig. 1-14 Conductor on Round Core (CORC) cable

The round geometry makes CORC cables isotropic in the radial direction, and there are only two different directions for the loading force. If the force is applied in the cable's longitudinal direction, due to the nearly 45-degree angle between the force and the tapes' length direction, the cable is insensitive to the force [79]. Therefore, the performance of CORC cables under a longitudinal load is comparable or even better than that of REBCO tapes. At the critical stress limit of REBCO tape, the tape exhibited a 10% I_c reduction, whereas the CORC cable exhibited only a 3% I_c reduction [28]. If the force is applied in the radial direction, the tapes in a CORC cable are under compressive stresses. In a relatively low magnetic field, the small gaps between the tapes do not affect the overall strength of the cable and therefore the CORC cable is expected to withstand radial loads without I_c degradation. In a 12 T magnetic field, a five-layer, 15-tape CORC cable carried a 2.5 kA current and did not show any degradation [28].

The current capacity and bending properties of CORC cables are largely affected by the number of tapes in the cable. For a six-layer, 12-tape CORC cable, at 77 K in self-field, the I_c was 612 A in a straight form and retained around 90% of the I_c when bent to a 3.5 cm diameter; for a 10-layer, 20-tape CORC cable, at 77 K in self-field, the I_c was 1680 A in the straight form, but only retained less than 70% of the I_c at a 3.5 cm bending diameter. At 4.2 K in a 10 T magnetic field, the highest reported J_e of CORC cables was 412 A/mm^2. To obtain such a J_e value, the CORC cable had 11 layers and the bending diameter was 6 cm [80].

1.3.4 REBCO cable comparison

Tab. 1-2 Properties comparison of REBCO cables

	RACC	TSTC	CORC
Tape consumption	209%	103%	141%
Transposition	Full	Partial	Partial
In-field J_e (A/mm^2) at 4.2 K	364, 9.6 T	274, 16 T	412, 10 T
Minimal bending diameter (mm)	30	140	60
Comment on minimal bending diameter	In certain bending directions	Single-tape-stack structure	29 tapes in 11 layers

The previously discussed tape consumption, transposition, engineering current density, and bending properties of REBCO cables are summarized in Tab. 1-2. It should be mentioned that the tape consumption of different cables is calculated from cabling degradation and the material wasting rate during cabling [28]. The RACC cable consumes the most tape since the zigzagged strand punching wastes a certain amount of material. CORC has a 141% tape consumption rate due to the 45-degree winding angle, whereas TSTC needs the least tape because of the twist tape structure.

1.4 Dissertation objectives and outline

The main objective of this dissertation is to develop a new REBCO wire that can be potentially used in compact accelerator applications, such as CCT coils. CCT coil design was first proposed by Meyer and Flasck in 1969 [81] and has re-gained attention recently in various accelerator magnet applications [82] and accelerator-based ion-beam particle therapy (IBT) in the medical industry [83]. CCT coils generate multipole magnetic fields at a smaller winding radius while preventing the stress accumulation that results from Lorentz forces. The CCT coil is usually used as a magnet insert, which requires a compact design to fit into the bore of outsert magnets. This requires a high J_e at a small bending radius. It was pointed out that the minimum required J_e was 540 A/mm^2 at 21 T, 4.2 K, at a bending diameter of 30 mm [84].

From the previous discussion, it can be concluded that the existing REBCO cables cannot provide the performance required by CCT coils, either because of their relatively low J_e values or the large bending diameters. Therefore, flexible REBCO wires that can be bent into a small diameter while maintaining a high J_e value are needed, but this need cannot be met by currently commercially available REBCO tapes. Therefore, special REBCO tapes with remarkable bending performance must be developed.

The outline of this dissertation is as follows:

- Chapter 1 provides the background knowledge of superconductivity, HTS cables, and the objective of this work.
- Chapter 2 presents a detailed description of the symmetric tape and STAR wire fabrication processes.

- Chapter 3 discusses the electromechanical properties of the symmetric tape and optimization of the tape structure.
- Chapter 4 analyzes the 77 K and 4.2 K electrical performance of STAR wires with different structures.
- Chapter 5 summarizes the results and provides possible future works.

Chapter 2. STAR wire fabrication

This chapter presents a detailed description of the STAR wire fabrication process. Commercial REBCO tapes are selected to produce symmetric tapes, which are used for STAR wire winding. The preparation procedures of symmetric tapes, including grinding, laser slitting, and copper electroplating, are described in the sequence of production; STAR wire fabrication techniques, such as the winding process and cable terminal soldering, are introduced afterwards. Fig. 2-1 shows the general STAR wire fabrication process.

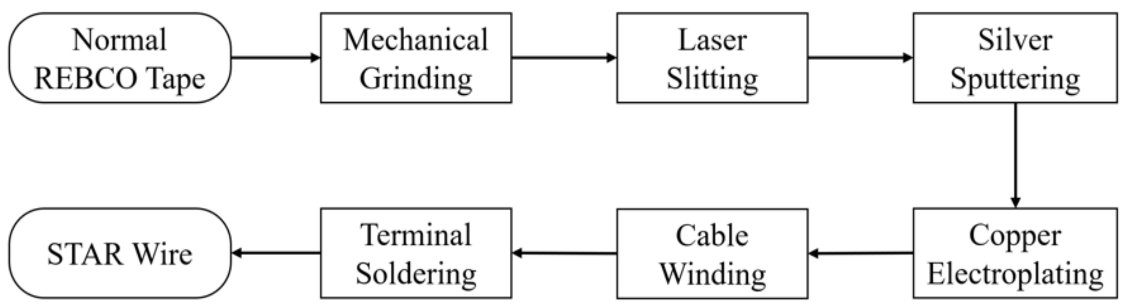

Fig. 2-1 A flowchart of the STAR wire fabrication process

2.1 REBCO tape grinding

Symmetric REBCO tapes are used to fabricate STAR wires. Compared to normal REBCO tape, the REBCO layer of symmetric tape is much closer to its neutral axis, making the I_c retention much higher at a small bending radius. This allows STAR wire to be wound on a small round former and exhibit high J_e. To produce symmetric tapes, the first step is to reduce the thickness of the Hastelloy C-276 substrate, which is a nickel-molybdenum-chromium alloy with stable chemical properties and high mechanical strength [85]. Mechanical dry grinding is used to reduce the substrate's thickness.

2.1.1 Reel-to-reel tape grinding system

2.1.1.1 Grinding machine prototype

A prototype of the reel-to-reel tape grinding machine was first built to verify the efficacy of the dry grinding method, as shown in Fig. 2-2. The machine frame was built with aluminum extrusions. A stepper motor was attached to the left spool to control the movement of the tape. The tension applied on the tape was controlled by a torque motor, which was connected to the right spool. One grinding wheel, with adjustable speed, was used to grind the back side of the tape.

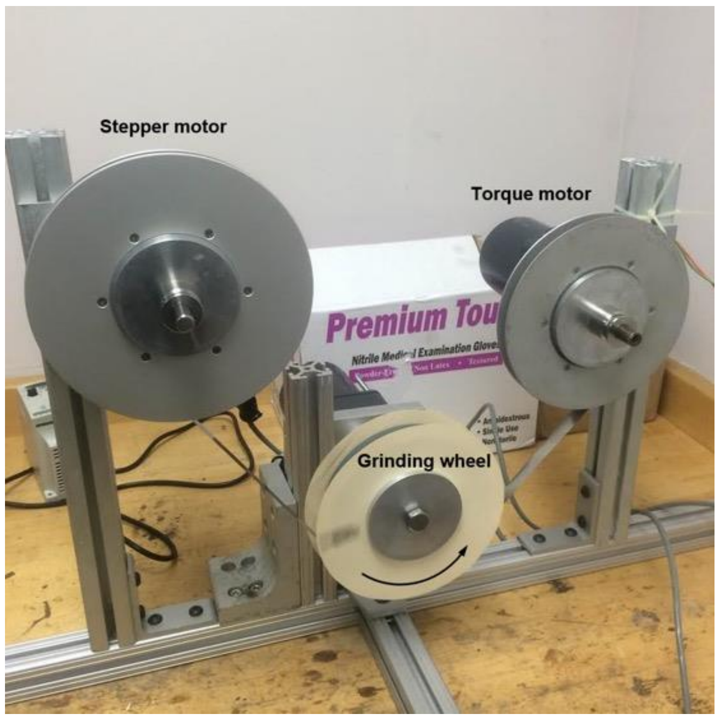

Fig. 2-2 Reel-to-reel grinding machine prototype

The initial grinding test was performed on a 25 cm long commercial REBCO tape with a 1.8 μm thick silver layer on the back side of the substrate using 80 grit aluminum oxide grinding wheels. After 24 turns of grinding, the thickness of tape in the middle was reduced from 54 μm to 40 μm. The I_c of the tape dropped from 300 A to 180 A. Fig. 2-3 shows the surface changes after the first six turns of grinding, where the dark-colored region is the remaining silver. The pattern indicated that material was removed from the tape in a relatively uniform manner.

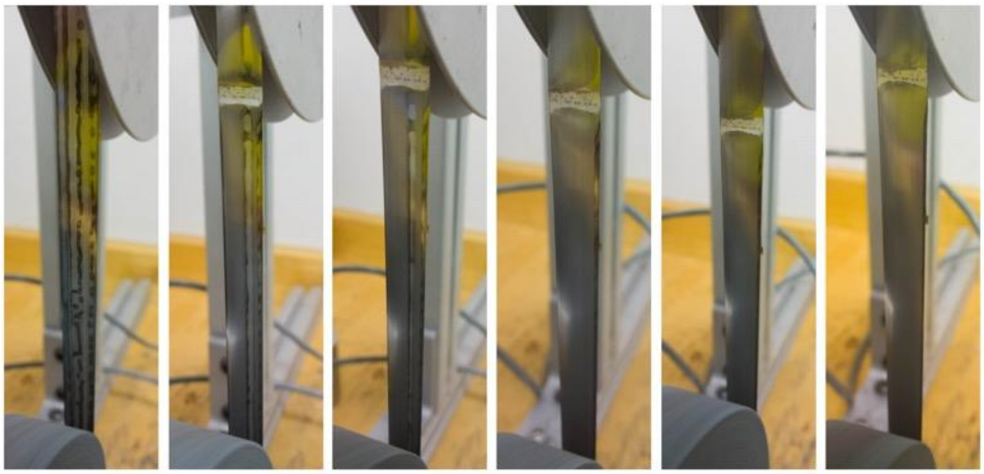

Fig. 2-3 Surface change of the back side of REBCO tape

The initial grinding test verified the feasibility of using the dry grinding method to reduce the thickness of REBCO tape. The thickness of the substrate in the middle was reduced by 14 μm in less than 30 turns of grinding; however, several issues were revealed in the prototype grinding test. The hardness of the aluminum oxide wheel was not enough to effectively abrade the Hastelloy. In addition, the vibration and misalignment of the grinding wheel caused the tape I_c to drop and resulted in non-uniform thickness after grinding.

2.1.1.2 Four-wheel grinding system

A custom four-wheel grinding system, which is shown in Fig. 2-4, was built to improve the quality and efficiency of grinding of long tapes. The whole chamber was assembled with aluminum extrusions and plates. Transparent acrylic plates were installed at the front and top sides to check the grinding operation. The number of grinding wheels was expanded to four to expedite the grinding speed; the even number of wheels also balanced the grinding force applied to the tape.

Silicon carbide grinding wheels, with grits ranging from 60 to 120, were selected. The 60 and 80 grit wheels were used for the initial coarse grinding and 120 grit wheels for fine grinding.

Fig. 2-4 Four-wheel reel-to-reel grinding system

2.1.2 Ground tape uniformity analysis

2.1.2.1 Ground tape thickness

Tab. 2-1 25 m tape grinding parameters

Grinding turns	Grinding wheel grit	Tape middle thickness (μm)
1-2	60	54-53
3-6	80	50-37
7-10	120	34-25

A piece of 25 m long, 12 mm wide stabilizer-free commercial REBCO tape SF12050 from SuperPower Inc. was ground by the four-wheel grinding system. The initial tape thickness was 54 μm and the target thickness in the middle was 25 μm. The tape movement speed was set at 9.2 cm/min. Tab. 2-1 summarizes the grinding parameters, including wheel grit and number of turns used. Ten turns of grinding were applied to reach a thickness of 25 μm. As the number of grinding turns increased, less aggressive grinding parameters were used to avoid tape damage.

After each turn of grinding, the tape thickness was read by micrometer and averaged across three readings. At 12.5 m in length, three points with distances of 1 mm, 6 mm, and 11 mm from one edge were selected for the thickness check. The results are plotted in Fig. 2-5. The first three turns initialized the grinding and removed the silver layer. In the middle part of the tape, 4 μm of material was ground off. At the edge of the tape, the thickness decreased by approximately 13 μm in three turns. After initialization, the grinding efficiency was between 2.7 to 3.6 μm per turn. The final thickness difference between the middle and edge points was 5 μm.

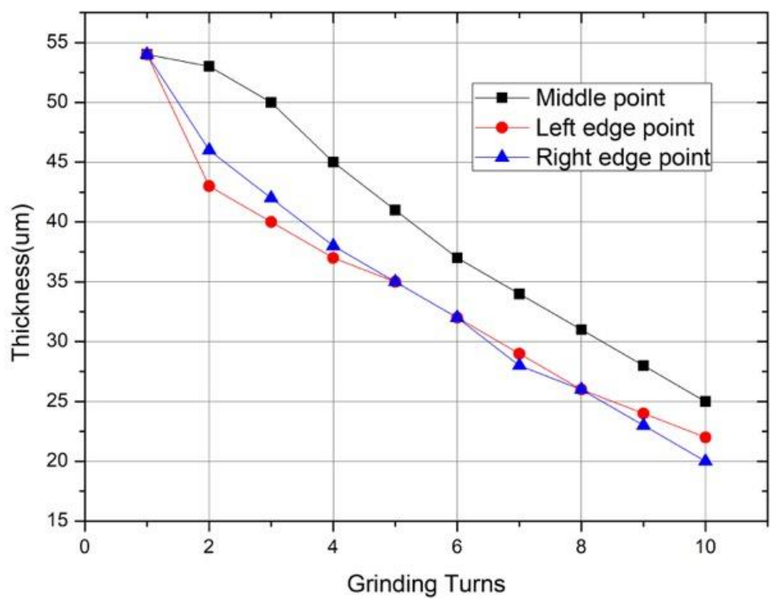

Fig. 2-5 Plot of tape thickness versus grinding turns

The initial grinding efficiency discrepancy between the middle and edge locations was caused by different grinding pressures. Even after carefully balancing the wheels, small vibrations still existed in the grinding wheels and caused the tape to sway slightly in the transversal direction. The transversal sway increased the grinding pressure at the tape edges and caused the thickness to decrease at a higher rate. After the grinding initialization, the thickness difference between the middle and edge locations compensated for the sway movement and prevented further grinding efficiency discrepancies. Therefore, the thickness difference was kept the same to the end. Compared to the grinding machine prototype, the thickness difference was drastically reduced by the improved alignment and balance of the grinding wheels.

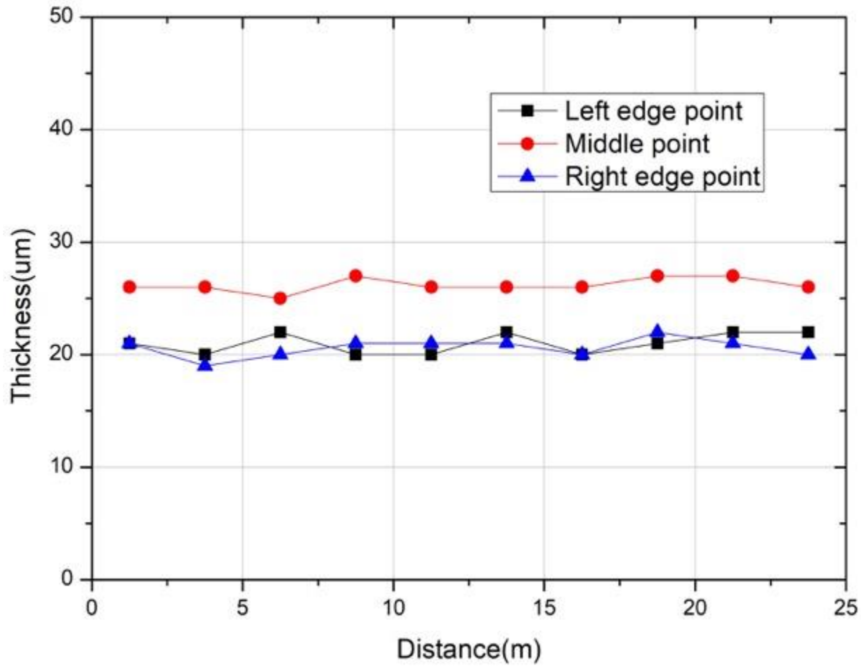

Fig. 2-6 Tape thickness at three different points along the length

After 10 turns of grinding, the lengthwise thickness uniformity was also studied. The thickness at three points at every 2.5 m along the length of the tape is shown in Fig. 2-6. As the plot shows, the thickness variation over 25 m was less than 2 μm. The left edge and right edge thicknesses were within 2 μm of each other and the middle point was 5-6 μm thicker than the edge. The highly uniform and symmetric tape thickness proved that the dry grinding method effectively reduced the thickness of the REBCO tape.

2.1.3 Ground tape weak point examination

The thinned tape was examined by TapeStar and SHPM to detect I_c drops after grinding. Both methods measure the trapped magnetic field distribution via a Hall probe sensor, where the normal region has a stronger field and the damaged region has a weaker field. With the fast Fourier transform algorithm, the magnetic field distribution along the tape's width is integrated to calculate the tape I_c. Fig. 2-7 shows the calculated I_c values of the 25 m tape before and after grinding by TapeStar. The initial I_c was 420 A and multiple I_c drops, down to 210 A, were observed after grinding.

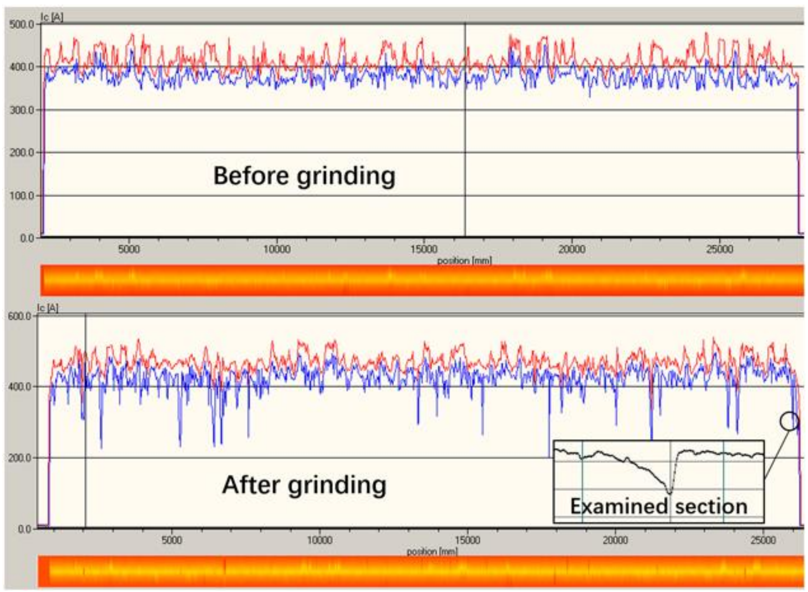

Fig. 2-7 25 m tape I_c comparison before and after grinding; the circled region was examined.

Since TapeStar lacked resolution along the width of the tape, SHPM was utilized to plot high-resolution local magnetic field distribution map, which can locate weak points precisely [86-88]. A 5 cm long sample that corresponded to the rightmost weak point in the 25 m tape was cut and scanned by SHPM. The 2D and 3D magnetic field plots are shown in Fig. 2-8, where the resolution in the X direction is 0.1 mm and in the Y direction is 1 mm. The top 23 mm region showed a strong and uniform magnetic field, indicating that there was no damage in the REBCO layer. However, the 5 mm wide region on the bottom left showed a very weak trapped field. The widest damaged region took up approximately 40% of the whole tape width, which was consistent with the Ic drop shown in Fig. 2-7.

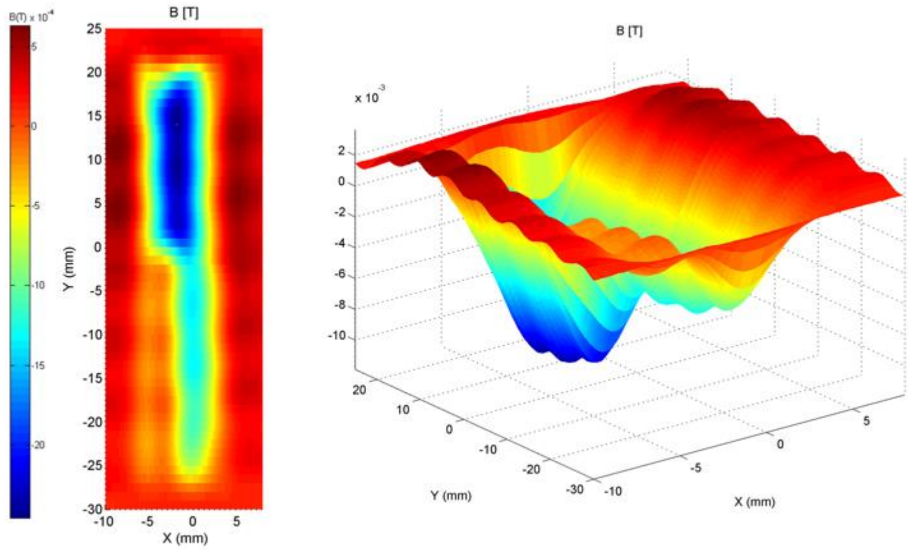

Fig. 2-8 Magnetic field plot of weak region by SHPM

The damaged region was further checked by SEM. The silver layer on the tape was chemically etched to expose the REBCO layer. Using SEM, two kinds of damage were found on the REBCO layer: chipping-off damage and in-layer damage. At the chipping-off damage sections, small pieces of REBCO in multiple locations chipped off, as depicted in Fig. 2-9 (a) (b). The diameters of the REBCO chips were between 10 μm and 60 μm. EDX analysis on two locations of the chips, as shown in Fig. 2-10, confirmed that the dark-colored area was the surface of the buffer layer and the light-colored area was inside the REBCO layer. One possible reason for the chipping-off damage is the excessive strain applied to the REBCO layer during coarse grinding. Low-grit grinding wheels, such as 60-grit wheels, have grainy surfaces. In the coarse grinding stage, these grains touch the substrate and deform local areas, especially at the tape edge. When the local strain exceeds a certain threshold, small pieces of REBCO chip off from the buffer layer and leave holes behind.

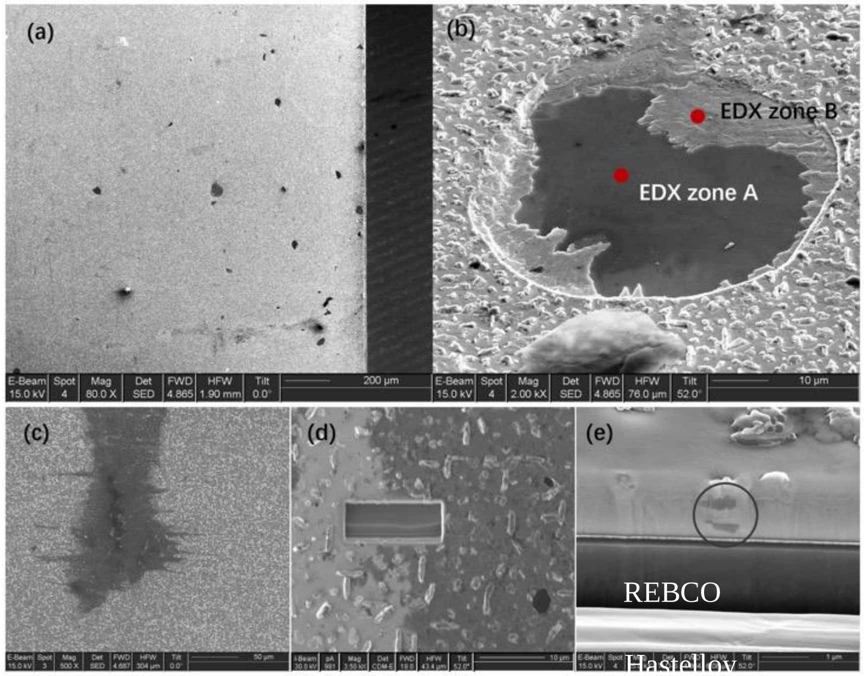

(a) (b) Chipping-off damage; (c) (d) (e) In-layer damage

Fig. 2-9 SEM examination of weak region of thin tape

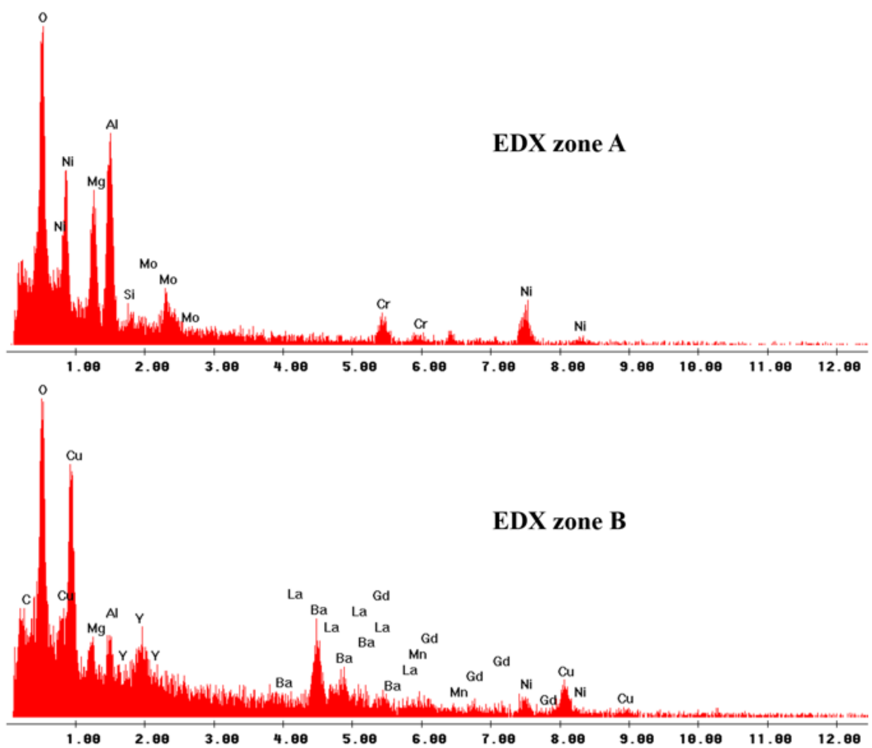

Fig. 2-10 EDX results at two areas in chipped region

The second kind of damage happened inside the REBCO layer. Areas with different surface morphologies and reflections, as shown in Fig. 2-9 (c), were observed. Focused ion beam was used to cut through REBCO layer at the edge of the abnormal area to examine its cross-section. The corresponding SEM micrographs are shown in Fig. 2-9 (d) (e). A few defects, which might have formed during MOCVD deposition, grew through the whole REBCO layer. Newly-created cracks in the circle clustered near the defects. It is believed that during the grinding process, stress is concentrated in the REBCO layer where defects are located. After repeated stress create-and-release cycles, small cracks are gradually created in weaker areas of the REBCO layer and the local current-carrying capacity decreases accordingly.

2.1.4 Improved reel-to-reel grinding process

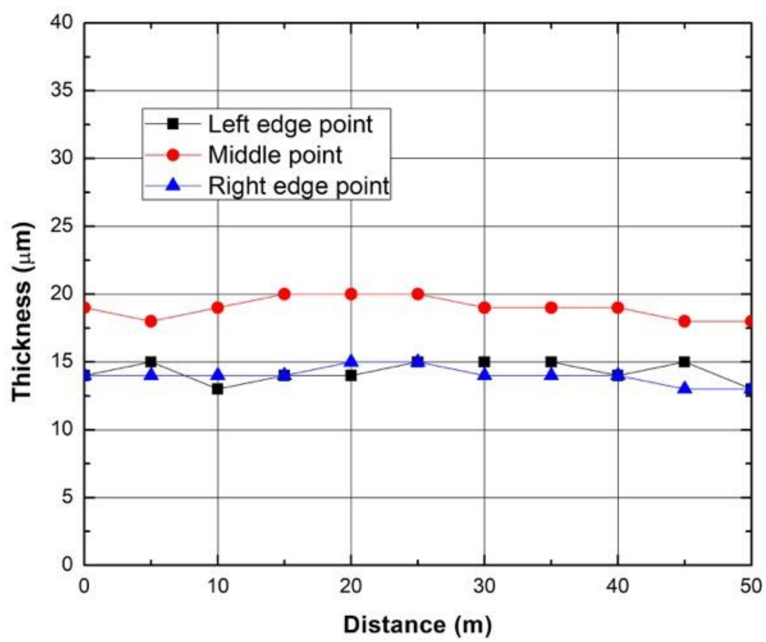

Fig. 2-11 Thickness of 65 m ground tape under new grinding parameters

Based on the analysis of the ground tape's weak region, several improvements were adopted in the R2R grinding process. Only 80 and 120 grit grinding wheels were used for coarse and fine grinding, respectively; 60 grit wheels were omitted to avoid local strain concentration. Tension and the grinding wheel RPM were optimized as well. These less-aggressive grinding parameters helped to prevent excessive tension in the REBCO layer.

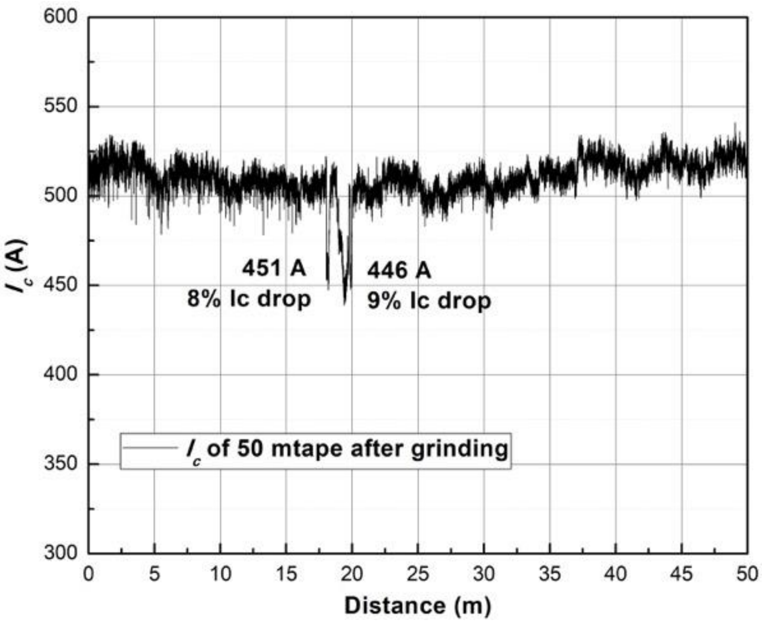

Fig. 2-12 Calculated I_c value of 50 m tape after grinding

A 50 m long 12 mm wide SF12050, also from SuperPower Inc., was ground using the new grinding parameters. After 18 turns of grinding, the tape thickness in the middle was reduced to around 20 μm. The thickness measurement data are plotted in Fig. 2-11. With the improved grinding parameters, the ground tape maintained the same level of uniformity across both its width and length at a thinner thickness. The thickness in the middle points was in the range of 18-20 μm, and both edges were 13-15 μm thick. The I_c value after grinding was measured by reel-to-reel SHPM and is shown in Fig. 2-12. With less tension and stress concentration in the REBCO layer, the I_c uniformity improved drastically. Only two adjacent areas across the tape's 50 m length had a less than 10% I_c drop. The tape in the other location maintained the same I_c value before and after grinding. The improved grinding parameters were used for producing all the symmetric tapes described in the dissertation unless otherwise stated.

2.2 REBCO tape laser slitting

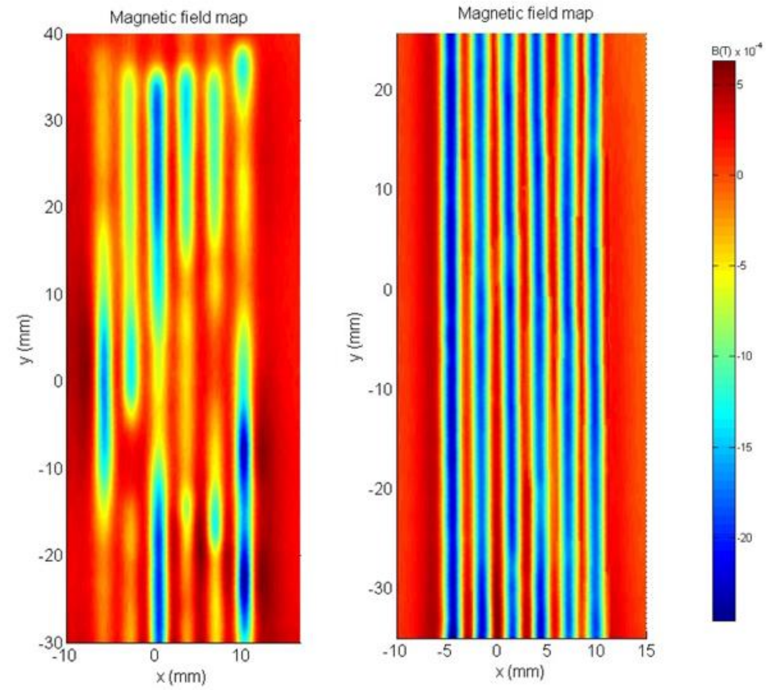

(a) Mechanical slitting; (b) Laser slitting

Fig. 2-13 SHPM trapped magnetic field plots of two slitting methods

To wind on a small core without overlapping, a narrow tape, rather than the original 12 mm tape, is needed. For instance, on a 20 AWG (0.79 mm) core, the first layer of tape is limited to a width of 2 mm. Mechanical slitting by a metal shear cutter and laser slitting by an optical fiber laser were compared. Fig. 2-13 shows the SHPM magnetic field maps of mechanically-slit tapes (a) and laser-slit tapes (b) [89]. The width of each tape was 2 mm and the gap in between was 1 mm. The resolution of the scanning hall probe microscopy was 0.05 mm in the X (tape width) direction and 1 mm in the Y (tape length) direction, which enabled the detection of small defects. For the mechanically-slit samples, the inhomogeneity of the magnetic field distribution along the tape's length indicated random defects in the tape, which were caused by cutting shear stress. On the other hand, laser-slit tapes exhibited very uniform magnetic field distributions and many fewer defects.

Since almost no stress was concentrated at the edge of the tape, laser slitting was determined to be the superior method for slitting narrow tapes.

2.2.1 Laser slitting platform

An optical fiber laser marking machine was used for tape slitting. The wavelength was 1064 nm and the maximum output power was 20 W. A laser enclosure was established to accommodate a reel-to-reel tape movement system, which was integrated into the laser slitting machine, as demonstrated in Fig. 2-14 (a). The tape tension was controlled by the unwinding spool on the right side. After passing through a custom-made vacuum stage below the laser lens, slit narrow tapes were collected separately by two synchronized rewinding spools on the left side.

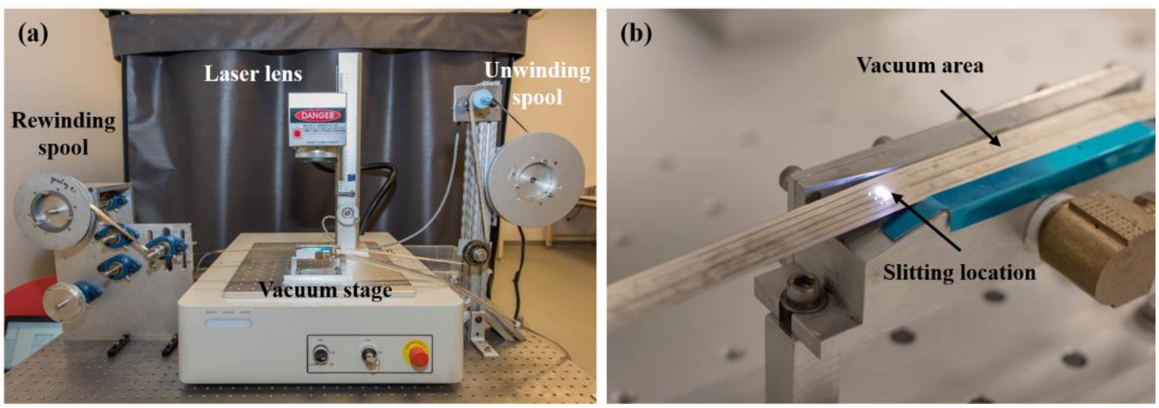

(a) Laser machine with integrated R2R system; (b) Vacuum stage

Fig. 2-14 Laser slitting platform

Because of the different thicknesses of the middle and edge locations, the ground tapes were slightly curved. The vacuum stage, which is shown in Fig. 2-14 (b), was used to flatten the tape before slitting. The slitting zone was next to the stage surface, with enough space under the tape to accommodate the melted particles.

To get a smaller laser dot after focusing, the standard 160 mm laser lens was changed to a 100 mm laser lens, which was the shortest focal length available for this laser. The size of the laser dot can be expressed as

$$w_0 = \left(\frac{2\lambda}{\pi}\right) \cdot \left(\frac{F}{D}\right), \tag{2-1}$$

and the corresponding depth of field can be expressed as

$$t = \left(\frac{8\lambda}{\pi}\right) \cdot \left(\frac{F}{D}\right)^2, \tag{2-2}$$

where w_0 is the diameter of the focused laser dot, F is the incident light diameter, D is the focal length of the lens, and t is the depth of field. With the same incident light diameter of 5.7 mm, after changing to the 100 mm lens, the laser dot size decreased from 19.0 µm to 11.9 µm and the depth of field decreased from 2.1 mm to 0.8 mm. The smaller laser dot yielded a higher slitting accuracy and fast slitting speed, while also requiring a more accurate focus.

2.2.2 Laser slitting optimization

2.2.2.1 Slitting parameters

With the help of the short focus lens, the laser focuses on the surface of the REBCO tape and generates very high temperatures to gasify materials and cuts through the tape. However, a part of the gasified material re-condenses at the surface of the slit tape and forms a rough edge. To minimize the roughness after laser slitting, different laser parameters were studied. Among the numerous adjustable parameters, pulse width and Q frequency are the most important. The pulse width controls the time duration of each laser pulse and the value is between 4 and 200 µs. The Q frequency is the number of pulses sent out per second and ranges from 1 kHz to 200 kHz. Both parameters control the power density of each single laser dot and thus affect the edge roughness.

Fourteen pieces of 50 µm Hastelloy tapes were slit in stationary mode; the test results are listed in Tab. 2-2. For each parameter combination, two samples were slit to reduce accidental error. The tape edge roughness was read by a surface profiler. Samples 1, 2, and 3 were slit at pulse widths of 200, 100, and 50 µs, respectively. Since the center frequency of the laser changes at different pulse widths, the Q frequency was set at the corresponding center frequency to achieve the highest efficiency. The output power percentage was set at the level where the sample was cut through by 10 passes. The results show that as the pulse width decreased, the edge roughness gradually increased. This is because a narrow pulse width releases energy in a short time and the high energy density gasifies too much material during a single pulse. The gasified material does not have enough time to escape from the slitting point and therefore re-condenses at the tape edge. In contrast, a longer pulse width gasifies the material in a relatively uniform way such that gasified material is able to escape into the surroundings.

Tab. 2-2 Tape edge roughness with different laser slitting parameters

Sample	Pulse width (μs)	Q frequency (kHz)	Output power (%)	Tape edge roughness (μm)	
				Left	Right
S1-1	200	40	30	6	7
S1-2				7	6
S2-1	100	60	40	10	10
S2-2				10	14
S3-1	50	90	70	17	18
S3-2				11	12
S4-1	200	20	60	10	11
S4-2				12	12
S5-1	200	40	30	5	9
S5-2				9	7
S6-1	200	60	60	10	10
S6-2				10	9
S7-1	200	80	100	11	10
S7-2				6	15

Samples 4 to 7 were slit at the best pulse width, which was 200 μs. The Q frequency ranged from 20 to 80 kHz and the output power percentage was set under the same principle as for samples 1 to 3. For samples other than S5, the Q frequency deviated from the center frequency of 40 kHz and higher output power was needed to compensate for the deviation. Edge roughness changes due to the different Q frequencies were not as obvious as changes due to the pulse width, but S5, using the lower power output, had the least rough edge. In conclusion, longer pulse widths with a Q frequency at the center frequency yield the best results. Notably, for reel-to-reel slitting, higher output power is required than for stationary slitting.

2.2.2.2 Laser slitting pattern

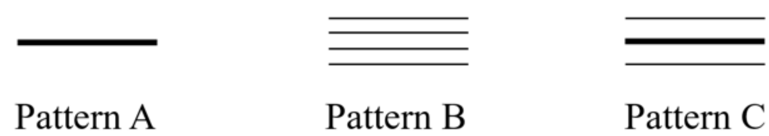

Fig. 2-15 Three laser slitting patterns

Tab. 2-3 Tape edge roughness of different laser slitting patterns

Pattern	Sample number	Tape edge roughness (μm)	
		Left	Right
A	S8-1	5	16
	S8-2	3	18
	S8-3	3	10
B	S9-1	6	9
	S9-2	7	6
	S9-3	7	11
C	S10-1	9	9
	S10-2	9	13
	S10-3	5	6

To further reduce edge roughness, three laser patterns for reel-to-reel slitting were tested, as plotted in Fig. 2-15 Three laser slitting patterns. Pattern A, the original pattern, contained four overlapping lines. Pattern B had four separate lines with a 10 μm distance between the center of each lines, whereas Pattern C had two overlapping lines in the middle and two separate lines that were 15 μm apart from the center. The idea of Patterns B and C was to use separate lines to gasify the re-condensed material and reduce edge roughness. Since all the patterns contained the same number of lines, the cutting speed was the same.

Nine pieces of 25 μm thin REBCO tapes, three for each pattern, were slit in reel-to-reel mode. The samples were slit from the Hastelloy side and the edge roughness was read on the REBCO side. The laser pulse width was 200 μs, the Q frequency was 40 kHz, and the power output was 40%. The results are summarized in Tab 2-3. During the reel-to-reel motion, the tape was slightly tilted to one side, which is why the right edge was rougher than the left edge. For Pattern A, the laser slit at the same line repeatedly and resulted in re-condensation of the material, which grew to more than 15 μm thick. For Pattern B, since the laser dot size was comparable to the distance between each line, there was 40-50% slitting line overlap. In this pattern, each line was slit at the edge of the previous line so that the re-condensed material could be removed effectively. The average edge roughness was 7 μm. Pattern C's results were similar to those of Pattern B, with a slightly rougher edge of 9 μm, on average. The two overlapping lines in the middle did not reduce the rough edge as effectively as the two lines at the edge. Therefore, Pattern B, with four separated lines, was the most effective pattern for reducing edge roughness.

2.2.2.3 Tape edge SEM examination

The high temperature during laser slitting not only gasifies material, but also causes local stress. It is important to ensure that the REBCO layer is not damaged during slitting. SHPM examination has already been demonstrated in Fig. 2-13; therefore, direct examination by SEM on the REBCO layer was conducted. Fig. 2-16 is a SEM image of the edge of sample S9-1 [90]. The silver layer was etched to expose the REBCO layer. A porous structure in the REBCO layer was found near the slitting edge due to the large thermal stress, but was limited to a range of only 2-3 μm. Compared to the 2 mm width of the narrow tape, the damaged area was negligible.

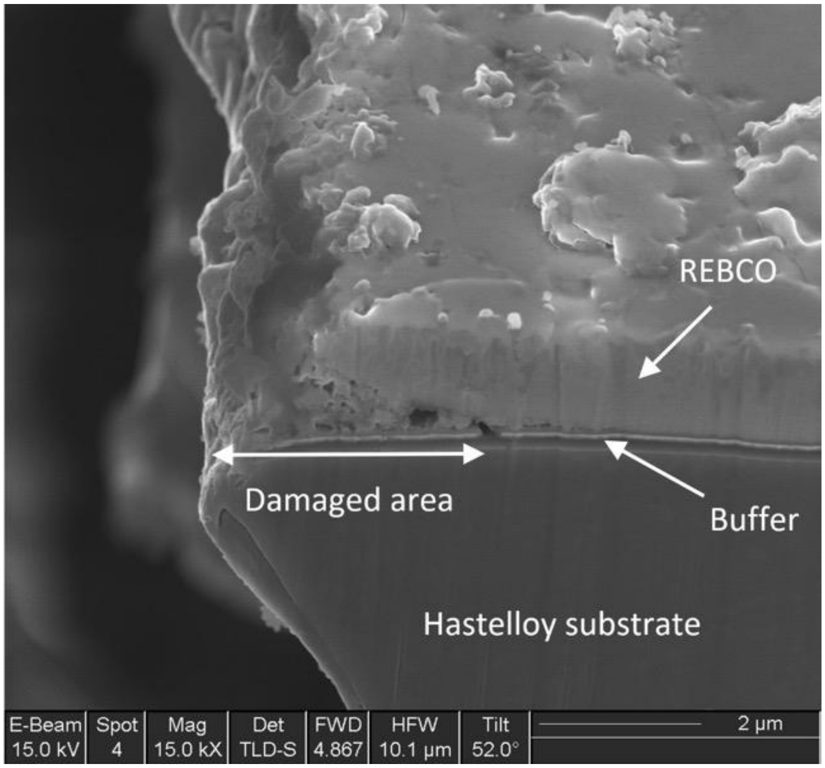

Fig. 2-16 SEM image of the edge of sample S9-1

2.3 Copper electroplating

After the 12 mm tape was slit into narrow tapes, reel-to-reel silver sputtering was first applied to cover the exposed edges and prevent delamination. The sputtered silver was about 2 μm thick on the REBCO side and 1 μm thick on the substrate side. Afterward, a certain thickness of copper was electroplated on the REBCO side of the tape to obtain a symmetric structure. A reel-to-reel DC electroplating system with water-based $CuSO_4$ solution was employed.

2.3.1 Reel-to-reel electroplating system

The electroplating system is shown in Fig. 2-17 (a). The system consists of four components to control tape movement, electroplating, electrolyte circulation, and tape post-cleaning, respectively. In the middle of the system is the electroplating cell, as shown in Fig. 2-17 (b), and two electrical contact cells. Since the resistivity of REBCO tape is mainly determined by the Hastelloy substrate, which has a resistivity of 1.3 mΩ·m [91], current can flow through the tape without generating too much heat. The tape is used as a cathode by itself and current is conducted by two pairs of brass brushes in the electrical contact cells. One or two titanium baskets filled with copper billets are installed on the side of the electroplating cell as anodes. For single-side electroplating, only one anode is needed. The electroplating current is supplied by a 120 W DC power station with 0.01 A accuracy.

(a) Overview of the entire system; (b) Electroplating cell

Fig. 2-17 Reel-to-reel electroplating system

After passing through the electroplating cell, the tape is rinsed with DI water and heated to 80 ˚C to remove any remnant electrolytes. This process keeps the tape surface clean and prevents any possible galvanic reactions after electroplating. Under the electroplating cell is the electrolyte and DI water reservoirs. The electrolyte is heated and circulated to the electroplating cell with enough agitation to avoid local ion depletion. The system is designed for large-scale electroplating, and so the electrolyte reservoir is 100 L in volume to keep the solution concentration constant.

The formula of the 100 L of water-based electroplating solution is listed in Tab. 2-4. In addition to $CuSO_4$, $NaSO_4$ is added to reduce the electrolyte resistance. The less-resistive electrolyte near the cathode decreases the overpotential from ohmic resistance, which makes electroplating more feasible [92]. Sulfuric acid is used to acidify the electrolyte. The solution's low pH value not only further reduces the electrolyte resistance, but also reduces the polarization impedance of the copper ion transfer process, which results in better bonding between the copper and silver and finer copper grains. Fig. 2-18 compares the surface morphology of copper electroplated in electrolyte solutions with different pH values. When the pH was reduced from 4.5 to 2.5, the typical surface roughness decreased from 68.13 μm to 13.68 μm, i.e., it yielded a much finer copper surface. However, further reducing the pH value may damage the REBCO layer; consequently, the pH value was kept between 2.5 and 3.0. The temperature in the electroplating process is an important factor since it affects surface roughness as well. At higher temperatures, copper ion diffusivity is greater, which results in a finer surface. When electroplating long tapes, however, high temperatures cause fast evaporation of the solution and thus variations in the solution concentration. Therefore, the temperature was set at 40 ˚C to balance the surface smoothness and long-length electroplating capability.

Tab. 2-4 100 L electroplating solution formula

$CuSO_4 \cdot 5H_2O$	19.5 kg
$NaSO_4$	2.5 kg
H_2SO_4	30 mL
DI water	100 L
pH	2.5-3.0
Current density	<5.5 mA/mm^2
Temperature range	25-55 ˚C

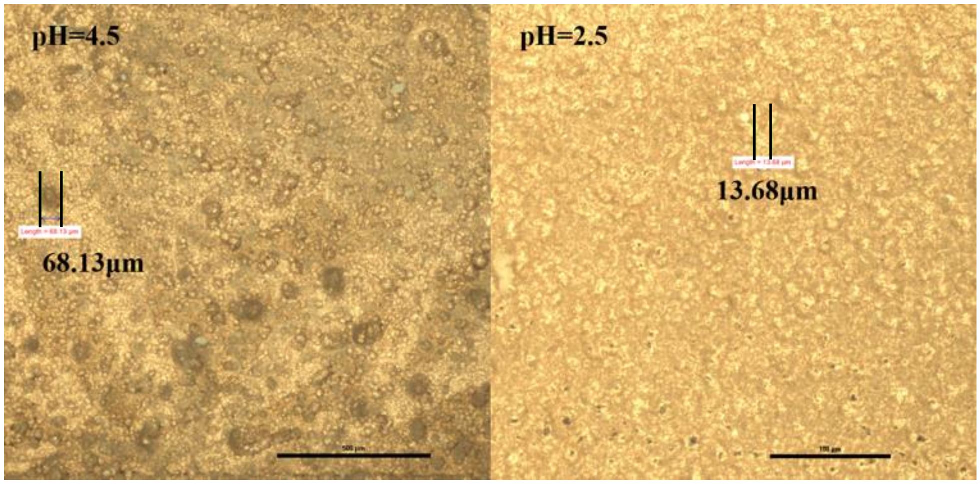

Fig. 2-18 Optical micrographs of surface of copper electroplated with two different pH solutions

2.3.2 Copper quality control

2.3.2.1 Copper thickness

The theoretical thickness of electroplated copper is expressed as a variant of Faraday's laws of electrolysis [93],

$$t = \frac{M_{Cu}Jt}{2\rho F}, \quad 2\text{-}3$$

where t is the copper thickness, M_{Cu} is the molar mass of copper, J is the current density, t is the electroplating time, ρ is the density of copper, and F is Faraday's constant. In reel-to-reel electroplating at a given tape speed, the electroplating time, which equals the amount of time that the tape passes through the electroplating cell, is constant. As a result, the theoretical copper thickness is proportional to the current density.

Five 2 mm wide REBCO tapes were electroplated at different current densities. The Hastelloy side of the tapes was covered by a simple Teflon straight piece to ensure that most of the copper was deposited on the REBCO side. During tape movement, some electrolyte flowed between the tape and the Teflon piece, therefore 1-2 μm of copper deposited on the back side of the tape but did not change the total copper thickness. The tape movement speed was set at 4 cm/min and the corresponding electroplating time was 7 min. The current ranged from 0.5 A to 2.5 A at 0.5 A intervals. After electroplating, the copper thickness was measured at both the center and edge of the tape with a micrometer. The results are plotted in Fig. 2-19. At low current density, the measured tape thickness corresponded well with the theoretical values; however, as the current density increased, the thickness in the middle of the tape was less than the theoretical value, whereas the thickness at the edge was higher than the theoretical value. The thickness difference between the middle and edge points at the highest current density (4.5 mA/mm^2) was 59 μm. The tape also had a very rough edge, as displayed in Fig. 2-20. Copper dendrites were found at the tape edges

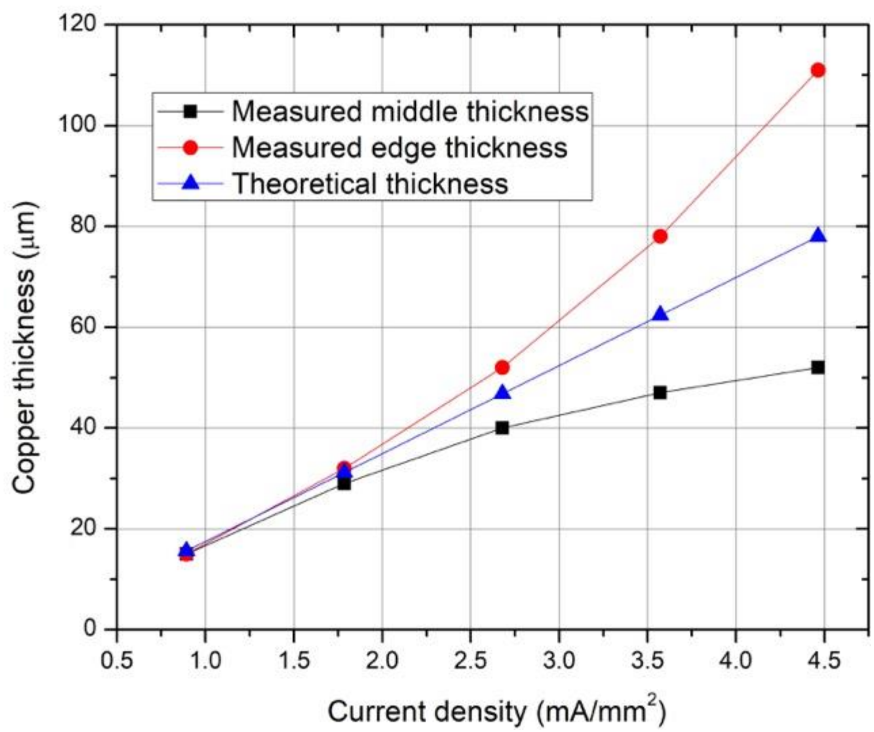

Fig. 2-19 Tape thickness at different electroplating current densities

Fig. 2-20 Rough edge of electroplated tape with simple plate cover

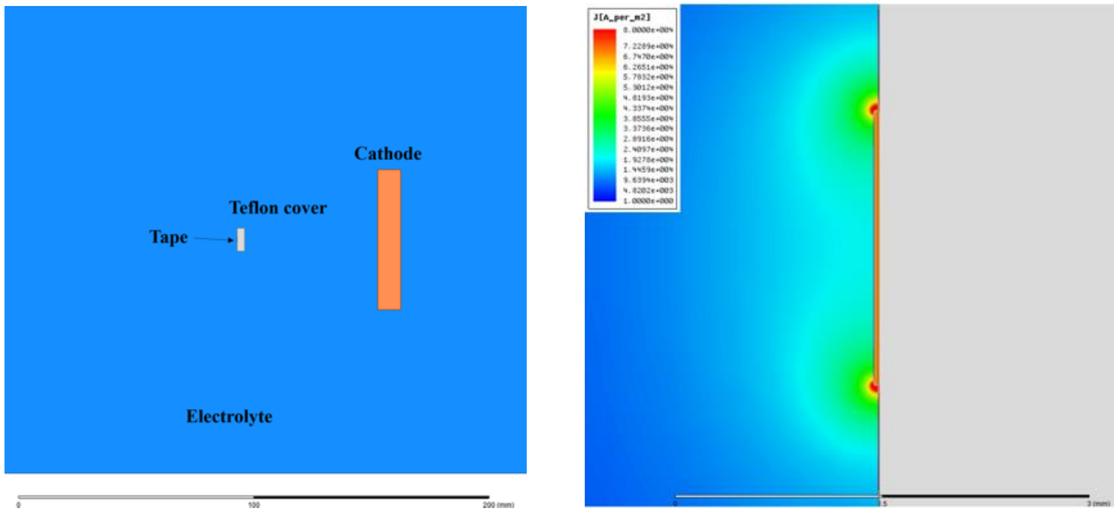

(a) 2D model of electroplating cell; (b) Current density distribution

Fig. 2-21 Simulation of current density with Teflon plate cover

To explain the abnormal copper thickness, a 2D simulation of the current density in the electrolyte was carried out. In the Ansoft Maxwell 14 DC conduction module, a cross-section model based on a real-size electroplating cell was built, as shown in Fig. 2-21 (a). The tape was 0.03×2 mm and located in the center of a 200×250 mm cell. The copper cathode was 10×60 mm and located 60 mm away from the tape. A 3×10 mm Teflon piece covered the back side of the tape. Based on the electrolyte concentration, the conductivity was set at 200 mS/cm [94]. Due to the extreme aspect ratio of the tape, an extra-small 4 μm mesh was used to accurately simulate the current distribution. The cathode was excited by a 5 V DC power source. The simulation result of the current density distribution near tape is plotted in Fig. 2-21 (b). Because of the large potential gradient, the current density at the tape edge was much higher than in the middle position, which was directly related to the faster copper deposition rate. As the copper became thicker at the edges, dendrites started to grow and they, in turn, sped up the copper deposition, which is why the copper thickness deviated further from the theoretical value at higher current values.

2.3.2.2 Shield design for single-side electroplating

One obvious approach to change the current distribution on the tape surface is to modify the shape of the Teflon piece. A Teflon shield with a groove on its surface to accommodate the tape was proposed to solve the current distribution issue. As demonstrated in Fig. 2-22, the Teflon shield fully covered the backside and edges of the tape. With proper groove shape, current flux in electrolyte was guided vertically to the tape surface, avoiding concentration at the tape edges. The Teflon shield was connected by two threaded rods to secure its position in the electrolyte. Several Teflon shields with different groove widths were designed to accommodate tapes of various widths.

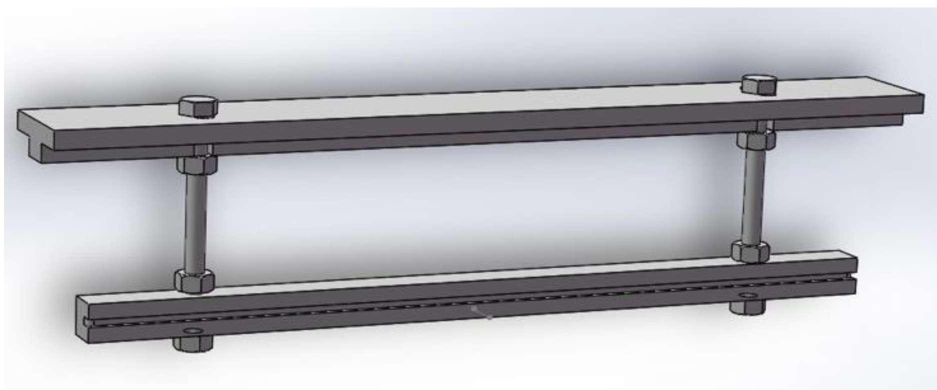

Fig. 2-22 Teflon shield for single-side electroplating

For a 2 mm wide tape, shields with groove widths from 2.1 mm to 2.7 mm were simulated. To avoid copper ion depletion, the groove depth was the same as the groove width. A simulated current density distribution at a groove width of 2.1 mm is shown in Fig. 2-23 (a). With the help of groove guidance, the current was almost uniformly conducted to the entire tape surface. Compared to Fig. 2-21 (b), no hot spot was concentrated at the tape edge. Current density distributions along the tape surface for different groove widths are plotted in Fig. 2-23 (b). At the 2.1 mm groove width, the current density at the tape edge was only 5.3% higher than the average value. The majority of the tape surface has a very uniform current distribution. As the width increased, the effect of the shield became weaker. At the 2.5 mm groove width, the edge had 48% higher current density, which meant that the shield almost lost its effect. In the real situation, however, the tape width varied slightly from batch to batch. Wider tapes might get stuck in grooves with exact widths. For this reason, a groove width of 2.2 mm was finally selected for the 2 mm tape electroplating shield.

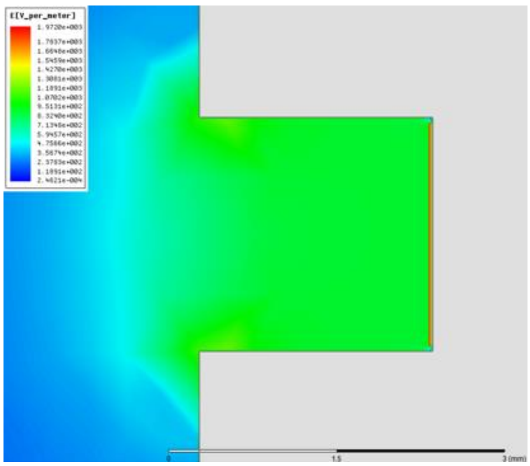

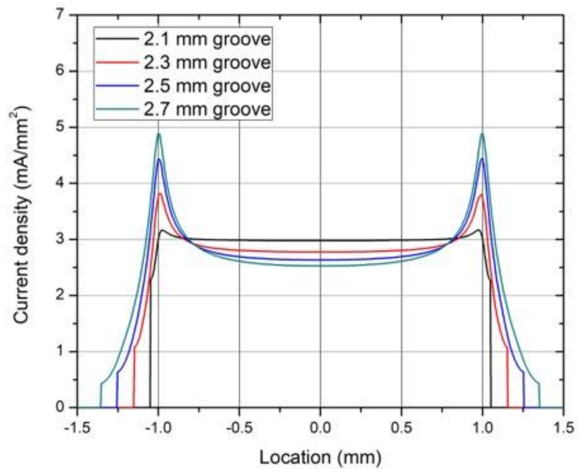

(a) Uniform current density in groove; (b) Current density distribution along tape surface

Fig. 2-23 Current density distribution with modified Teflon shield

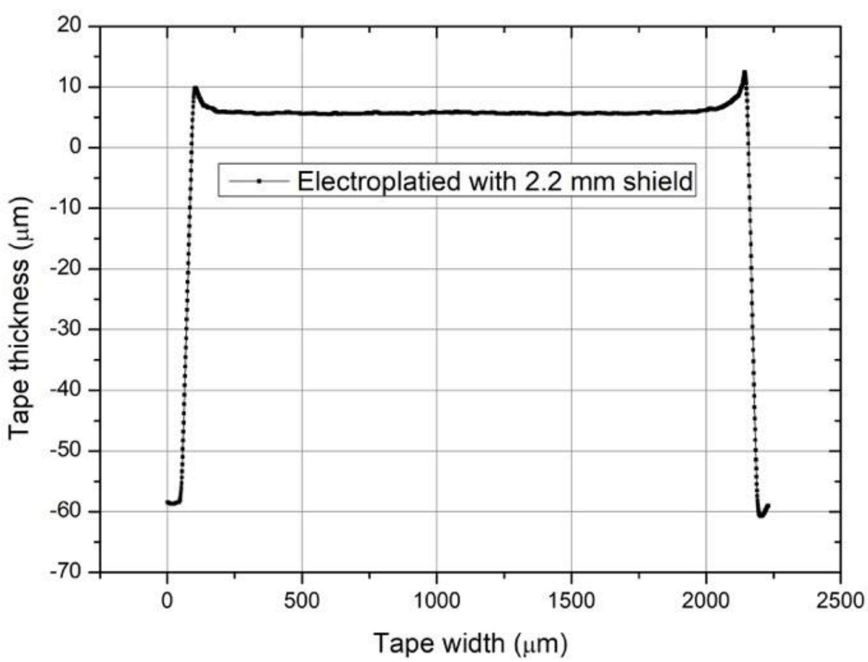

Fig. 2-24 Tape thickness of electroplated tape with improved shield

One piece of 30 μm thick, 2 mm wide tape was electroplated with a shield with a 2.2 mm wide groove to verify the simulation. The electroplating current was 1.1 A with a corresponding current density of 1.96 mA/mm^2. The tape movement speed was 4 cm/min. After electroplating, a surface profiler was used to read the tape thickness and the result is plotted in Fig. 2-24. Compared to the data in Fig. 2-23 (b), the measured thickness corresponded well with the simulation. In addition, with minimal edge roughness, the middle thickness of 34 μm was also in good agreement with the theoretical thickness of 34.5 μm.

2.4 STAR wire winding

The previous three sections discussed the fabrication of symmetric tape in detail. This section presents the STAR wire winding process. In early development, short-length STAR wires were manually wound. Wire structures with and without terminals were utilized. Multi-layer STAR wires with lengths less than 10 cm showed promising performance; however, the manual winding was not consistent, which affected the performance of longer-length STAR wires. Based on the data collected during manual winding, an automatic winding machine was developed, which allowed for the precise control of several winding parameters, such as tension and wrap angle, to produce long STAR wires with stable performance.

2.4.1 Manual winding process

2.4.1.1 Wire without terminal

The initial winding stage was constructed with aluminum extrusions, as shown in Fig. 2-25 (a) (b). The distance between the two aluminum plates was adjustable in order to wind STAR wires with different lengths. Brass or copper rods fixed to the aluminum plates were used as wire formers. Because the REBCO conductor can sustain a much higher compressive strain than tensile strain before irreversible I_c degradation occurs, symmetric tapes were wound with the copper layer facing inward. Manual winding takes the following steps. One symmetric tape is first fixed to the aluminum plate by Kapton tape at a certain angle to the copper wire former. Then, the tape is wound by hand at a predetermined twist pitch until it reaches the second aluminum plate. After fixing the second end with Kapton tape, the junctions between the tape and former are glued by Loctite 404 super glue. This process is repeated several times until enough layers are wound. Fig. 2-25 (c) shows a 2-layer sample in progress. Based on this structure, a large number of STAR wires were fabricated to study the tape bending properties and I_c retention, which was defined as the ratio of the tape I_c in the bending form to the I_c in the straight form. Various parameters, such as copper thickness, twist pitch, and former diameter, were studied and are discussed in Chapter 3.

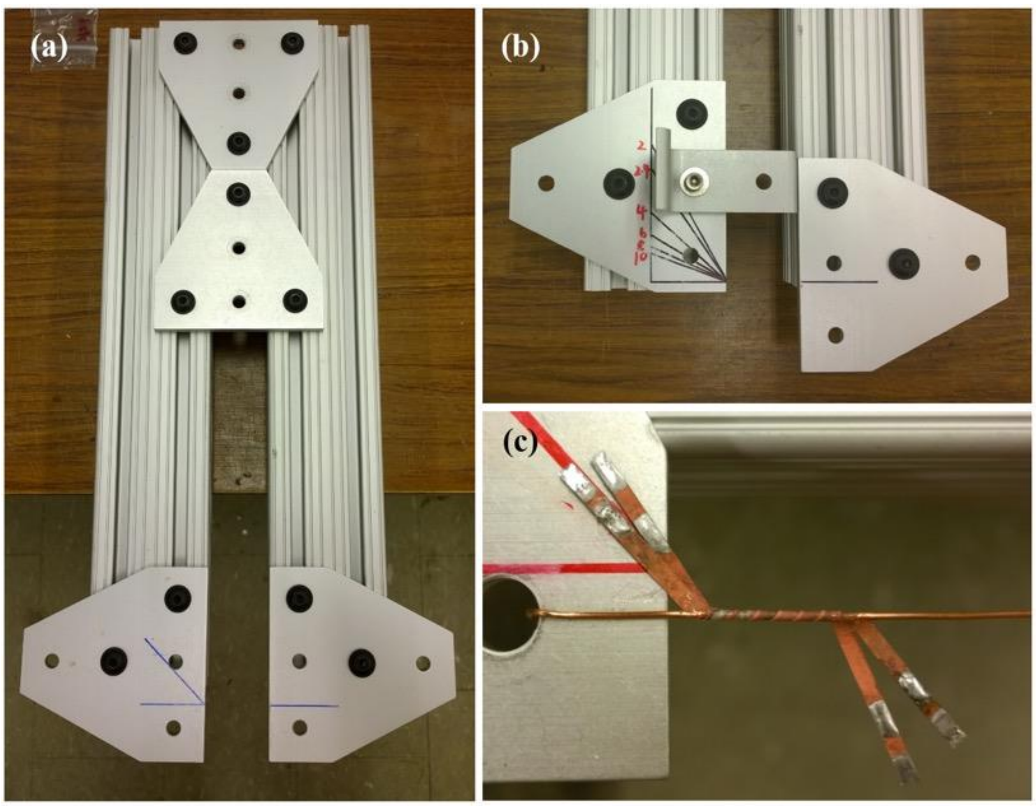

(a) (b) Winding platform structure; (c) 2-layer sample in progress

Fig. 2-25 STAR wire manual winding platform

Fig. 2-26 demonstrates two typical 6-layer STAR wires, where Wire-A was wound in the alternating direction in each layer and Wire-B was wound in the clockwise direction in all layers. The structure of Wire-A was also called a crisscross structure, which is a standard weaving structure for a round conductor; this structure provides better mechanical strength while maintaining a partially transposed structure. The structure of Wire-B was easier to test since the ends of all the layers were gathered together. Wire-A was made in the early period and the outer diameter was 3.4 mm. It was wound on a 1.1 mm diameter brass rod and 3 mm twist pitch for 6 turns in total. After a lot of parametric study and optimization, Wire-B had an outer diameter of 1.71 mm. It was wound on a 0.8 mm diameter copper rod at a 45-degree twist angle for 6 turns in total.

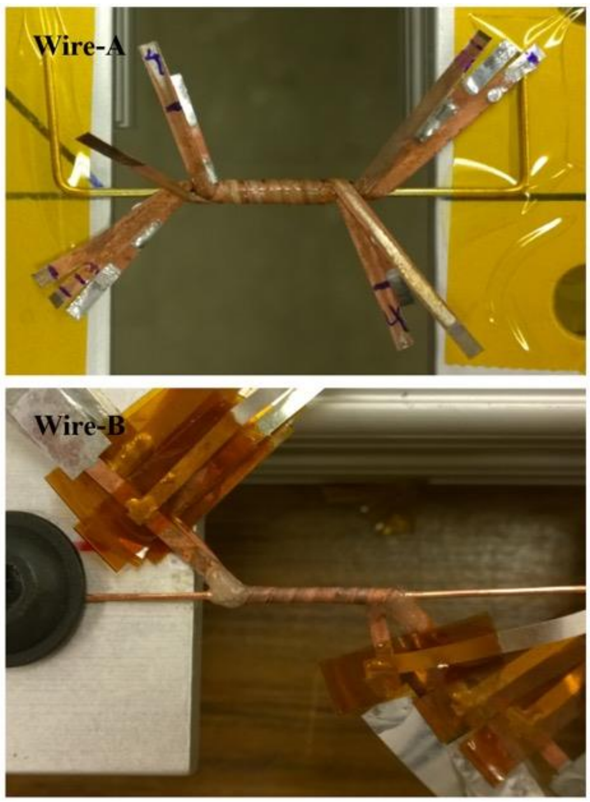

Fig. 2-26 Two typical 6-layer short STAR wire

The I_c of each tape in Wire-A was first measured in the straight form and then measured again individually after winding. The *I-V* curves of Wire-A are plotted in Fig. 2-27, where solid dots represent the voltage in the straight form and the hollow dots represent the voltage in the bending form. The distance between the two voltage taps was 3 cm along the tape surface and 1 μV/cm was used as the critical current criterion. As can be seen from the plots, the straight tape I_c values were between 57 A and 64 A and relatively uniform. However, the I_c retention after winding randomly ranged from 4% to 79%. The third layer, which only retained 2 A of current after winding, basically lost superconductivity. While certain layers, such as layer 1 and 2, showed good bending properties, the results were not consistent. This issue was caused by the unstable nature of hand winding since the winding tension for each layer was difficult to maintain at a constant value.

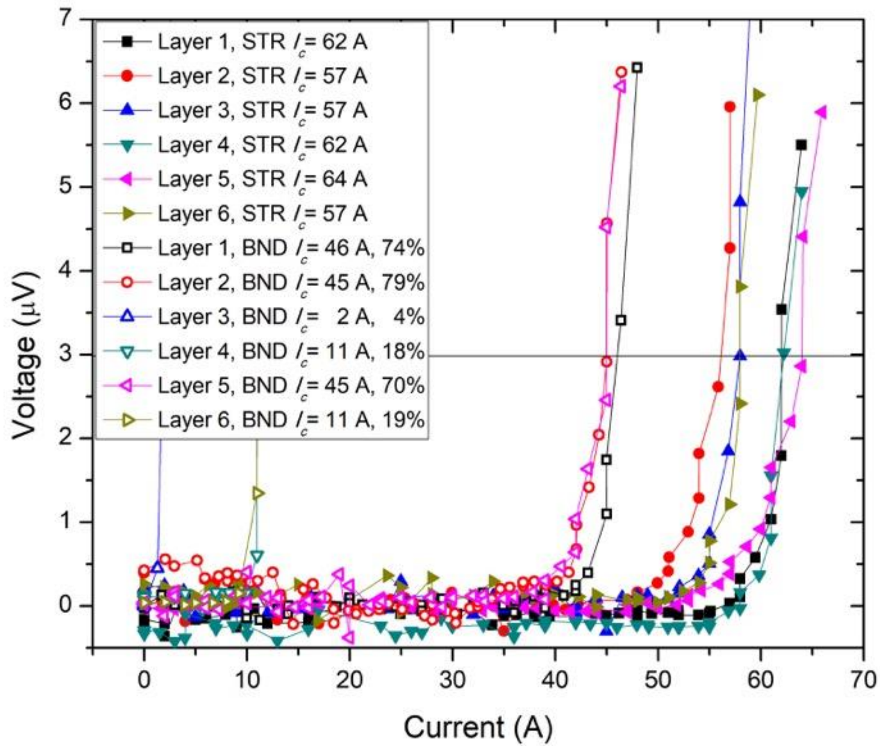

Fig. 2-27 *I-V* plots of each tape in Wire-A

The same I_c retention measurements were carried out on Wire-B and the results of both the straight and bending forms are plotted in Fig. 2-28. The I_c retention of each layer was between 79% and 94%, which was much more uniform than that of Wire-A. This improvement was the result of the copper thickness optimization and better tape handling techniques. Unlike a constant copper thickness used for all layers in Wire-A, Wire-B had an optimal copper thickness for each layer, which will be explained in detail in next chapter, and the average I_c retention was improved to 87% accordingly. Careful handing during winding also helped to avoid accidental tape damage, such as that happened to the layer 3 in Wire-A. In addition, the structure of the same winding direction of in Wire-B resulted in gathering all the tape ends together and made the I_c test less complicated, which also reduced the chance of tape damage during testing.

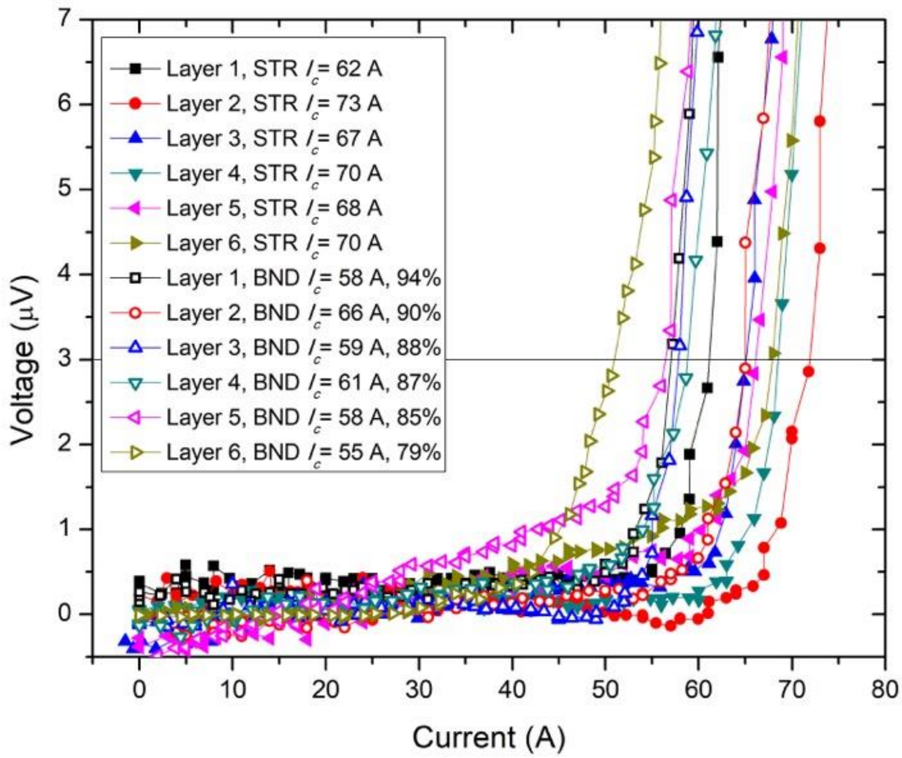

Fig. 2-28 *I-V* plots of each tape in Wire-B

2.4.1.2 Wire with terminals

STAR wires without terminals are suitable for studying an individual layer's performance, but terminals are essential for using STAR wires in real applications since they are crucial for current distribution and sharing between tapes. Another benefit of soldering tape to terminals is a stronger structural strength since no Loctite glue or epoxy is used during winding. Two terminal structures were used for manual winding; their schematic designs are shown in Fig. 2-29. The conical terminal was compact in size, whereas the plate terminal provided a smooth transition from the wire to the terminal. Both designs had large tape soldering areas for a low terminal resistance. The winding process for wire with terminals was the same as the process described in section 2.4.1.1 except solder was used instead of Loctite glue to fix tapes. Based on these designs, a 7.5 cm long, 6-layer STAR wire was able to carry an I_c of 283 A with a corresponding J_e of 141 A/mm^2. The results will be discussed in Chapter 4.

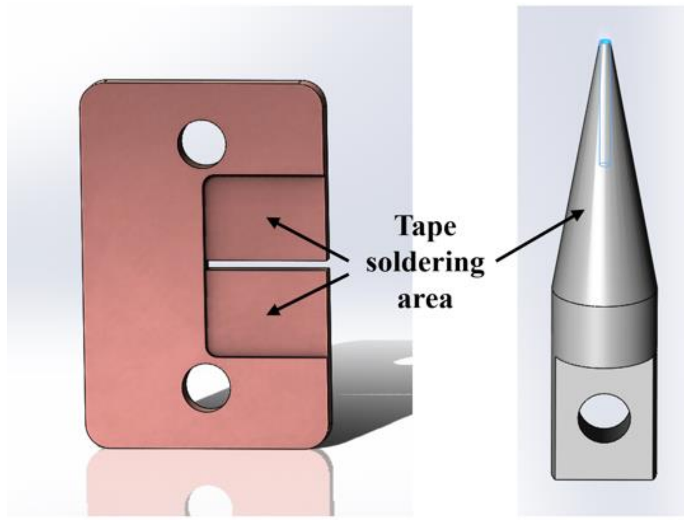

Fig. 2-29 Two terminal structures used in manual winding process

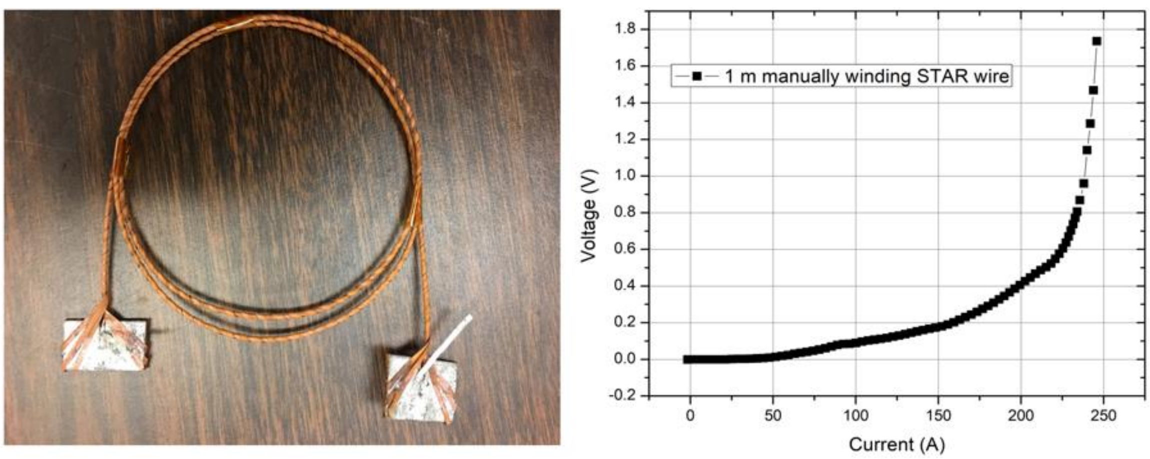

(a) 1 m of manually wound STAR wire; (b) Full transition *I*-*V* plot

Fig. 2-30 Manually-wound 1 m STAR wire

While manual winding is suitable for short sample fabrication, manually winding longer wires results in inconsistent performance. When the STAR length increases from less than 10 cm to the order of meters, the chance of damaging a tape during manual winding also increases substantially.

For multiple-layer STAR wires, it is nearly impossible to manually fabricate a sample longer than one meter with good performance. Fig. 2-30 shows the picture of 1 m of a manually-wound 6-layer STAR wire and its corresponding *I-V* test result. Although no damage was found in the exterior, the performance of this wire was much worse than the short sample with the same structure. If a critical current criterion of 1 μV/cm was used, the I_c was only 28 A. However, after increasing the stop voltage to 2 V, a full transition was observed. This indicated that a lot of damaged areas existed in the middle of the wire. To bypass the damaged area and share current between tapes, the large interlayer resistance caused a voltage drop of hundreds of millivolts before transition could be observed. Several kinks in the *I-V* curve also indicate that current redistribution occurred between the layers.

2.4.2 Automatic winding process

2.4.2.1 Automatic winding machine

To overcome the difficulties in manual winding, an automatic winding machine was developed. Winding parameters were precisely controlled and kept constant during the entire winding process. Fig. 2-32 shows a photograph of the automatic winding system. The copper former is stored on a storage spool, guided through the winding unit in the middle, and then wound on a collecting spool after winding.

Before winding, symmetric tapes are first stored on the winding arm spool. The winding tension is set to as low as 1 N to minimize extra bending stress on the tape. Based on the analysis of manually-wound samples, the wrap angle was kept at 45 degrees to minimize the influence of bending strain. To initiate STAR wire winding, one end of the tape is soldered with 60/40 tin lead alloy to the pre-tinned copper former with the REBCO side of the tape facing inward. A low wire movement speed (10 cm/min) is used in the beginning to ensure that no delamination or breakage happens. After initialization, the wire movement speed is gradually increased to full speed (25 cm/min). When the wire reaches the end, the other end of the tape is soldered to the copper former while the tape is still under tension. This process is repeated to fabricate a multi-layer STAR wire.

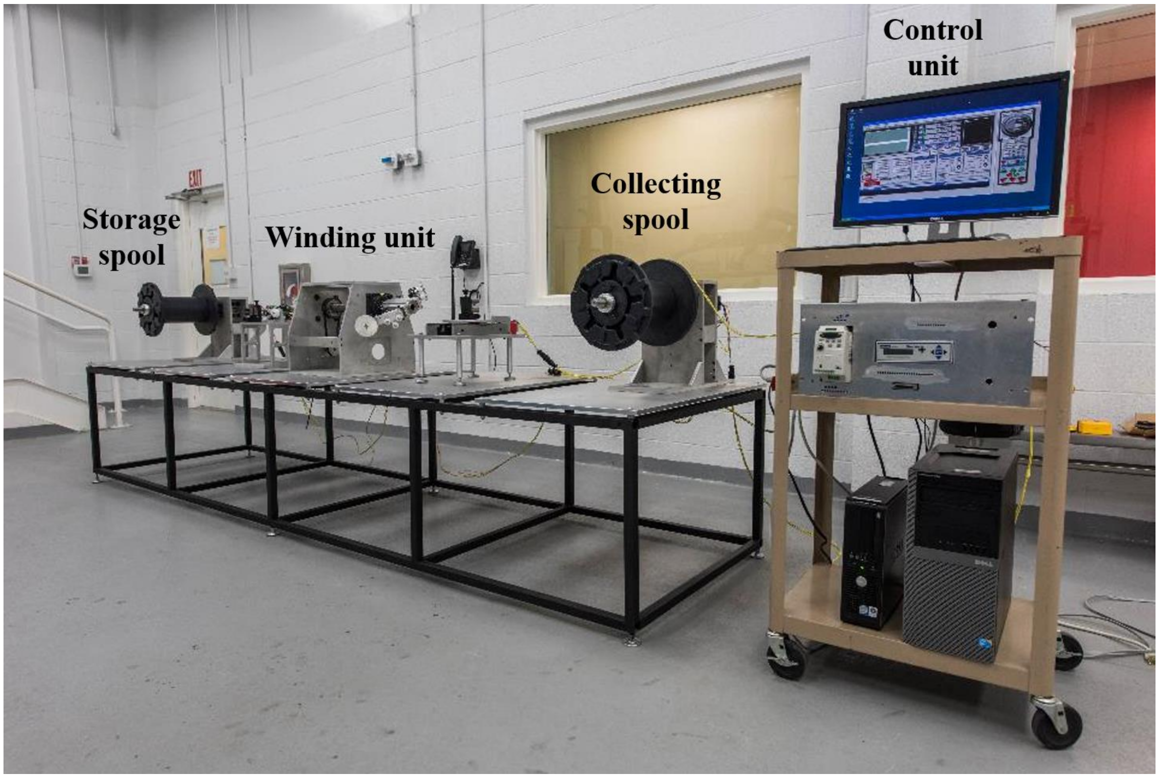

Fig. 2-31 Automatic winding machine

With the help of the automatic winding machine, the performance of long wire was drastically increased. In an initial test run, a 1 m long, 6-layer STAR wire was able to carry a current of 174 A, which was 6 times higher than the I_c of the manually-wound sample. The detailed results will be discussed in Chapter 4.

2.4.2.2 Terminal fabrication in automatic winding

The manual winding terminal structures discussed in section 2.4.1.2 are not applicable for automatic winding since a reel-to-reel process is used. A low-resistance, compact terminal is needed. Because it was quite difficult to solder multiple layers of tape in small space without damaging the tape, in early development Loctite 404 superglue was used to hold the tape ends, as demonstrated in Fig. 2-32 (a). Once cured, however, the superglue formed insulation layers between the tapes and prevented wetting of tapes to the solder material. The electrical contact between the wire end and copper terminal was poor.

(a) Wire end glued by Loctite 404; (b) Wire end soldered with tin lead alloy

Fig. 2-32 STAR wire end connection structures

After carefully improving the soldering uniformity and decreasing the pre-tin layer thickness, a soldered end was adopted, as shown in Fig. 2-32 (b). To expose each layer of the tape directly to the soldering material rather than the outer layer, a stage-shape structure was used. In this structure, the innermost layer was the longest and the outermost layer was the shortest; other layers had lengths between these two. For applications without space limitations, the length difference between the adjacent layers was 15 mm. Since the process for soldering wire to a copper terminal might be repeated several times, a layer of thin bare copper wire, in a crisscross structure, was wound to cover the whole soldering area and prevented tape unwinding during soldering. This stage-shape soldered end is compatible with the automatic winding machine while providing low contact resistance to the copper terminal. After winding, two ends of STAR wire are soldered to copper terminals for future testing.

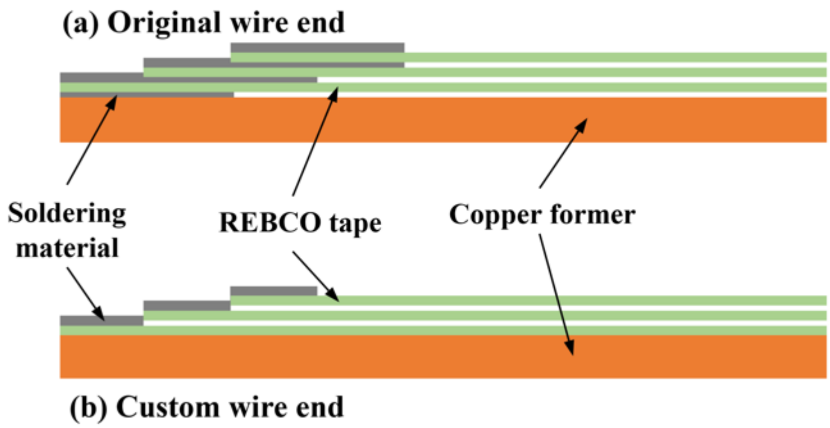

Fig. 2-33 Comparison of STAR wire ends

Fig. 2-34 Wire end remaking steps

Notably, for long-length STAR wire, in some cases the wire needs to be cut in the middle. The original STAR wire terminal provides the best electrical performance; however, custom terminals can be made to offer extra flexibility at the cost of higher resistance. Schematic of the original wire end and custom wire end are displayed in Fig. 2-33. During the wire end remaking, it is difficult for the soldering material to get under each layer as thoroughly as the original wire end, which results in higher resistance in custom terminals. The wire end remaking process, which uses an 8-layer STAR wire as an example, is as follows:

1. Determine the location of the new end on the STAR wire. It is recommended that the length of the custom end is not shorter than the original one. Shorter ends can be made but yield higher resistance; 5 mm of extra length is needed for the cutting operation.
2. Use Kapton tape and several turns of tightly wound thin copper wire to prevent the unwinding of the rest of the STAR wire. Shrink tubes and collars with soft inserts can also be used; the main idea is to provide enough pressure while not damaging the wire.
3. Mark the section of the 8^{th} layer on the new end. Mask the remaining area with Kapton tape and apply flux to the exposed area.
4. Tin the exposed area of the 8^{th} layer with 60/40 tin lead alloy. The lead tin layer should be thick enough to hold the tapes in position.
5. Remove the masking Kapton tape. Carefully cut the 8^{th} layer of tape at the further end at the 5 mm of extra area mentioned previously.
6. Carefully unwind the 8^{th} layer and then cut the tape next to the tinning area. The wire end making of the 8^{th} layer is done.
7. Repeat Step 3 to Step 6 until all 8 layers are exposed. Now the stage-shape wire end is formed.
8. Apply a thin bare copper wire in crisscross shape to cover the whole terminal area. This copper wire prevents terminal unwinding during soldering. Tin the copper wire and remove all other materials.

The corresponding photographs of the wire remarking steps are shown in Fig. 2-34.

Chapter 3. Electromechanical properties of symmetric tape

This chapter presents the electromechanical properties of symmetric tape. The bending strain and neutral axis, which are the fundamental concepts behind symmetric tape, are introduced in the beginning. Then, the structure of normal REBCO tape and the method for shifting the neutral axis are discussed. The efficacy of the neutral axis shifting is proven via bending tests on tapes with different structures. Because it is difficult to calculate the exact theoretical location of the neutral axis when plastic deformations are involved, a series of experiments was performed to determine the optimized copper stabilizer thickness. The influence of twist pitch on I_c is discussed at the end.

3.1 Symmetric tape structure

3.1.1 Bending strain and neutral axis in REBCO tapes

When a homogeneous beam is loaded by lateral forces, the longitudinal axes of the beam is deformed. The longitudinal lines on one side of the beam are under tensile stress and stretched, whereas the longitudinal lines on the other side of the beam are under compressive stress and compressed. In the middle of the beam, an axis that keeps its length unchanged and experiences no stress is called a neutral axis.

For objects that consist of different layers of material, such as the REBCO tapes, the locations of their neutral axes are determined by the thickness and mechanical properties of each layer. When only elastic deformation is involved, the location of the neutral axis can be calculated as follows [95]:

$$y_{neutral} = \frac{t}{2} - \sum_i E_i \gamma_i \frac{t_i}{2} / \sum_i E_i t_i, \tag{3-1}$$

where $y_{neutral}$ is the distance from the lowest surface of the tape to the neutral axis; t and t_i are the thicknesses of the whole tape and each layer, respectively; E_i is the elastic modulus of each layer; and γ_i is the relationship between the curvature and the stress at each layer. Correspondingly, the bending strain of a certain layer is expressed as

$$\varepsilon = \frac{y_{neutral}}{\rho} \times 100\%, \tag{3-2}$$

where ρ is the bending radius of the neutral axis.

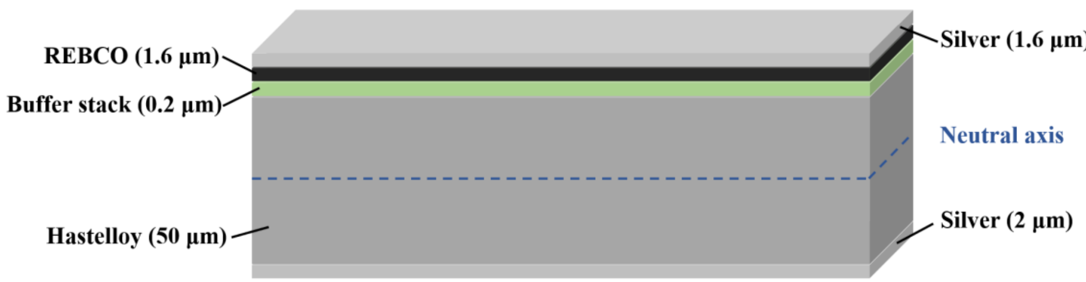

Fig. 3-1 Layer structure of Superpower SF12050 tape (not to scale)

Fig. 3-1 shows a cross-section of the structure of a Superpower SF12050 tape. It contains a 50 µm thick Hastelloy substrate and a 0.2 µm thick buffer stack. A 1.6 µm thick REBCO layer is deposited onto the surface of the buffer stack by MOCVD. Then, silver cap layers of 1.6 to 2 µm are sputtered onto both sides of the tape. Because of the small volume fraction of the other layers, the neutral axis of the SF12050 is very close to the center of the Hastelloy substrate. Per formula (3-1), the $y_{neutral}$ of SF12050 was 24-25 µm and the displacement between the neutral axis and geometric center was only 1-2 µm [96].

Since the REBCO layer deposited by MOCVD has a nearly single-crystalline structure, the irreversible compressive strain limit exceeded -2%. It was mentioned that for REBCO tape with a 50 µm thick substrate, a winding radius of 1.25 mm was possible [76] because of the high compressive strain limit. This value corresponds to the bending radius calculated by substituting an ε of -2% into formula (3-2).

An experiment was performed to test the bending performance of normal REBCO tape. A SF12050 tape was slit into 2 mm wide sections by laser slitting, which was discussed in Chapter 2.2. To protect the tape from damage during multiple bending tests, a 20 μm thick copper stabilizer was electroplated onto both sides of the tape. Since the neutral axis of the original tape was very close to the geometric center and the thickness of the copper layers was the same on both sides, the extra copper did not shift the neutral axis.

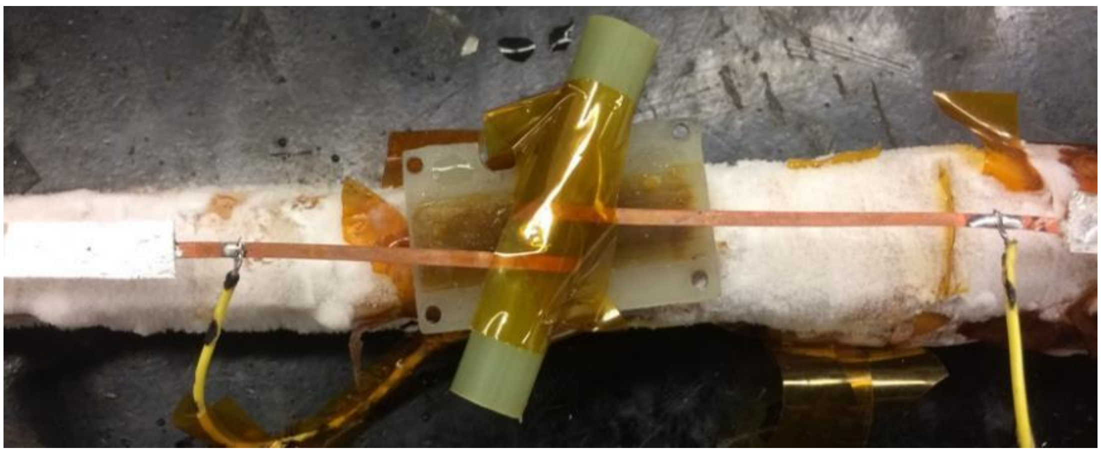

Fig. 3-2 REBCO tape bending test on a 9.5 mm diameter G10 rod

The tape was wound a single turn over a former with the REBCO side facing inward, as demonstrated in Fig. 3-2. The tape was fixed by Kapton tape and its two ends were firmly connected to current leads. This structure ensured that the bending diameter of the tape was kept unchanged during the test. The bending formers with diameters of 12.5 mm, 11.0 mm, 9.5 mm, 7.5 mm, or 6.5 mm were made of G10; the bending formers with diameters of 3.19 mm or 2.06 mm were made of brass. The 77 K, self-field critical currents were tested by a standard 4-point method and a criterion of 1 μV/cm was used. The sample was first tested in straight form, for which the measured I_c was 54 A; afterward, the sample was bent and tested on the largest former, i.e., a 12.5 mm diameter G10 rod. Without flattening the tape, the next-smallest former was used for the next test.

The dependence of the I_c on the bending diameter is plotted in Fig. 3-3 [97]. The results show that I_c started to decrease at much larger diameters than expected. At a 6.5 mm bending diameter, the tape maintained 93% of its original I_c in straight form; however, at a 3.19 mm bending diameter, the I_c retention rate was only 53% and only 10% of the I_c was retained at a 2.06 mm bending diameter. The reason for the much-earlier-than-expected I_c degradation in the bending test is because the plastic deformation of the tape happened at small bending diameters and the previous expectation only considered elastic deformation. In elastic deformation, the bending stress changed linearly with the distance from the neutral axis; in plastic deformation, however, the outside regions of the tape yielded first, redistributing the strain and causing the REBCO layer to experience a much larger bending strain.

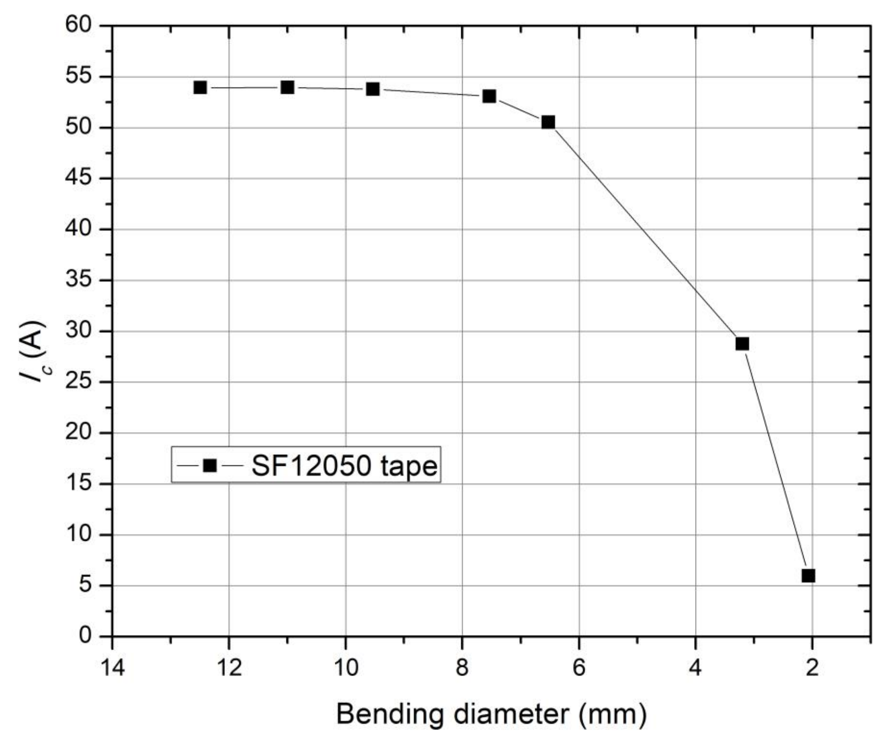

Fig. 3-3 I_c dependence of SF12050 tape on bending diameter

3.1.2 Bending tests of tapes with different configurations

3.1.2.1 Bending test under compressive strain

To enhance the bending performance of the REBCO tape, the key factor is to decrease the distance between the REBCO layer and the neutral axis; one method to decrease this distance is to use REBCO tape with a thinner substrate and another is to deposit or laminate materials, such as copper, on the REBCO side of the tape. Both methods shift the neutral axis of the tape closer to the REBCO layer, which makes the REBCO layer experience less strain during bending. The thin substrate REBCO tapes were produced using the grinding method, as discussed in Chapter 2.1. In this section, 5 thin substrate REBCO tapes with different configurations were directly compared in bending tests under compressive strain to verify these methods.

Fig. 3-4 Schematic structure of samples for bending test (not to scale)

Tab. 3-1 Thickness of copper layers and Hastelloy substrate

Layer thickness	S1	S2	S3	S4	S5	S6
T1 (µm)	20	10	20	30	20	5
T2 (µm)	50	22	22	22	22	22
T3 (µm)	20	1	1	1	20	30

The schematic layer structure of the tested samples is demonstrated in Fig. 3-4. Compared to the structure of SF12050 tape, the Hastelloy substrate with a thickness of 22 μm was much thinner. Because reel-to-reel silver sputtering was used to cover the exposed edges of laser-slit samples, the silver layer thicknesses (2 μm on the REBCO side and 1 μm on the substrate side) were also slightly different from the original tape. Copper layers of different thicknesses on the REBCO side (T1) and Hastelloy side (T3) were electroplated to study the influence of tape configurations on bending performance. The thicknesses of the copper layers and Hastelloy substrate of the samples are listed in Tab. 3-1. Sample S1, which is the original SF12050 tape discussed in the previous section, was included for comparison. To cover the edges and prevent delamination at small bending diameters, 1 μm of copper was electroplated onto the substrate side of the tape for S2, S3, and S4.

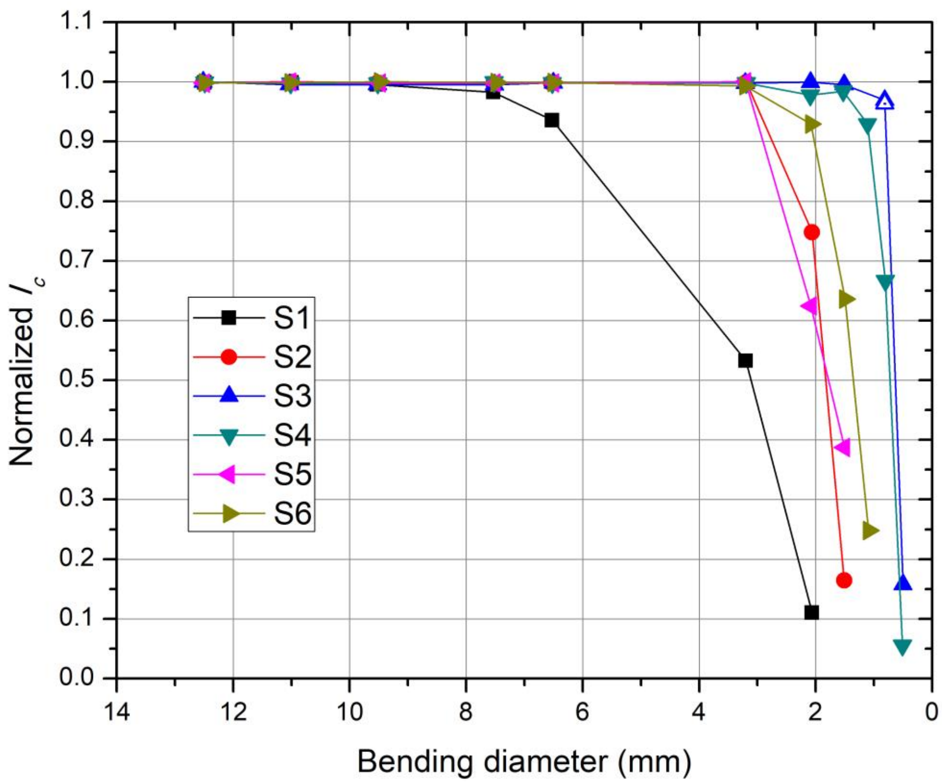

Fig. 3-5 I_c dependence of different tape configurations on bending diameter

All the samples were laser-slit to a width of 1.6 mm (to avoid overlapping on small formers) and bent on the formers with the REBCO side facing inward. In addition to the formers with diameters between 12.5 mm and 2.06 mm, brass rods of 1.5 mm and 1.1 mm in diameter, and copper rods of 0.8 mm and 0.51 mm in diameter were also included. The small-diameter metallic formers were used to mimic the condition of the STAR wires discussed in the next chapter. The tapes were first tested in straight form and their corresponding I_c values were between 41 A and 47 A. The small variation in I_c values was due to the tapes' different production batches and their location in the parent 12 mm wide tape. To emphasize the influence of bending diameter, the I_c values in bending form were normalized with each tapes' flat I_c value, as plotted in Fig. 3-5 [97].

The 22 μm substrate samples exhibited much better I_c retentions at small bending diameters. S3 and S4 showed no significant I_c degradation at bending diameters of 0.8 mm and 1.1 mm, respectively. After exceeding a bending diameter of 3.19 mm, plastic deformations were found in both S3 and S4 as their original flat shapes could not be regained. To confirm the I_c reversibility, the I_c of sample S3 was re-measured after releasing the strain and partially unwinding it from the 0.8 mm diameter bending former; the result is shown as the open triangle in Fig. 3-5. Since the I_c values before and after releasing the bending strain were the same, it is believed that the 3% of the degradation of S3 at 0.8mm was not reversible because of the plastic deformation. For S2, S5, and S6, drastic I_c degradations were observed at bending diameters of 2.06 mm, 2.06 mm, and 1.5 mm, respectively.

The bending test results indicate that the thickness of the copper layers plays an important role in enhancing the bending performance of thin REBCO tape. For certain thicknesses of substrate, there is an optimal copper thickness to get the best bending property and deviating from that thickness yields inferior performance. The tape with the optimal copper layer shifts the neutral axis close to the REBCO layer and nearly the same bending strain is expected at each side of the REBCO layer, which is why the tape is called 'symmetric tape.'

Fig. 3-6 shows a microscopic cross-section of symmetric tape [98]. Except for the 20 μm area near the edge, the thicknesses of the Hastelloy substrate and copper layers are very uniform. It is observed that the REBCO layer is close to the geometric center of the tape, which thus forms the symmetric structure.

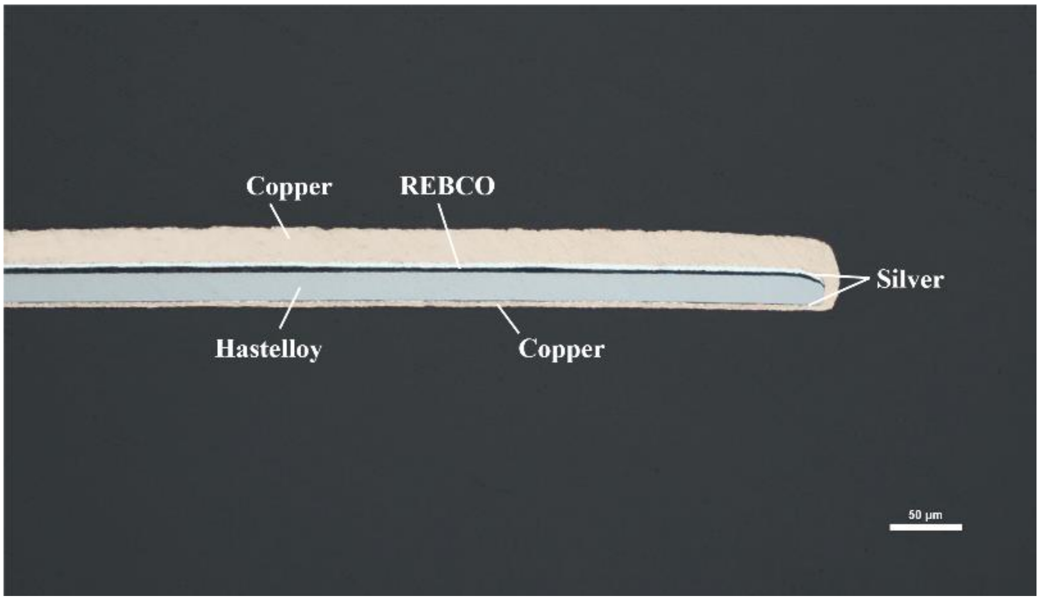

Fig. 3-6 Cross-section of a symmetric tape

3.1.2.2 Bending test under tensile strain

Because of the ceramic nature of the REBCO material, the REBCO layer can sustain much higher compressive strain than tensile strain, which is also why REBCO tapes are wound under compressive strain in most applications. For symmetric tapes, however, it is interesting to study the bending properties under tensile strain since the REBCO layer is close to the neutral axis.

Similar bending experiments under tensile strain were carried out. A 1.6 mm wide tape S7 was slit from the edge of a 12 mm ground tape such that the thickness of the Hastelloy was only 16 μm. A reel-to-reel electroplating machines was used to deposit 30 μm of copper, 28 μm on the REBCO side and 2 μm on the Hastelloy side. The tape was first tested in straight form and the flat tape I_c

was 38 A, which was slightly lower than average because of its edge location in the parent 12 mm wide tape. Afterwards, the tape S7 was wound a single turn on the formers with the REBCO side facing outward. The normalized I_c values of S7 at different bending diameters are plotted in Fig. 3-7, and the data of S3 is added for comparison.

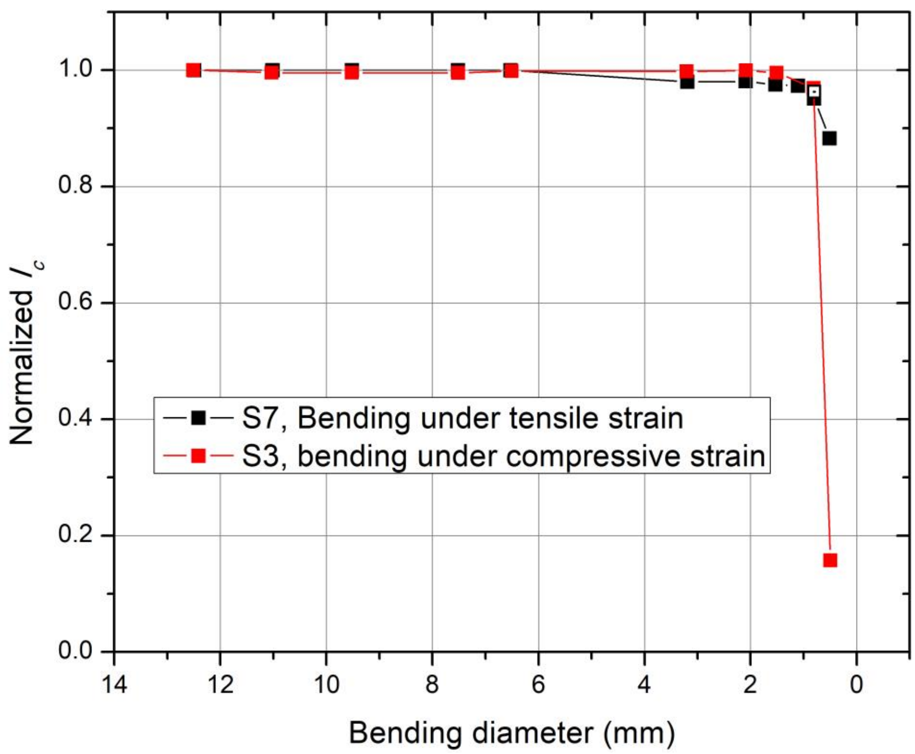

Fig. 3-7 Comparison of I_c dependence on bending diameter under tensile and compressive strain

As expected, this symmetric tape shows exceptional bending performance under tensile strain. At bending diameters equal or larger than 0.8 mm, the I_c degradation is less than 5%. Even at the smallest diameter of 0.51 mm, the tape still can maintain 88% of its initial I_c. The better result at the 0.51 mm bending radius is believed to be due to the ultra-thin substrate. The reversibility test after releasing the strain and partially regaining the shape at 0.8 mm shows a 0.5 A higher I_c than when the tape is under strain; this is marked as an open square in Fig. 3-7. However, after unwinding from the 0.51 mm former, the tape was damaged due to delamination. The similar results between the compressive and tensile strain bending experiments prove the symmetric structure of the tape and its extraordinary bending properties.

3.2 Symmetric tape parameter optimization

3.2.1 Optimization of copper stabilizer thickness

Tab. 3-2 Electroplating parameters of tapes used for copper thickness optimization

Sample	Initial tape thickness (μm)	Copper thickness (μm)		Electroplating current (A)	Tape thickness after electroplating (μm)
		Theoretical value (μm)	Measured value (μm)		
S1-1	21	22	23	0.71	44
S1-2		24	24	0.78	45
S1-3		26	26	0.84	47
S2-1	24	27	27	0.87	51
S2-2		28	28	0.91	52
S2-3		29	29	0.94	53
S2-4		30	31	0.97	55
S3-1	25	29	29	0.94	54
S3-2		31	31	1.00	56
S3-3		33	33	1.07	58
S4-1	27	24	25	0.78	52
S4-2		28	28	0.91	55
S4-3		32	33	1.04	60
S4-4		36	36	1.16	63
S4-5		40	41	1.29	68
S4-6		44	45	1.42	72

Because the REBCO tape has a multi-layer structure and the plastic deformation happens at small bending diameters, predicting the optimal copper thickness for bending property enhancement is quite difficult. Material strain hardening and delamination between layers also need to be considered to make precise predictions. Therefore, the experimental method was used to directly determine the optimal copper thickness for compressive bending. Tapes were electroplated with different thicknesses of copper and wound into STAR wires to check the level of I_c degradation.

Considering the thickness variation along the width of the ground thin tape, four thicknesses of thin tape (21 μm, 24 μm, 25 μm, and 27 μm) were selected as optimization targets. These 2 mm wide, laser-slit tapes had the same REBCO layer, buffer stack, and silver layers, whose thicknesses are marked in Fig. 3-4. Therefore, the tape's total thickness variation was caused solely by differences in the thickness of the Hastelloy. The copper layer was deposited with the reel-to-reel electroplating system using a 4 cm/min tape movement speed. For a 30.9 μm/A copper deposition rate on 2 mm tape, the electroplating currents and corresponding theoretical copper thicknesses are listed in Tab. 3-2.

In order to get a full optimization curve at each tape thickness, three to six samples cut from the same piece of tape were electroplated with different thicknesses of copper. The tape thickness was measured before and after electroplating by a micrometer to calculate the copper thickness, which was within ± 1 μm of the theoretical value. It is noteworthy that because of the tape movement during reel-to-reel electroplating, 1-2 μm of the copper was deposited onto the backside of the tape.

Fig. 3-8 Photograph of a single-layer STAR wire for copper optimization

For each sample listed in Tab. 3-2, two 15 cm long single-layer STAR wires, as demonstrated in Fig. 3-8, were made by the winding machine separately to reduce accidental errors. Tapes were wound on a 20 AWG copper former with REBCO layer facing inward, and the winding angle was kept at 45 degrees. The I_c values of the flat tape and STAR wires were measured with a 1 μV/cm criterion. I_c values of STAR wire made of tapes with an initial thickness of 24 μm are plotted in Fig. 3-9. As can be seen, with the help of the symmetric structure, at a bending diameter of 0.8 mm, the I_c retention of all the wires was between 70% and 94%. For the wires made of tape with the same copper thickness, the I_c varied up to 5 A; however, the relationship between the copper thickness and I_c can be clearly seen. Tapes with 29 μm thick copper layers maintained an average I_c retention of 91%, which was the highest observed value. As the copper thickness deviated from the optimal 29 μm, the I_c retention also dropped.

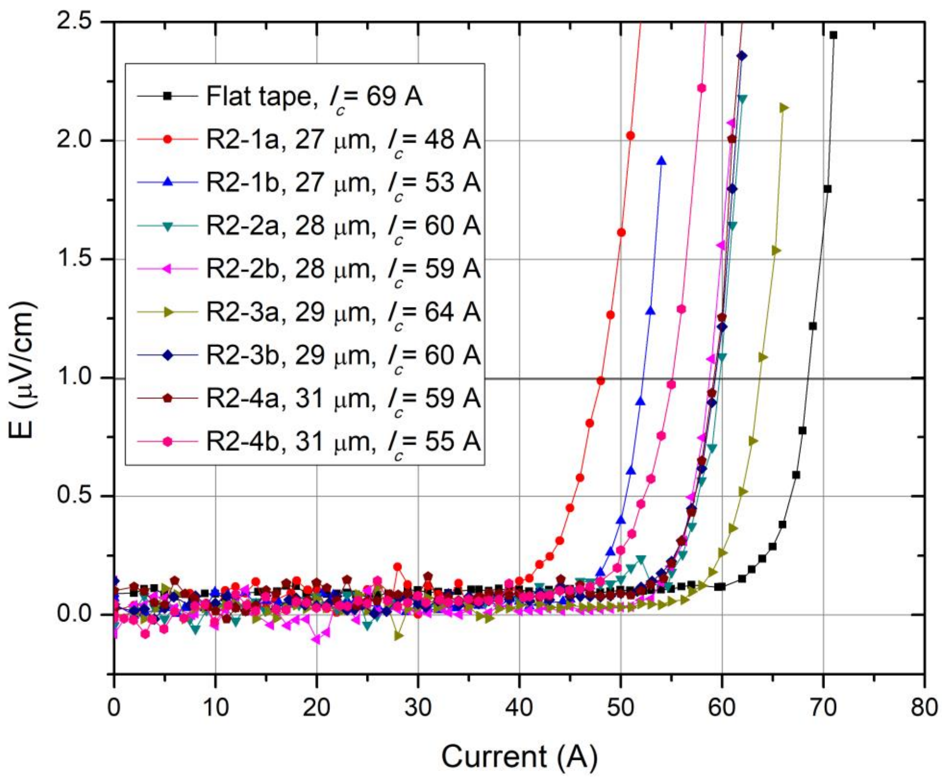

Fig. 3-9 *I-V* curves at 77K, self-field of STAR wires made of tapes with initial thickness of 24 μm

The same bending tests were performed on tapes with initial thicknesses of 21 μm, 25 μm, and 27 μm; all the I_c retention results for these tapes are plotted in Fig. 3-10. Since two STAR wires were made from each sample, the error bars are used to represent their test results and the average values are marked with solid dots. For the 21μm, 24 μm and 25 μm thick tapes, a small range of copper thickness was applied; whereas for the 27 μm thick tape, a larger range of copper thickness of 20 μm was applied to study the I_c retention change. It is clear that at each tape thickness, there is an optimal copper thickness at which the I_c retention is the highest. At such small bending radii, the I_c retention is very sensitive to copper thickness. Deviating from the optimal value by 4 μm, e.g., as that observed with R4 at 33 μm rather than the optimal 37 μm, reduced the I_c retention from 74% to 25%. The optimal copper thickness decreases as the initial tape thickness decreases since less copper is needed to shift the neutral axis for thinner tapes.

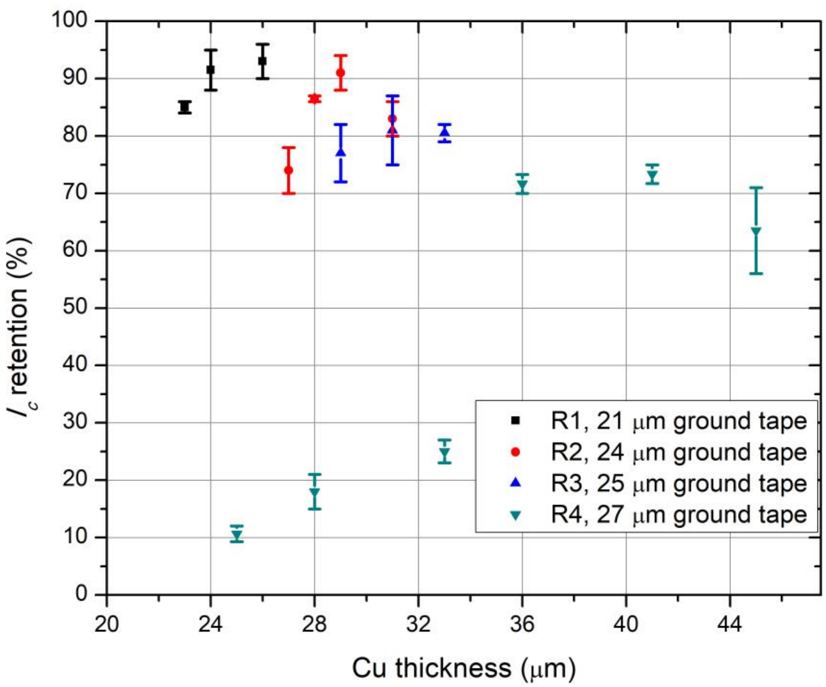

Fig. 3-10 I_c retention versus copper thickness of tapes with different initial thicknesses

Interestingly, the maximum I_c retention at the optimal copper thickness also decreases as the tape thickness increases. One possible explanation is the movement of the neutral axis during bending. At large bending radii, both the copper and the Hastelloy are under elastic deformation, and the initial position of the neutral axis is in the copper where near the REBCO layer. As the bending radius decreases, the copper is under plastic deformation due to its smaller yield strength whereas the Hastelloy is still under elastic deformation; therefore, the neutral axis moves towards the center of the Hastelloy and "sweeps" over the REBCO layer. At even smaller bending radii, both the copper and the Hastelloy are under plastic deformation, and the neutral axis moves back towards the REBCO layer. For thicker tapes, because of the larger thickness of the Hastelloy, the sweeping distance of the neutral axis is larger than the thinner tape and the final distance between the neutral axis and the REBCO is farther, which could be why the maximum I_c retention decreased.

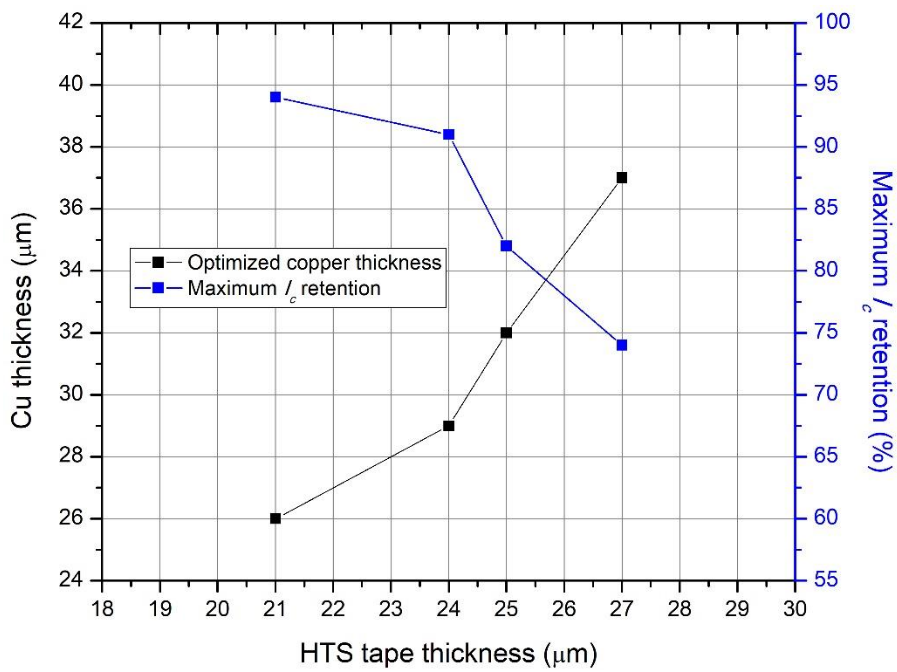

Fig. 3-11 Optimized copper thickness and corresponding maximum I_c retention

The optimized copper thickness and corresponding maximum I_c retention versus tape thickness are summarized and plotted in Fig. 3-11. This important optimization curve is used to predict the performance of STAR wires that contain multiple layers of tape with different thicknesses. For both curves, the slopes change at a tape thickness of 24 μm. Thicker copper layers are needed and less I_c retention is observed when the initial tape thickness exceeds 24 μm. Also, thicker copper and thicker initial tape thicknesses decrease the J_e of the tape. Compare 21 μm and 27 μm thick tapes with optimal copper layers: the J_e of the 21 μm tape itself is 42% higher, or 37% higher if including the 20 AWG former, than that of the 27 μm tape.

3.2.2 Optimization of twist pitch

Twist pitch is another important parameter for winding the symmetric tapes into STAR wires. At different twist pitches, the bending strain in the tape changes accordingly since twist deformation can be decomposed into pure bending deformation and twist bending deformation. Along the tape length, if only elastic deformation is involved, the strain in the REBCO layer $\varepsilon(p)$ is proportional to the difference between the length of the twist path of the REBCO layer l_{REBCO} and the length of the twist path of the neutral axis $l_{neutral}$ [76], expressed as

$$\varepsilon(p) = \frac{(l_{REBCO} - l_{neutral})}{l_{neutral}} = \frac{\sqrt{\frac{1}{4}p^2 + 4\pi^2(r+y_1)^2}}{\sqrt{\frac{1}{4}p^2 + 4\pi^2(r+y_2)^2}} - 1, \tag{3-3}$$

where p is the twist pitch, r is the former radius, y_1 is the distance between the former surface and the REBCO layer, and y_2 is the distance between the former surface and the neutral axis. For symmetric tape, as long as y_1 and y_2 are not completely consistent, the bending strain should decrease as twist pitch increases. Therefore, the I_c of STAR wire is expected to increase at larger twist pitches.

Thirty-six short STAR wires were made to study the influence of twist pitch on I_c retention. Two-mm wide, 10 cm long REBCO tapes were wound on 0.8 mm and 1.1 mm brass formers at different twist pitches, as shown in Fig. 3-12. The substrate of the tape was 20 μm and a 20 μm thick copper layer was deposited on the REBCO side. The tapes were wound three turns with the REBCO side facing inward on the former and fixed by Loctite 404 and fast-curing epoxy. Since the tapes were too short for the automatic winding machine, manual winding was used to fabricate all the STAR wire samples. At a 1.1 mm bending diameter, samples with twist pitches of 2 mm, 4 mm, 6 mm, 8 mm, and 10 mm were tested; at a 0.8 mm bending diameter, since the 2 mm twist pitch is not viable due to overlapping, 3 mm, 4 mm, 6 mm, and 8 mm twist pitches were studied. The retention rates between the flat tape I_c and STAR wire I_c values of the 36 samples are plotted in Fig. 3-13, where the I_c retention rates are grouped by twist pitch and their average values are marked by solid lines.

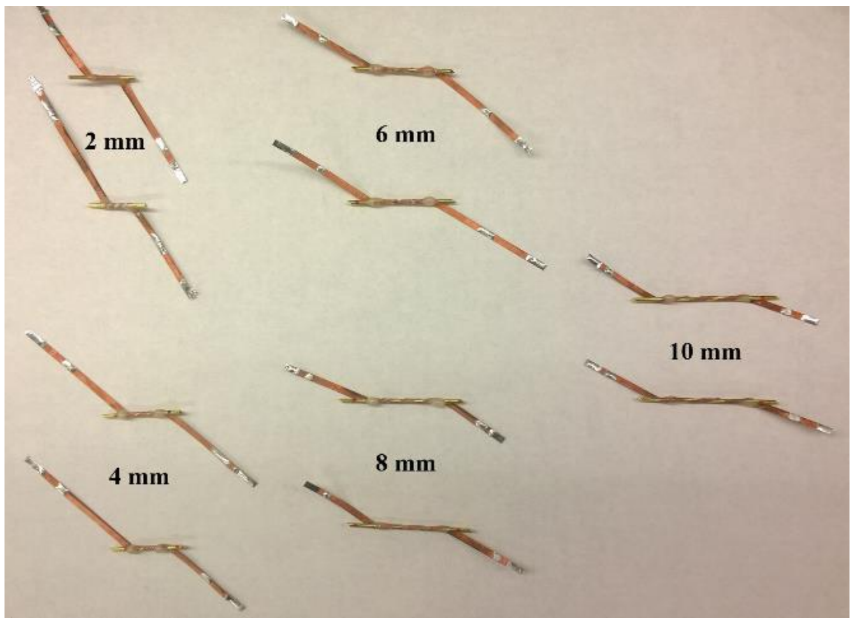

Fig. 3-12 Short STAR wires with different twist pitches

It is observed that most of the I_c retention rates under the same twist pitch are within a 15% range, whereas a few dots are scattered further, which is probably caused by handling issues during manual winding. The average values, however, display a clearer trend. Contrary to expectations, the I_c retentions on both the 0.8 mm and 1.1 mm formers decrease at larger twist pitches. On the 0.8 mm former, the highest average I_c retention (74%) is achieved at the smallest twist pitch of 3 mm, whereas the averaged I_c retention gradually decreased to 54% at a twist pitch of 10 mm. On the 1.1 mm former, the average I_c retention increased slightly from 86% at 2 mm to 87% at 4 mm, then gradually decreased to 70% at the 10 mm twist pitch. This trend indicates that the assumption that the I_c value of the twist tapes in STAR wire is determined only by the bending strain along the tape length may not be correct.

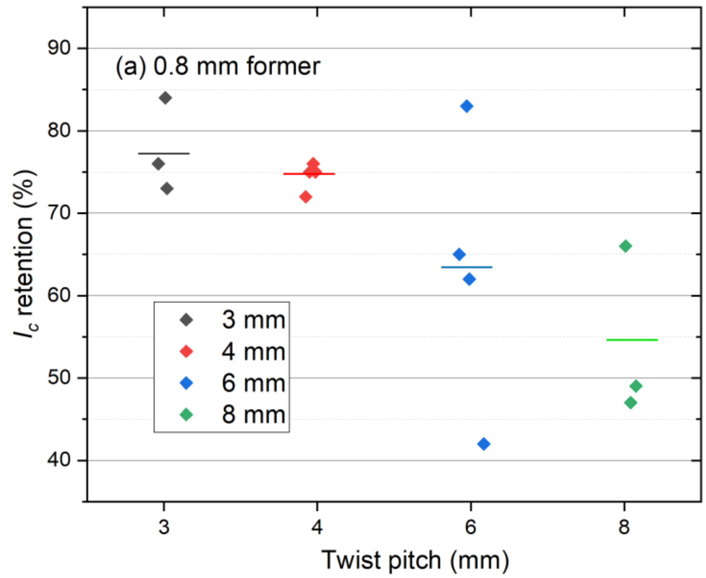

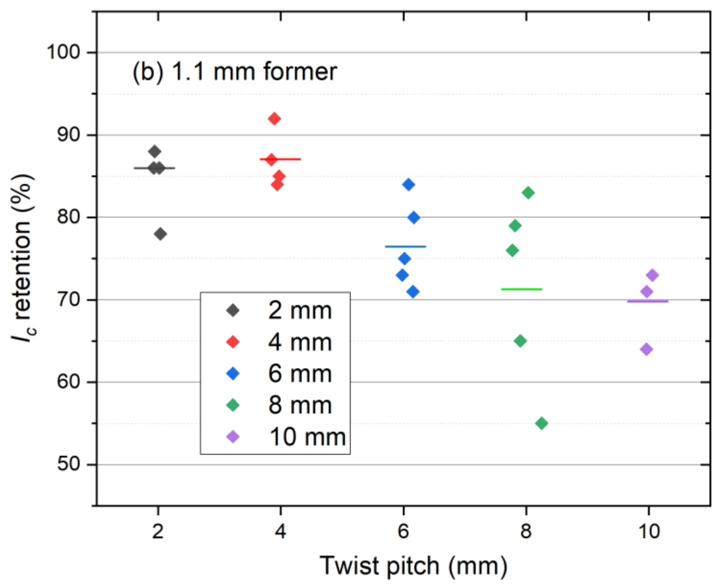

(a) STAR wires on 0.8 mm former; (b) STAR wires on 1.1 mm former

Fig. 3-13 I_c retention dependence on twist pitch

A possible explanation for the observed I_c changes is the different strain sensitivities of I_c due to the microstructure of the REBCO layer [79]. Twin planes in the REBCO layer, which switch locally between the [100] and [010] directions, are usually oriented 45° to the a-axis and b-axis. Since the strain applied in the REBCO layer causes local changes in T_c and I_c on both sides of the twin boundary, the angle between the strain direction and the a-axis of the tape affects the strain sensitivity of I_c. The tape is most sensitive to strain when the strain is along the [100] and [010] directions, whereas the tape is least sensitive to strain when the strain is along the [110] direction.

In the single-layer STAR wires, the twist pitch p is calculated as

$$p = \pi d \cdot \tan\theta, \tag{3-4}$$

where d is the diameter of the former and θ is the wrap angle. Therefore, for 0.8 mm and 1.1 mm diameter formers, at a 45° wrap angle, the optimal twist pitches are 2.5 mm and 3.5 mm, respectively. This result corresponds well with the trend of I_c retention in Fig. 3-13. The I_c retention rates at twist pitches next to the optimal values are the highest; therefore, in long-length STAR wire fabrication, the wrap angle is set at 45°.

Chapter 4. STAR wire electrical performance and analysis

This chapter discusses the electrical performance of STAR wires with different structures. The chapter begins with 77 K self-field tests of STAR wires in both the straight and bent forms, followed by in-field test results of STAR wires, including analyses of the field dependence and angular dependence. The terminal resistance, interlayer resistance, and several methods of detecting defects in STAR wires are discussed at the end.

4.1 77 K self-field performance of STAR wires

Based on the parametric analysis of symmetric tapes in the previous chapter, the optimal copper thickness was applied to produce symmetric tapes with excellent bending properties. At the optimized winding angle, these tapes were used to produce STAR wires with different structures. Several STAR wire structures, including a manually-wound fixed-tape-width structure, a variable-tape-width structure, a multiple-tapes-in-a-single-layer (MTISL) structure, and an optimal-tape-width structure, were tested and analyzed. Except for the manually-wound fixed-tape-width STAR wire, all the STAR wires were fabricated by the automatic winding machine. Their I_c values and corresponding J_e values, in both the straight and bent forms, were tested at 77 K in self-field. Unless otherwise stated, the voltage criteria were set at 1 μV/cm. After comparing the performances of the different structures, a 10 m long STAR wire with the optimal-tape-width structure was produced and tested. The STAR wires' electrical performance improvements are summarized at the end.

4.1.1 Manually-wound fixed-tape-width structure

4.1.1.1 Layer-wise performance in straight form

A manually-wound, 7.5 cm long, six-layer STAR wire with conical terminals, as shown in Fig. 4-1 [89], was fabricated and tested. Six layers of 2 mm wide symmetric tapes were wound on a 0.8 mm copper core in the clockwise direction and soldered onto copper terminals; the outer diameter was 1.6 mm. The tapes' I_c values were measured in a straight form and listed in Tab. 4-1. For the STAR wire, two voltage taps were located at the cylindrical parts of the terminals, which were outside the current leads; therefore, the resistance of the copper terminals themselves and the contact resistance between the terminal and tape were measured as well. Since manual winding provided more flexibility during the test, the voltage versus current curves of the STAR wire were measured after winding each layer and are plotted in Fig. 4-2 [89]. The calculated I_c values of each curve are marked in the plot.

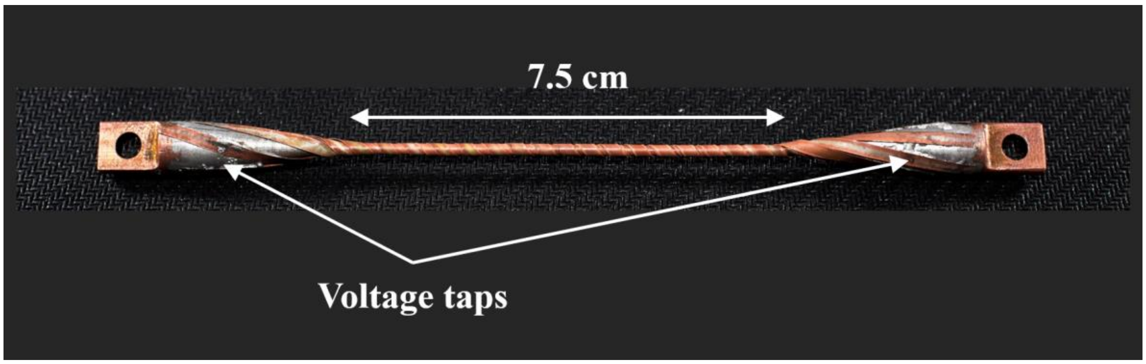

Fig. 4-1 A manually-wound STAR wire with conical terminals

Tab. 4-1 Layer-wise electrical performance of manually-wound STAR wire

Layer	1	2	3	4	5	6	Total
Flat tape I_c (A)	68	66	75	72	67	75	423
Total resistance (μΩ)	2.92	3.20	3.16	2.73	1.83	1.47	1.47
Round wire I_c increment (A)	58	27	45	48	45	60	283
I_c Retention (%)	85.3	40.9	60.0	66.7	67.2	80.0	66.7

As can be seen from the curves, due to the small size of the contact area between the superconducting tapes and the copper terminals, the contact resistance is relatively high. In order to get accurate I_c values, a non-linear fitting method, which will be discussed later in this section, was used. The calculated total resistance and I_c retention are also listed in Tab. 4-1. The round wire

I_c increment in the table refers to the calculated I_c of each layer after winding, which assumes that the outer layers do not affect the performance of the inner layers.

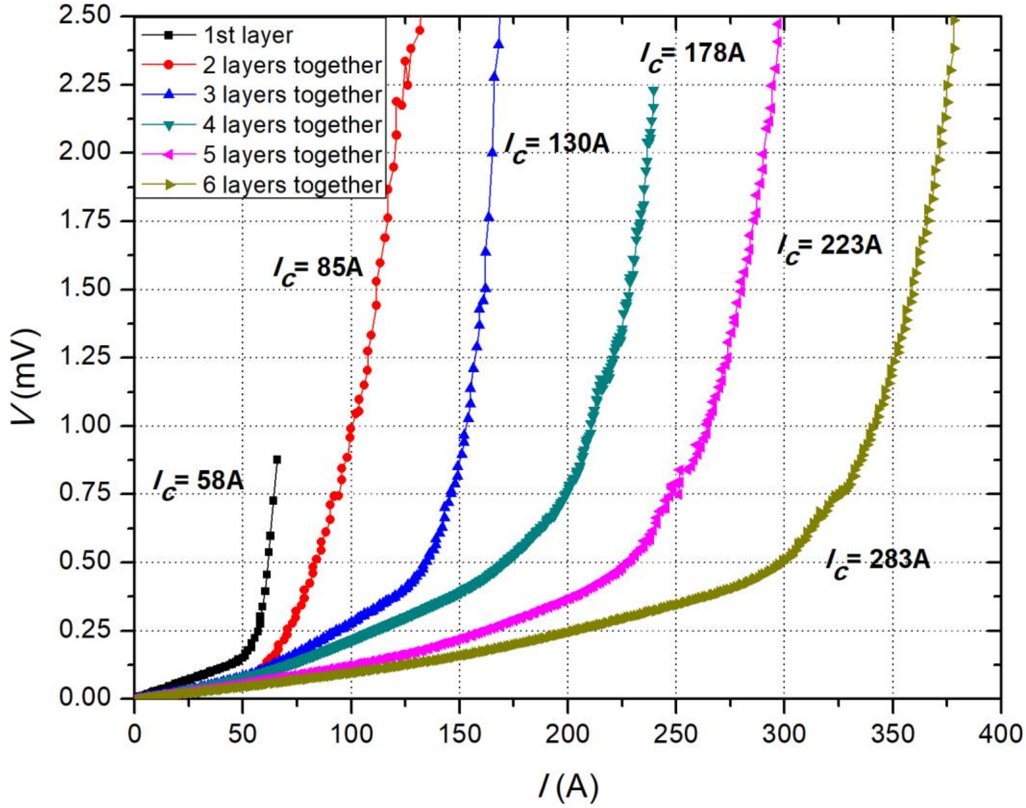

Fig. 4-2 *I-V* curves of manually-wound wire at 77 K in self-field

As the number of layers increases, the total contact area at the current leads increases and the total resistance decreases gradually, as expected. The exception happens at the first layer, which has a lower resistance than that of three layers together. Since soldering each layer requires heating up the whole copper terminal, the abnormal change of resistance may be caused by the tape re-soldering process during the terminal heating process. The I_c retention also increases as more layers are wound due to the larger diameter and because less strain is applied on the outer layer; however, the first layer shows the highest I_c retention (85.3%) at the 0.8 mm diameter. One possible reason is that the first layer was directly wound on the copper former, which has a smoother surface than the other layers. Therefore, less local stress is concentrated on the first layer, which leads to the highest I_c retention. Near the transition point, there are kinks in the curves of the 4th, 5th, and 6th layers, which indicate current sharing between layers. With an outer diameter of 1.6 mm, the J_e of this manually-wound STAR wire is 141 A/mm^2.

4.1.1.2 Bending performance

After being tested in the straight form, with the help of plastic tubes with different outer diameters, the manually-wound STAR wire was bent from 12 cm to 3 cm in diameter and the I_c values were measured in the bent form. Fig. 4-3 shows the STAR wire at a 5 cm bending diameter. The *E*-*I* characteristics at different bending diameters are plotted in Fig. 4-4 [97].

Fig. 4-3 The manually-wound STAR wire at a 5 cm bending diameter

The same nonlinear fitting was used to determine the I_c values. It is expressed as

$$U = U_c\left(\frac{I}{I_c}\right)^n + IR + C, \qquad (4\text{-}1)$$

where R is the contact resistance, U_c is the voltage criterion, n is the n-value, and C is the initial voltage offset. With the nonlinear fitting, the influence of the contact resistance and the initial voltage are removed, and the zoomed-in *E*-*I* characteristics in a log-log scale are plotted in Fig. 4-5 [97], where the calculated I_c values of each curve are in red squares. As can be seen, at bending

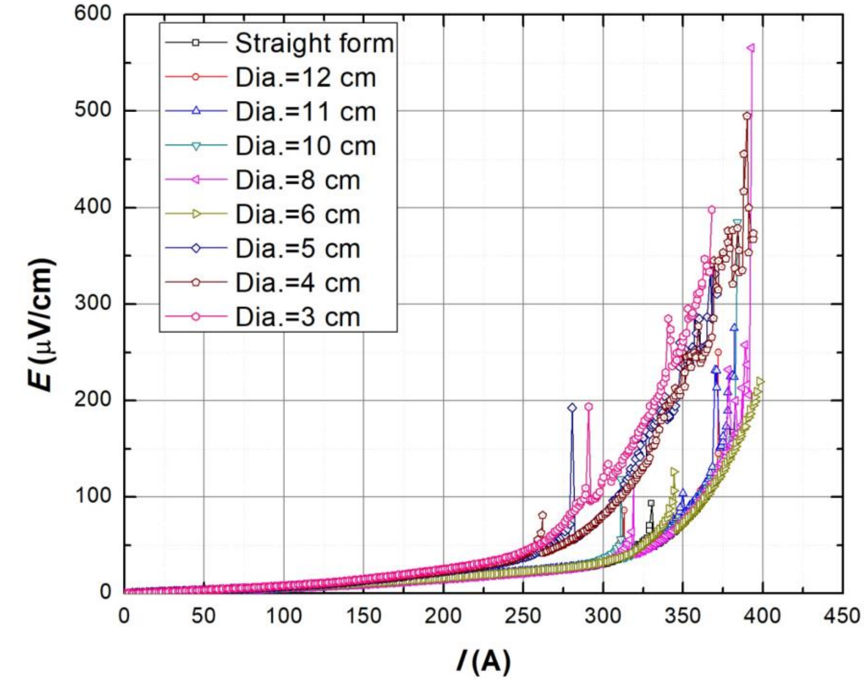

Fig. 4-4 *E-I* characteristics of manually-wound STAR wire at different bending diameters

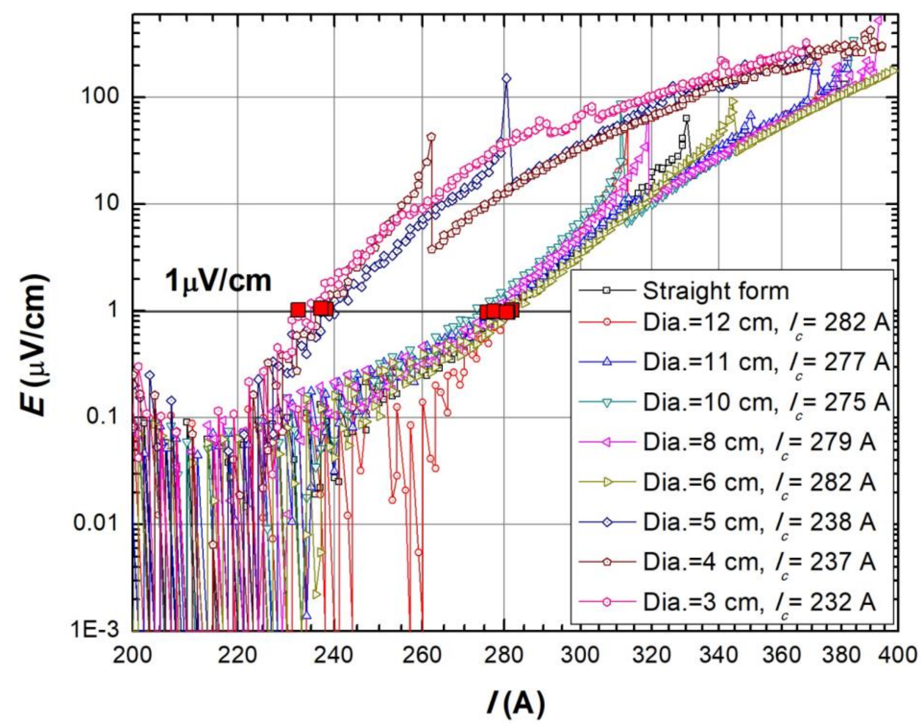

Fig. 4-5 Zoomed-in *E-I* characteristics of the manually-wound STAR wire in log-log scale

diameters of at least 6 cm, there is no signification degradation and the I_c values remain approximately the same as in the straight form. When the bending diameter decreases to 5 cm, the I_c value drops about 16%. At the smallest bending diameter of 3 cm, a maximum I_c degradation of 18% is observed, and the corresponding J_e is 115 A/mm^2. It is interesting to note that at different bending diameters, the locations of the kinks in each curve, which indicate the current sharing between layers, are also different due to slight changes in the interlayer resistance caused by layer deformation at each bending diameter.

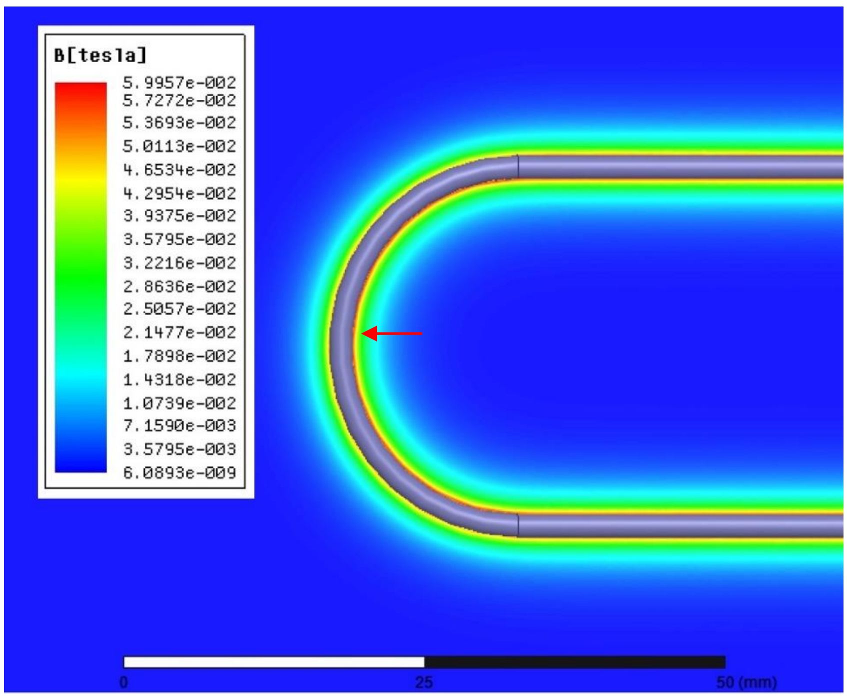

Fig. 4-6 Finite elemental model of a bent STAR wire and its magnetic field distribution

Comparing samples in the straight and bent forms, the self-field of the latter is increased because of the magnetic field concentration inside the bending circle. A finite elemental simulation was carried out to study the influence of the increased self-field. A simple 3D model of a half-circle STAR wire was built in the Ansoft magnetostatic module, as shown in Fig. 4-6. The outer diameter of the STAR wire was 2 mm and the bending diameter was 3 cm. As can be seen from the magnetic field distribution map, the point with the strongest magnetic field is located at the center of the wire's surface in the inner half circle, as marked by an arrow in the figure. With a 232 A current, which was the I_c of the manually-wound STAR wire at the 3 cm bending diameter, the magnetic field at that point is 60 mT; for a sample with the same current in a straight form, by applying Ampere's law, the magnetic field at the same point is 56 mT. The 4 mT increment of the magnetic field is negligible, and therefore the degradation of the I_c value of STAR wire in the bent form is caused only by the bending strain.

At bending diameters as small as 3 cm, the STAR wire maintains a high I_c retention, which proves its excellent flexibility. The symmetric structure of the REBCO tapes in the wire enable the wire to sustain extra bending strain during the bending process. In addition, as the number of layers increases, winding fixed-width tapes results in a gradually increased gap between each turn, which allows the tapes to slide during bending and prevents excessive bending strain accumulation.

4.1.2 Variable-tape-width structure

4.1.2.1 Tape width configurations

To increase the filling factor of STAR wire and correspondingly increase the I_c and J_e values, a variable-tape-width structure is proposed. In this structure, the tape width is not constant but increases as the wire diameter increases. Wider tapes are used in the outer layers and thus provide higher currents for the same outer diameter. The maximum tape width of each layer is determined by the wrap angle and wire outer diameter, as shown in Fig. 4-7, where d is the diameter of the wire, p is the twist pitch, ϑ is the wrap angle, and w is the maximum tape width. According to the geometric relationship, the maximum tape width is calculated as

$$w = \cos(\vartheta) \cdot p = \sin(\vartheta) \cdot \pi d. \tag{4-2}$$

With a wrap angle of 45 degrees, a series of typical wire outer diameter values and the corresponding maximum tape widths are listed in Tab. 4-2.

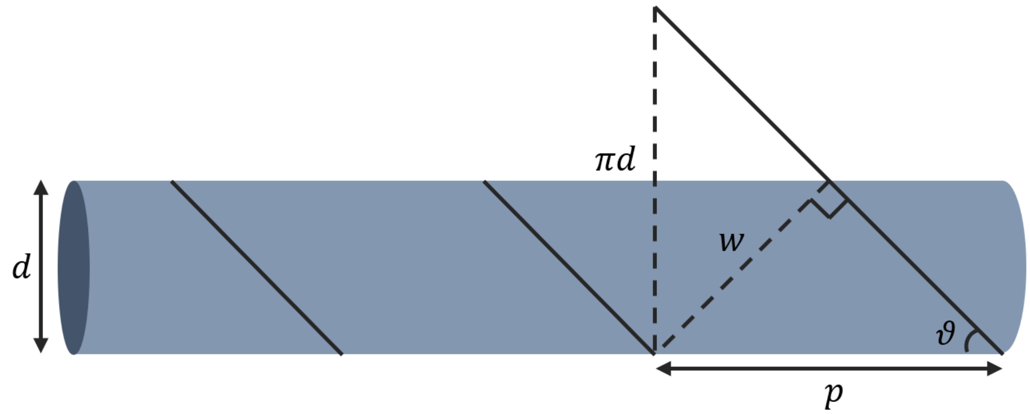

Fig. 4-7 Relationship between the twist pitch, wire diameter, and tape width

Tab. 4-2 Maximum tape width and two tape width configurations calculated by typical wire diameters

Layer number		1	2	3	4	5	6	Total
Typical O.D. (mm)		0.9	1.07	1.23	1.38	1.55	1.69	N/A
Maximum tape width (mm)		2.01	2.38	2.73	3.06	3.44	3.76	17.38
Variable tape width (mm)	Configuration-1	2	2.2	2.5	2.8	3.2	3.5	16.2
	Configuration-2	2	2	2.5	2.5	3	3	15

Two tape width configurations were studied and the width of each layer was as listed in Tab. 4-2. The minimum tape width was 2 mm as tapes narrower than that are very fragile and difficult to fabricate without any damage. Configuration-1 has as wide tapes as possible; each tape is only around 0.2 mm narrower than the maximum width except for the first layer. Configuration-1 focuses on increasing the I_c and J_e values in the straight form and the total tape width is 16.2 mm. After considering the tape fabrication difficulties, which are mainly caused by the irreplaceability of each tape due to the different widths, and the fact that one separate electroplating shield is needed for one tape width, configuration-2 was proposed. Only three tape widths, 2 mm, 2.5 mm, and 3 mm, were used and the total tape width was 15 mm. With this configuration, some gaps still exist between the tapes and the tapes are easier to fabricate.

4.1.2.2 Performance in straight and bent forms

For configuration-1, the I_c values of the REBCO tapes before winding were between 87 A and 142 A because of their different widths, whereas the currents per unit width were between 41 A/mm and 43 A/mm. The summation of flat tape I_c was 685 A. One piece of 1.1 m long STAR wire was fabricated and its outer diameter was 1.6 mm. The STAR wire was tested first in the straight form and then in the bent form at bending diameters that ranged from 8.5 cm to 3 cm. After bending, the wire was tested again in the straight form to check the I_c reversibility. The *E-I* characteristics are plotted in Fig. 4-8.

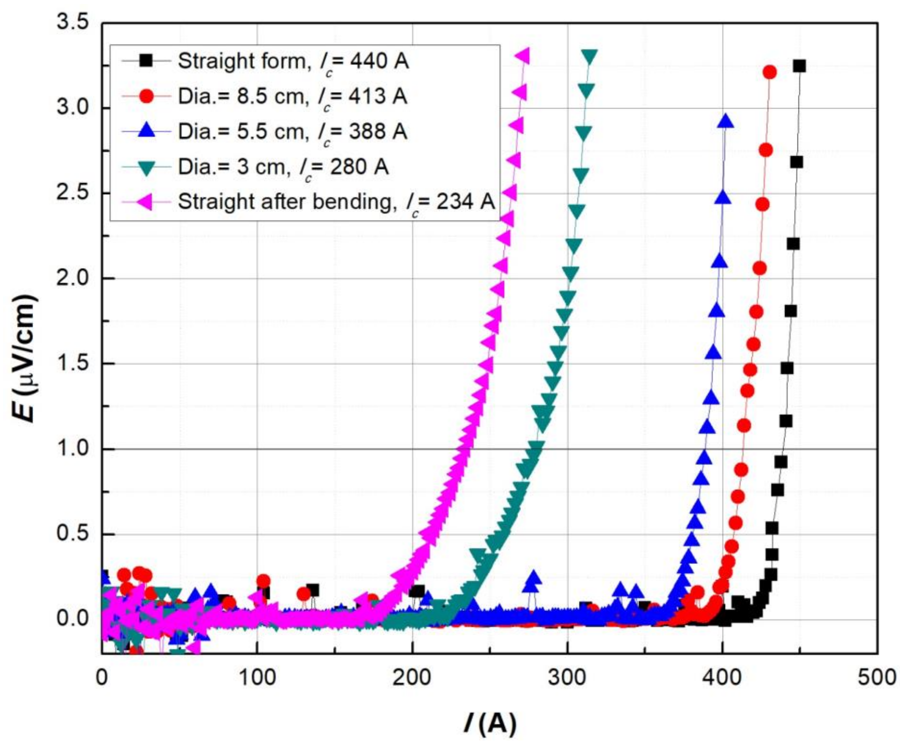

Fig. 4-8 *E-I* characteristics of variable-tape-width STAR wire of configuration-1

As can be seen, with a high current per unit width and an increased total tape width, the I_c of the STAR wire in the straight form is 440 A and the corresponding J_e is 219 A/mm^2, which is 55% higher than the manually-wound STAR wire. The retention of the flat tape's I_c summation in the wire I_c in straight form is 64%, which is comparable to that of manually-wound STAR wire. The bending performance, however, starts to degrade at bending diameters as large as 8.5 cm. At the 3 cm diameter, the wire I_c retention is only 63% compared to that in the straight form; the I_c and J_e also drop to 280 A and 139 A/mm^2, respectively. When the wire is straightened after bending, the I_c value drops again to 234 A, likely because the mechanical damage, such as cracks in the REBCO layer and delamination between the REBCO and copper layers, is expanded during the bending tension release process.

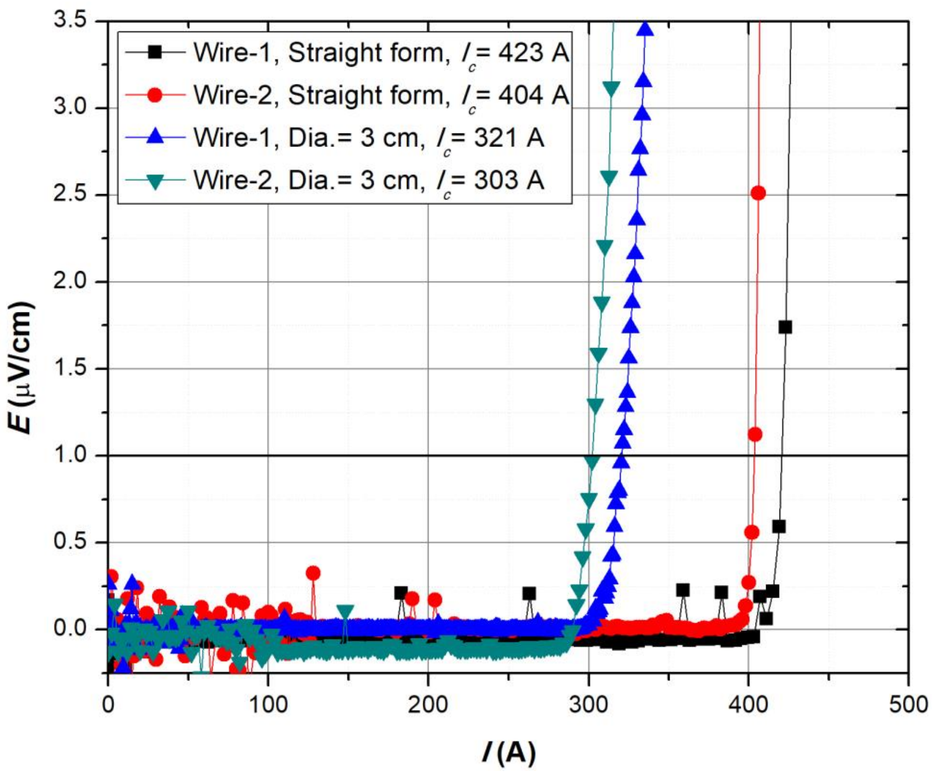

Fig. 4-9 *E-I* characteristics of variable-tape-width STAR wire of configuration-2

For configuration-2, with a total tape width of 15 mm and an average current per unit width of 43 A/mm, the summation of flat tape I_c was 651 A. Two shorter STAR wires (20 cm in length) were fabricated and their outer diameters were 1.72 mm for Wire-1 and 1.70 mm for Wire-2. The slightly larger diameters were due to the thicker REBCO tapes used for winding. The wires were directly bent to a 3 cm bending diameter after the test in the straight form and the *E-I* characteristics of the two STAR wires are plotted in Fig. 4-9.

In the straight form, the I_c values of the two wires are 423 A and 404 A, respectively, which correspond to 65% and 62% retention of the tape I_c summation in the straight wire I_c. At a 3 cm bending diameter, the I_c values of the two wires drop to 321 A and 303 A and the I_c retention values, compared to the straight form, are 76% and 75%, respectively. The straight-to-bent form I_c retention of configuration-2 is about 12% higher than that of configuration-1, but it is still not comparable to the fixed-tape-width structure in the manually-wound wire. Despite its 1.2 mm narrower total tape width and 0.1 mm larger outer diameter, configuration-2 still exhibits the same J_e of 138 A/mm^2 in the bent form as configuration-1 due to the better bending performance.

4.1.2.3 Analysis of longitudinal and circumferential stresses in bending

To explain the inferior bending performance of the variable-tape-width structures, an analysis of the bending stresses in the longitudinal and circumferential directions was performed. In tube bending theory [99, 100], the longitudinal and circumferential stresses are related by the geometric deformation relationship. In Fig. 4-10, a tube is bent and an element on the wall of the tube is studied. The bending force applied on the element can be decomposed into three components: the longitudinal component, $\mathrm{d}p_x$, the circumferential component, $\mathrm{d}p_c$, and the radial component, $\mathrm{d}p_r$. For STAR wire, since the wall thickness T equals the thickness of one REBCO layer and is much smaller than the wire diameter r, the radial component $\mathrm{d}p_r$ is negligible. The longitudinal component $\mathrm{d}p_x$ is expressed as

$$\mathrm{d}p_x = \sigma_x r \mathrm{d}\alpha T, \tag{4-3}$$

where σ_x is the longitudinal stress and $\mathrm{d}\alpha$ is the circumferential angle of the element. Its centripetal composite $\mathrm{d}f$ is

$$\mathrm{d}f = 2\mathrm{d}p_x \sin\frac{\theta}{2}, \tag{4-4}$$

where θ is the bending angle of the element. For small angles, $\sin\frac{\theta}{2} \approx \frac{\theta}{2}$, and Eq. (4-4) is simplified as

$$\mathrm{d}f = \mathrm{d}p_x\theta. \tag{4-5}$$

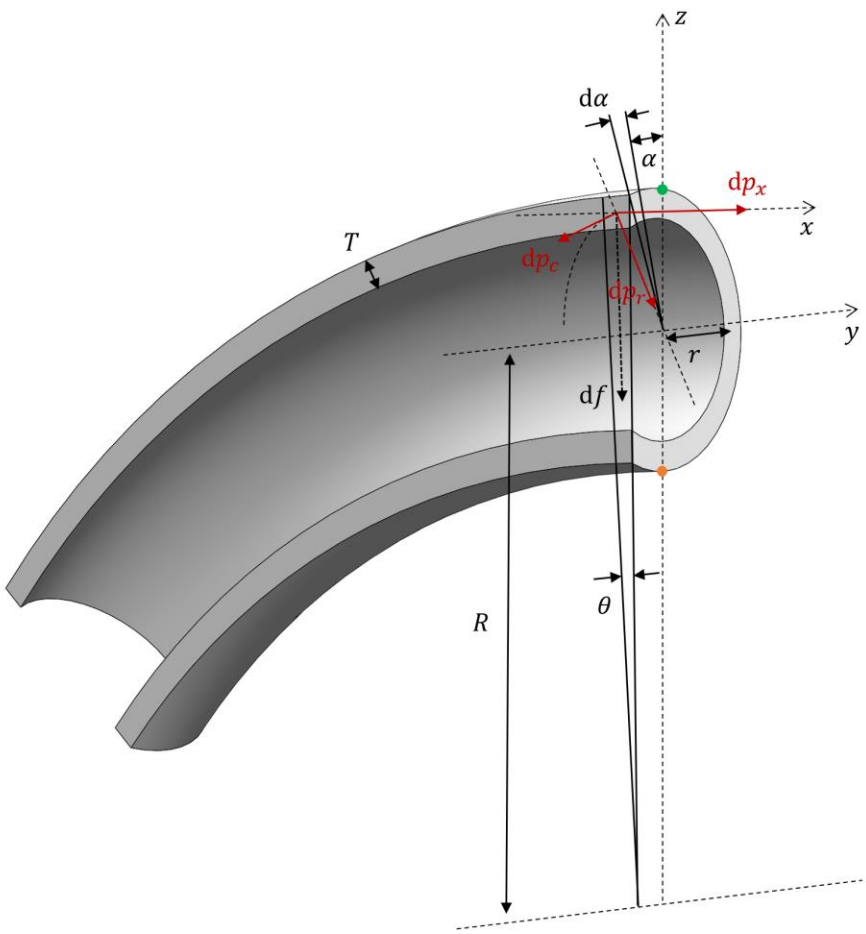

Fig. 4-10 Stresses induced during tube bending

For the circumferential component $\mathrm{d}p_c$, which is produced by $\mathrm{d}f$, it can be expressed as

$$\mathrm{d}p_c = \mathrm{d}f \sin\alpha. \tag{4-6}$$

where α is the circumferential angle of the element. Substituting Eq. (4-3) and Eq. (4-5) into Eq. (4-6) results in

$$\mathrm{d}p_c = \sigma_x r \mathrm{d}\alpha T\theta \sin\alpha. \tag{4-7}$$

Also, in terms of the circumferential stress, $\mathrm{d}p_c$ is given by

$$\mathrm{d}p_c = \mathrm{d}\sigma_c (R + r\cos\alpha)\theta T, \tag{4-8}$$

where σ_c is the circumferential stress. Equaling Eq. (4-7) and Eq. (4-8) yields

$$\mathrm{d}\sigma_c = \sigma_x \frac{r\sin\alpha}{R + r\cos\alpha} \mathrm{d}\alpha, \tag{4-9}$$

and after the integration of α, we get the relationship between the longitudinal stress σ_x and the circumferential stress σ_c:

$$\sigma_c = \sigma_x \ln \frac{R + r\cos\alpha}{R + r}. \tag{4-10}$$

At a 3 cm bending diameter, $R = 15$ mm. Using the typical outer diameters of layers 1 and 6 of a STAR wire in Tab. 4-2, r equals 0.45 mm and 0.85 mm, respectively, and their stress function (Eq. (4-10)) curves are plotted in Fig. 4-11. As can be seen from the plots, the ratio between the circumferential stress and the longitudinal stress in both layers increases as α increases. The longitudinal stress is proportional to the distance between the point and the neutral plane (y=0); therefore, the circumferential stress equals zero at the outermost point, which is marked in green in Fig. 4-10, and reaches the maximum value at the innermost point, which is marked in orange in Fig. 4-10. In addition, because of the larger r value in layer 6, the circumferential stress in this outermost layer is larger than that in other layers. Since the circumferential stress is not affected by the gaps between tapes, at the innermost point, the outer layers are more vulnerable than the inner layers. From Fig. 4-12, it can be seen that a copper delamination happened right at the innermost point on layer 6 of a STAR wire with variable-tape-width configuration.

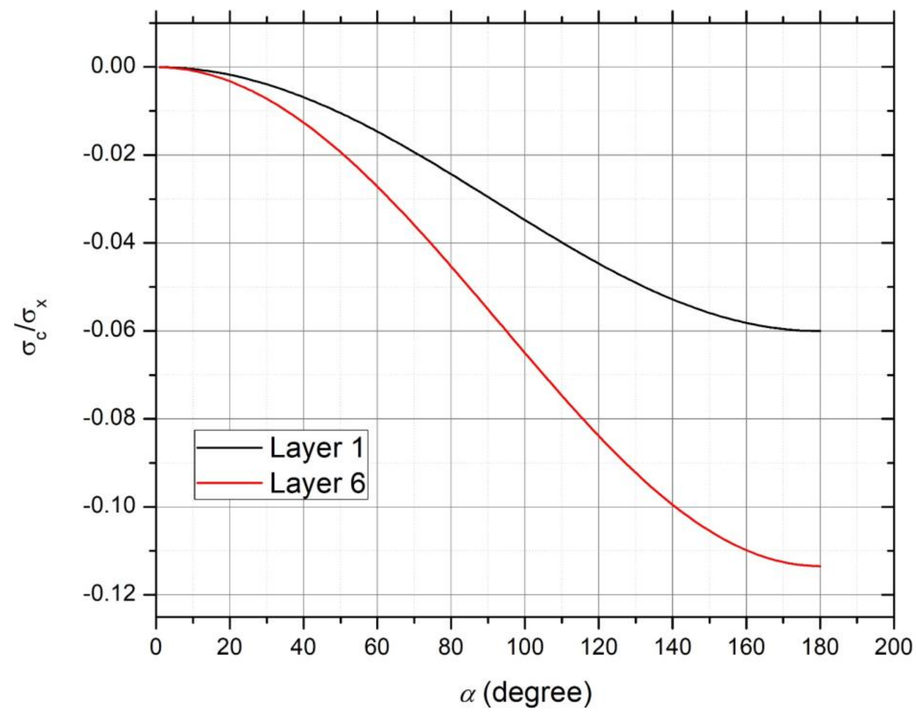

Fig. 4-11 Stress function comparison of two layers in STAR wire

Fig. 4-12 Variable-tape-width STAR wire in configuration-2 in bent form; delamination happened at innermost point

For the outer semi-circle (y>0) of the tube in Fig. 4-10, the longitudinal stress is tensile and the circumferential stress is compressive. For STAR wire, however, because the REBCO tape is wound in a helical pattern and gaps exist between turns, the longitudinal tensile stress is mostly released, with the assumption that the tape is relatively narrow. This can be proved by the increased gaps on the outer semi-circle, as shown in Fig. 4-12. For the inner semi-circle (y<0), on the other hand, both the longitudinal stress and circumferential stress are compressive. If the gaps are large enough, the longitudinal compressive stress can be largely released, which is confirmed by the compressed gaps on the inner semi-circle in Fig. 4-12; otherwise, the longitudinal stress accumulates and degrades the performance of the STAR wire.

Therefore, to avoid extra longitudinal stress accumulation on the inner semi-circle, the maximum tape width calculated in Tab. 4-2 should be adjusted. At different bending diameters D, the length of the inner semi-circle path is shorter than the length of the copper former, and the difference l_{diff} is

$$l_{diff} = \frac{\pi D}{2} - \frac{\pi(D-d)}{2} = \frac{\pi d}{2}, \tag{4-11}$$

where d is the outer diameter of the wire. For a STAR wire bent in a full circle, the number of turns n is expressed as

$$n = \frac{\pi D}{p} = \frac{\pi D}{\pi d \cos \vartheta} = \frac{D}{d \cos \vartheta}, \tag{4-11}$$

where p and ϑ are the twist pitch and wrap angle, respectively. Therefore, the adjusted maximum tape width w_{adj} equals the original maximum tape width w after subtracting the projection of the shortened length of the inner semi-circle path on each turn, i.e.,

$$w_{adj} = w - \frac{l_{diff}}{n} \cos \vartheta = \sin \vartheta \, \pi d - \frac{\pi(d \cos \vartheta)^2}{2D}, \tag{4-12}$$

and the calculated results are listed in Tab. 4-3. As the bending diameter of the STAR wire decreases, the adjusted maximum tape width also decreases.

Tab. 4-3 Adjusted maximum tape widths at different bending diameters (in mm)

Layer / Dia. (cm)	1	2	3	4	5	6
12	1.97	2.34	2.69	3.01	3.37	3.67
10	1.97	2.34	2.68	3.00	3.36	3.66
8.5	1.96	2.33	2.67	2.99	3.35	3.64
5.5	1.95	2.3	2.64	2.95	3.29	3.58
4	1.93	2.28	2.61	2.91	3.24	3.51
3	1.91	2.25	2.57	2.84	3.17	3.42

For configuration-1, with its variable-tape-width structure, at bending diameters of 8.5 cm and 5.5 cm, the tape widths are below the adjusted maximum tape widths, whereas at the bending diameter of 3 cm, the tape widths exceed the adjusted maximum tape widths and extra longitudinal stress accumulates on the inner semi-circle. For layer 6, assuming that no plastic deformation occurs, the extra longitudinal strain reaches 2.24%. That is why the I_c degraded more as it was bent from 5.5 cm to 3 cm in diameter than from 8.5 cm to 5.5 cm in diameter. For the variable-tape-width structure of configuration-2, even at the smallest bending diameter of 3 cm, the tape widths are still below the adjusted maximum tape widths, except the first layer, which partially explains why the degradation is less than that in configuration-1.

It is worth noting that in the simplification of Eq. (4-4), $\sin\frac{\theta}{2} \approx \frac{\theta}{2}$ is only valid at small bending angles. The larger the bending angle, the more the actual value deviates from the simplified equation. For STAR wires, therefore, the narrower the tape, the more accurate the assumption that the longitudinal stress is released by the gaps between turns. For the variable-tape-width STAR wire in configuration-2, the tape widths in each layer are narrower than those in configuration-1, which helps with the longitudinal stress release and provides higher I_c retention.

Compared to the manually-wound sample discussed in section 4.1.1, the STAR wires fabricated with the automatic machine are more compact in the radial direction and have less space between layers. On one hand, machine winding increases the mechanical strength and J_e value of the wire; on the other hand, due to the decreased space between layers to accommodate the bending deformation, these REBCO tapes experience more stress during wire bending. This is the probably why the manually-wound sample exhibited a higher I_c retention than the machine-wound samples.

In general, because of the higher filling factor, the variable-tape-width structure can provide higher I_c and J_e values in the straight form. In the bent form, if the tapes are wider than the adjusted maximum tape width in that bending diameter, which should be avoided, extra longitudinal stress is accumulated and the performance is affected. Even if the tapes are narrower than the adjusted maximum tape width, wider tapes also experience more bending stress than narrower tapes, especially at small wire bending diameters. Therefore, for applications that do not require small bending diameters, moderately increasing the tape width can improve the overall performance, whereas for applications that require excellent bending performance, narrower tapes are preferred.

4.1.3 Multiple-tapes-in-a-single-layer (MTISL) structure

To overcome the bending performance degradation of the variable-tape-width structure while maintaining a high filling factor, the MTISL structure is proposed. In this structure, multiple tapes are co-wound in one layer simultaneously. Since the tapes in the same layer can deform independently during wire bending, the first reason why variable-tape-width structure degrades in the bent form, i.e., the large tape width, is avoided. If the width summation of all tapes in the same layer is less than the adjusted maximum tape width, then there is no extra longitudinal stress, and thus the second reason for the bending performance degradation is also avoided.

Tab. 4-4 Tape number and width of a MTISL structure STAR wire

Layer	1	2	3	4	5	6
Wire O.D. (mm)	1.18	1.33	1.48	1.62	1.78	1.95
Max total tape width at 3 cm (mm)	2.50	2.76	3.05	3.31	3.61	3.89
Single tape width (mm)	2.50	2.50	2.50	2.50	1.80	1.80
Number of tapes in one layer	1	1	1	1	2	2
Tape width gain	1	1	1	1	1.44	1.44

A 20 cm long, 6-layer MTISL STAR wire was fabricated and the specifications of the tapes used for winding are listed in Tab. 4-4. Although tapes with widths less than 2 mm are very fragile and not easy to fabricate at consistently high quality, several pieces of 1.8 mm wide tapes were still produced to test this structure. Instead of a 20-AWG former, an 18 AWG copper former was used to increase the wire's outer diameter and provide more space to accommodate more than one tape in a single layer. The tape width of the first four layers was constant at 2.5 mm. For the fifth and sixth layers, the adjusted maximum tape widths at the 3 cm bending diameter exceeded 3.6 mm and two pieces of 1.8 mm wide tape were used. The tape width gain is the ratio between the tape width summation in this structure and the 2.5 mm tape width used in the fixed-width structure. By winding two tapes in each of the last two layers, the total tape width increases from 15 mm to 17.2 mm.

Fig. 4-13 shows a photograph of the fifth and sixth layers of the MTISL STAR wire. As can been seen from the photograph, multiple bulges are observed at the edges of tapes in the fifth layer. This is because the maximum tape width allowed in the straight form is 3.72 mm, which is only 0.12 mm larger than the tape width summation of 3.60 mm; therefore, precisely winding two tapes at the same time is necessary. However, the two tapes that are wound simultaneously are not identical and the winding force also changes slightly between them. Any axial slide of the tape causes the tape edges to touch each other and results in bulges. Because of the same winding precision issue, the gaps shown in the sixth layer are also not very uniform. As a result, the final outer diameter of this wire is also larger than that of the wires with a normal structure. This demonstrates the difficulties in fabricating small STAR wires with a MTISL structure.

Fig. 4-13 The fifth and sixth layers of MTISL STAR wire

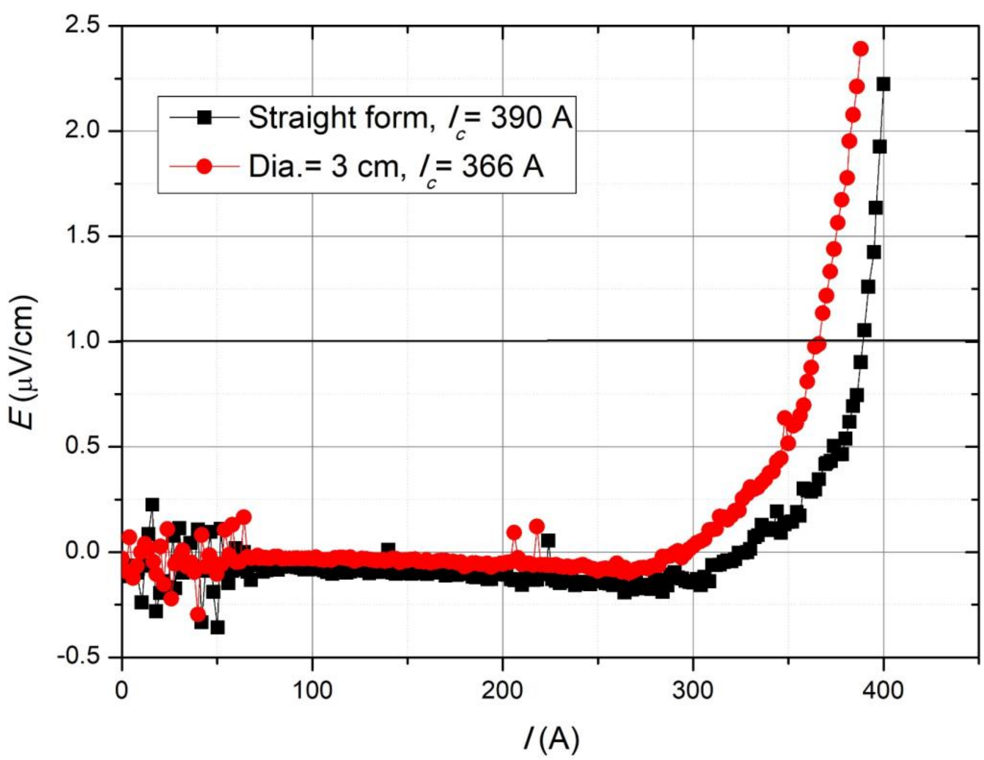

Fig. 4-14 *E-I* characteristics of MTISL STAR wire

The I_c summation of the flat tapes is 476 A due to the relatively low I_c value of the parent 12 mm wide tape. After fabrication, the MTISL STAR wire was first tested in the straight form and then bent into the 3 cm bending diameter; the *I-E* characteristics are shown in Fig. 4-14. In the straight form, the I_c of the wire is 390 A, which corresponds to an 82% retention between the tape I_c summation and the straight wire I_c. This relatively high I_c retention is due to the large copper core. After bending the wire into the 3 cm diameter, the I_c value is still maintained as high as 366 A, which corresponds to 94% retention. This result proves the efficacy of the idea of using several narrow tapes as a substitute for a wide tape to increase the bending performance while maintaining a high filling factor. Because of the bulky size and low tape I_c, the J_e of the MTISL structure STAR wire at the 3 cm bending diameter is 123 A/mm^2.

In general, the MTISL structure is suitable for large STAR wires with more than six layers (on the 18 AWG former) or eight layers (on the 20 AWG former) that also require good bending performance. As the number of layers increases, the gap between turns also increases in the fixed tape width structure, whereas the MTISL structure takes advantage of the gaps to increase the current capacity of the wire. In addition, the extra support from the multiple tapes can potentially increase the wire's in-field performance because of its higher mechanical strength; however, the difficulties in precisely winding multiple tapes simultaneously and fabricating tapes that are narrower than 2 mm wide make the MTISL structure less favorable for fabricating smaller STAR wires.

4.1.4 Optimal-tape-width structure

In the previous three sections, several STAR wire structures were discussed and analyzed. They are suitable for different applications, but the I_c and J_e values are relatively low: at 77 K self-field, under a 3 cm bending diameter, the I_c values are lower than 370 A and the J_e values are lower than 140 A/mm^2. In this section, the optimal-tape-width structure is presented, aiming at increasing both the I_c and J_e values at the 3 cm bending diameter.

Based on the results of the variable-tape-width structure, it was observed that the tapes as wide as 3 mm are easily damaged at the edges during bending tests; therefore, the maximum tape width of the optimal-tape-width structure was limited to 2.5 mm. In addition, the STAR wire with the 18 AWG former shows a 33% higher tape-to-wire I_c retention than the wires with the 20 AWG former, which is why the 18 AWG copper former was chosen for the optimal-tape-width structure. To further increase the I_c values, the 18 AWG former of one wire was replaced with a 20 AWG copper former wound with two layers of 2 mm wide REBCO tapes since the latter structure had a higher REBCO-to-copper ratio.

Tab. 4-5 Specifications of optimal-tape-width structure wires

STAR wire No.	Former size	No. of layers	Tape width (mm) ×No. of tapes	Total tape width (mm)	O.D. (mm)
R1	18 AWG	8	2.5×8	20	1.85
R2	18 AWG	6	2.5×6	15	1.73
R3	20 AWG	8	2×2, 2.5×6	19	1.78

Three 9 cm long optimal-tape-width structure wires were fabricated and their specifications are listed in Tab. 4-5. The parent 12 mm wide tape, which was used to produce the narrow tapes, had an average I_c of 490 A and the thickness before electroplating was between 20 and 25 μm. STAR wires R1 and R2 have similar structures, though R1 has two more layers of 2.5 mm wide tape than R2. As previously mentioned, R3 has two layers of 2 mm wide tape on the 20 AWG former instead of the 18 AWG former, and the outer diameter of R3 is slightly larger than R2 because of that. In high current situations, since the structure of the copper terminal plays an important role in the wire's performance, which will be discussed later in this chapter, the copper terminals shown in Fig. 4-15 were used. The large contact area between the copper terminal and the wire end reduces the contact resistance and the heat generated in high current tests. The wires were first tested in the straight form and then bent into the 3 cm diameter half-circle.

Fig. 4-15 Copper terminals with large contacting area and low resistance

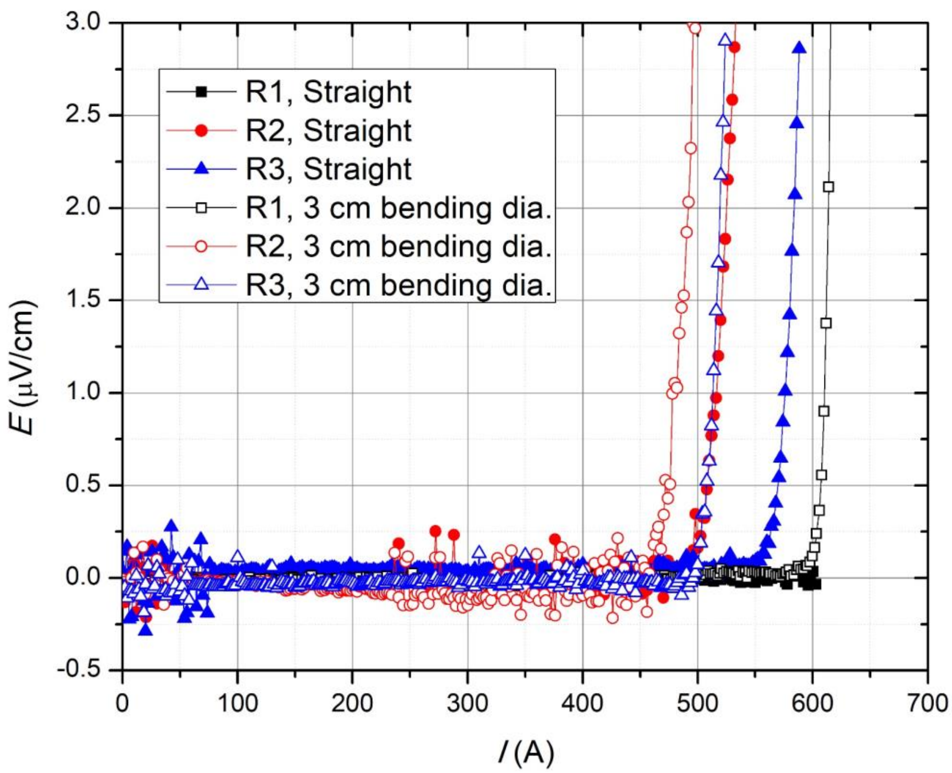

Fig. 4-16 *E-I* characteristics of the optimal-tape-width structure STAR wires

The *E-I* characteristics of the three wires are plotted in Fig. 4-16 and the I_c , J_e, and retention values are listed in Tab. 4-6, where retention-1 is the ratio between the tape I_c summation and the straight wire I_c, whereas retention-2 is the ratio between the straight wire I_c and the bent wire I_c. In the straight forms, because of the large former size and wide total tape width, the I_c of all wires exceeded 500 A. In terms of J_e, the compact size and high parent tape I_c also helped to increase the J_e of all wires to over 220 A/mm^2. For R1, due to the current source limitation, a transition could not be reached and the I_c was more than 610 A. Comparing R2 and R3, the 2 mm wide tapes in the first two layers of R3 provide 60 A of extra current, but the current per unit width of tape drops from 34.3 A/mm in R2 to 30.3 A/mm in R3, which indicates that the first two layers of tape have a lower-than-average performance, compared to the outer layers.

Tab. 4-6 Test results and retention of optimal-tape-width structure STAR wires

Wire #	Tape total width	Tape I_c sum.	Straight form			Bent form		
			I_c (A)	J_e (A/mm^2)	Retention-1 (%)	I_c (A)	J_e (A/mm^2)	Retention-2 (%)
R1	20	819	> 610	>223	>74.5	611	218	N/A
R2	15	626	516	220	82.4	478	203	92.6
R3	19	771	576	237	74.2	514	207	89.2

In bent form, the I_c slightly drops but the retention values are about 90% those of the straight form. With the high I_c values, the J_e of all wires still remained above 200 A/mm^2. For R2 and R3, since the first two layers of tape in R3 experience extra strain during wire bending, the difference in performance is even less: with a 26.6% wider total tape width, R3 has only a 7.5% higher I_c value and 1.9% higher J_e value in the 3 cm bent form. R1, on the other hand, with a 33.3% wider total tape width than R2, provides a 27.8% higher I_c value and 7.4% higher J_e value.

In general, STAR wires with 6 to 8 layers of 2.5 mm wide tapes on an 18 AWG former, i.e., the optimal tape width structure, have higher I_c and J_e values in both the straight and bent forms. Using the same width for all tapes also reduces fabrication difficulties. The idea of replacing an 18 AWG copper former with a smaller former to accommodate more tapes does not boost the wire performance significantly.

4.1.5 10 m STAR wire

After comparing different STAR wire structures, the optimal tape width structure was selected to fabricate a 10 m long STAR wire. Unlike short STAR wire samples, fabricating long wires propose new challenges regarding tape uniformity and winding system stability since the chance of having a weak point in the STAR wire increases substantially as the length of the wire increases.

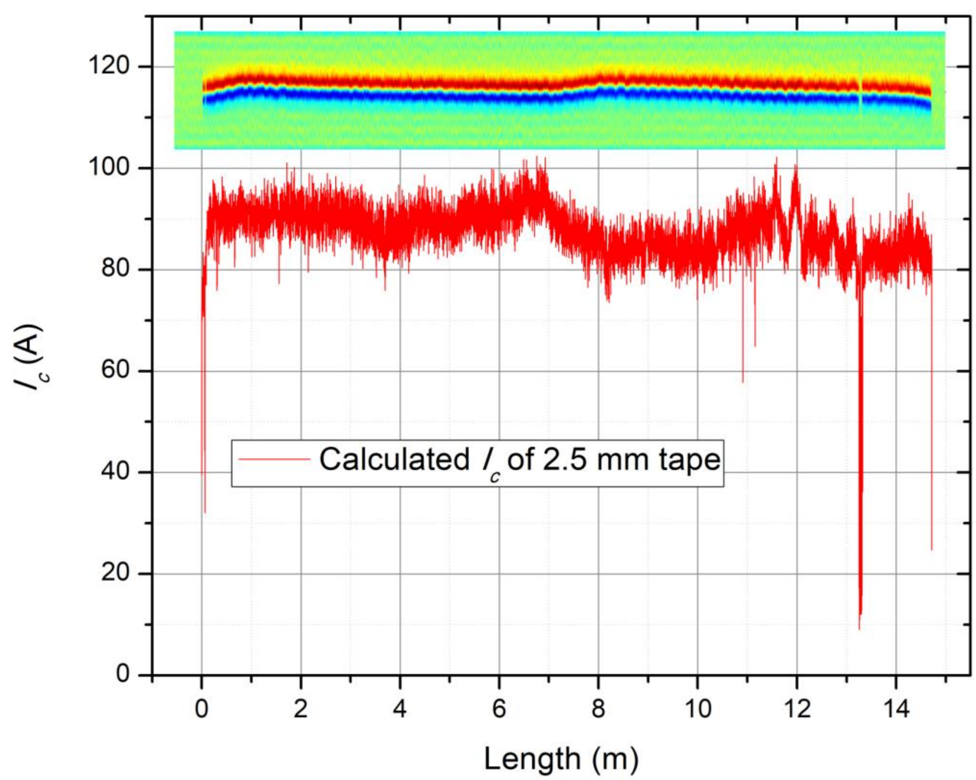

Fig. 4-17 Trapped field maps of SHPM and the corresponding calculated I_c of a 2.5 mm wide tape

Twelve pieces of 14.5 to 16.5 m long, 2.5 mm wide REBCO tapes were prepared and the reel-to-reel SHPM was used to test their local I_c values. For tapes with this length, it is difficult to find one without any defect; therefore, the I_c plots calculated by the trapped field maps of SHPM were used to determine which defects were acceptable and which must be avoided. Fig. 4-17 shows the I_c plot of a 14.5 m tape. As can be seen from the plot, the average I_c is 86 A and several weak points are observed. The weak point at 13.2 m is 6 cm long and only maintained 14% of the original I_c, which would affect the performance of the STAR wire severely if used for winding and therefore must be avoided. Other weak points, like the ones at 10.9 m and 11.1 m, are acceptable since their lengths are only 1 mm and around 70% of the I_c values are maintained.

Using this method, the best tapes were selected from the twelve tapes for winding. Since the tapes are relatively thick, to keep the outer diameter of the STAR wire less than 2 mm, 7 layers were used for winding. The tapes' average I_c, the lowest I_c that considered all weak points, and the outer diameter of the wire are listed in Tab. 4-7. The lowest I_c summation was 229 A lower than the average I_c summation.

Tab. 4-7 Specifications of the 10 m STAR wire

Layer	1	2	3	4	5	6	7	Total
Average I_c (A)	103	100	106	98	96	99	101	703
Lowest I_c (A)	65	72	90	82	64	56	55	474
Tape thickness (μm)	52	52	50	56	55	52	50	N/A
O.D. (mm)	1.14	1.26	1.36	1.58	1.69	1.80	1.90	N/A

After winding, the wire ends were soldered into a pair of 12 cm long copper terminals, as shown in Fig. 4-18 (a). The final length of the STAR wire between the two terminals was 10.22 m. Since the wire was too long to be tested in a straight form, a 3D-printed mandrel with 22 turns of groove on the surface was used to hold the wire and test in liquid nitrogen, as demonstrated in Fig. 4-18 (b). The extra field induced by the solenoid-like shape was also considered. Two pairs of voltage taps were used to read the wire's voltage during tests, where voltage tap 1 is on the outmost layer and 11 cm away from the copper terminals and voltage tap 2 is on the copper terminals. In addition, another nine voltage taps, at 1 m intervals in the middle of the wire, were used for section-by-section voltage reading, which will be discussed later in this chapter.

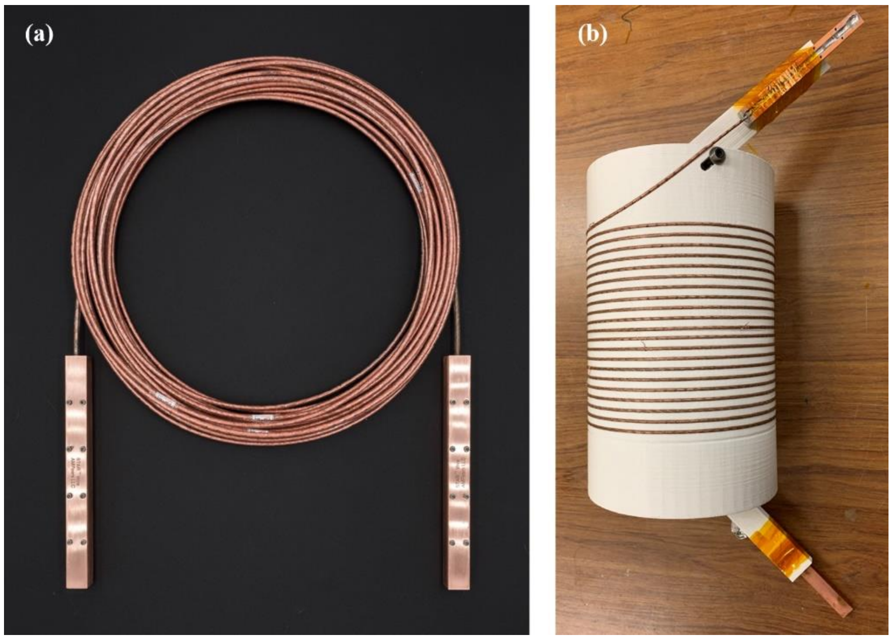

(a) Overview of 10 m STAR wire with copper terminals; (b) 3D-printed mandrel for testing

Fig. 4-18 10 m long STAR wire

The *E-I* characteristics are plotted in Fig. 4-19. Since the 3D-printed mandrel shrunk in liquid nitrogen and couldn't support the wire well, small vibrations were observed at low current values, which is why the current was ramped up from 200 A. The I_c values determined from voltage tap 1 and voltage tap 2 were 476 A and 467 A and the J_e values were 165 A/mm^2 and 168 A/mm^2, respectively. The different values indicate that the current re-distribution happened in the copper terminals: as the I_c value of each tape is not exactly the same, when a low I_c tape reaches its current limit, the high I_c tape is still capable of carrying more current; thus the extra current is re-distributed to the latter tape through the copper terminals and causes different voltage readings between the terminals and outer layers. The difference is only 2.4% of the I_c value, proving that the resistance of the terminal is low enough to effectively re-distribute current between tapes.

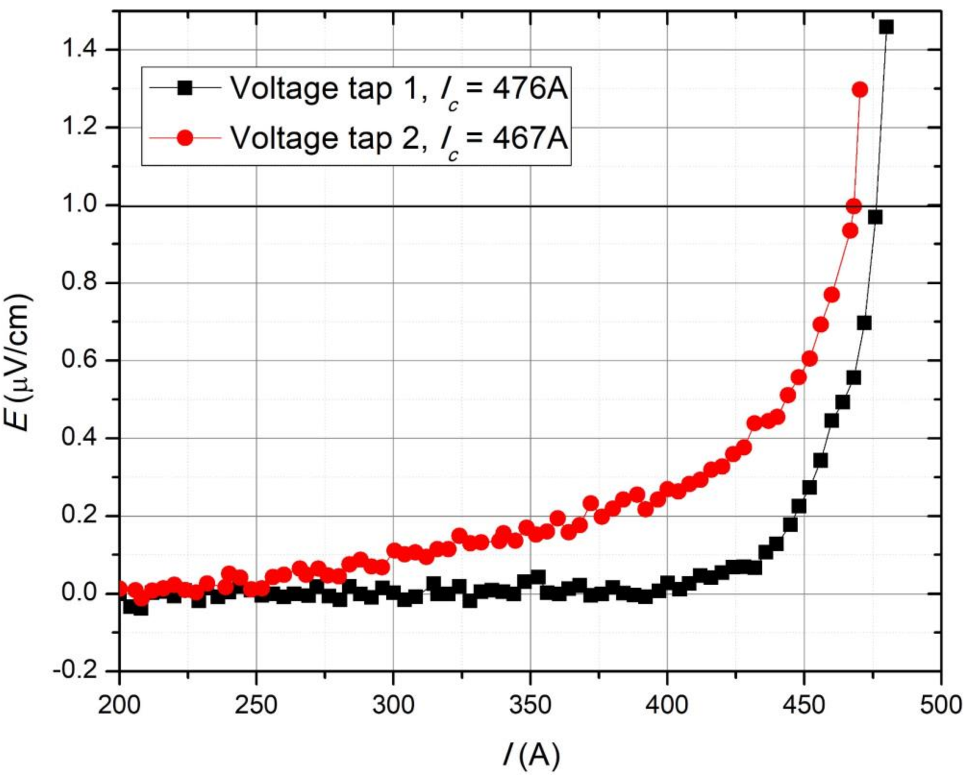

Fig. 4-19 *E-I* characteristics of the 10 m STAR wire

Due to the solenoid-like shape, the largest magnetic field near the wire surface was 153 mT, whereas a straight wire with the same current had a 99 mT magnetic field near its surface. With the magnetic field parallel with the tape surface, the I_c value at 99 mT is around 20% higher than the I_c value at 153 mT [101]. It is worth mentioning that the outer layer was affected more by the increased magnetic field than the inner layer since the magnetic field was reduced inside the wire. Assuming an average 10% I_c reduction for all tapes, an I_c value of approximately 525 A is expected in the straight form for the 10 m STAR wire.

Based on the previous test results of STAR wires on an 18 AWG former, 80% to 85% retention is expected between the tape I_c summation and the straight wire I_c; thus, the straight wire I_c value of 525 A corresponds to the tape I_c summation of 618 A to 656 A. Comparing the tapes' lowest I_c summation of 474 A and the tapes' average I_c summation of 703 A in Tab. 4-7 reveals that current was shared between layers. When reaching a weak point in one layer, current in this layer transfers to other layers and bypasses the weak point, which is why the actual I_c value of the wire was higher than the value calculated from the lowest I_c summation of the tapes.

In general, the 77 K test results of the 10 m wire prove the feasibility of fabricating long STAR wires. Although the J_e value of the wire is relatively low due to the thicker tapes, the I_c value is promising. With the current sharing ability, the long STAR wires made by tapes with defects can still possess good performance.

4.1.6 Summary

In this section, the 77 K electrical performance of STAR wires with different structures was discussed. With the help of the automatic winding system, the high I_c thin tapes, and the low-resistance copper terminal structure, the electrical performance of STAR wires was improved substantially: at a 3 cm bending diameter, the self-field I_c and J_e were increased from the initial values of 232 A and 116 A/mm^2 to 611 A and 218 A/mm^2 and the length increased from 7.5 cm to 10.22 m. Based on the test results, the following conclusions can be made:

1) The variable-tape-width structure STAR wires are suitable for use in straight form or with large bending diameters; as the bending diameter decreases, the tape width should be narrowed to maintain a good bending performance.
2) The MTISL structure increases the filling rate while maintaining the bending performance; to fully take advantage of this structure, large diameter STAR wires are preferred.
3) Under the 3 cm bending diameter, STAR wires with 6 to 8 layers of 2.5 mm wide tape and an 18 AWG former provide the best performance.
4) Current re-distribution and sharing between layers occurs in long STAR wires.

4.2 In-field performance of STAR wires

This section presents the in-field test results of STAR wires. The performance of single-layer STAR wires, including their angular dependence and field dependence at different temperatures, is discussed first. Afterwards, the in-field test results of multi-layer STAR wires, both with and without indium filling, are compared. The field dependence, degradation, and repeatability in high fields are analyzed. Unlike 77 K self-field tests, the voltage criteria used for the in-field tests at different temperatures were not the same and will be stated individually.

4.2.1 Single-layer STAR wire performance

One advantage of the STAR wire is its isotropic structure and insensitivity to the direction of magnetic fields [89]. In the early stages of STAR wire development, the angular dependence was tested on the single-layer structure. At 77 K in a 1 T magnetic field and at 30 K in a 3 T magnetic field, the I_c of a single-layer STAR wire was measured at different angles to the magnetic field. One layer of 2 mm wide symmetric tape was manually wound onto a 1.1 mm brass former with the REBCO side facing inwards. The twist pitch was 3 mm and the total length of the wire was 18 mm. At the 1 μV/cm voltage criterion, the I_c of the STAR wire in self-field was 37.4A.

The angular dependences of I_c are plotted in Fig. 4-20 [89]. To avoid the relatively high background noises, 2 μV/cm and 3 μV/cm criteria were used at 77 K and 30 K, respectively. The angle is defined in the plane that is perpendicular to the axis of the wire. At 77 K, 1 T, in the angle that ranged between -93° and 35°, the minimum I_c value was 9.2 A and the maximum value was 10.2 A, which corresponds to an 11.3% variation. At 30 K, 3 T, the minimum value was 101.9 A and the maximum value was 107.0 A, which corresponds to an 8.2% variation. The reason for this small fluctuation in I_c is that manual winding is not ideal and the wire ends are not fully isotropic. Nevertheless, these variations in the angular dependence of I_c are far less than those measured in flat REBCO tapes, where the difference between the minimum and maximum I_c values can be over 100% at 77 K, 1 T and over 160% at 30 K, 3 T [89].

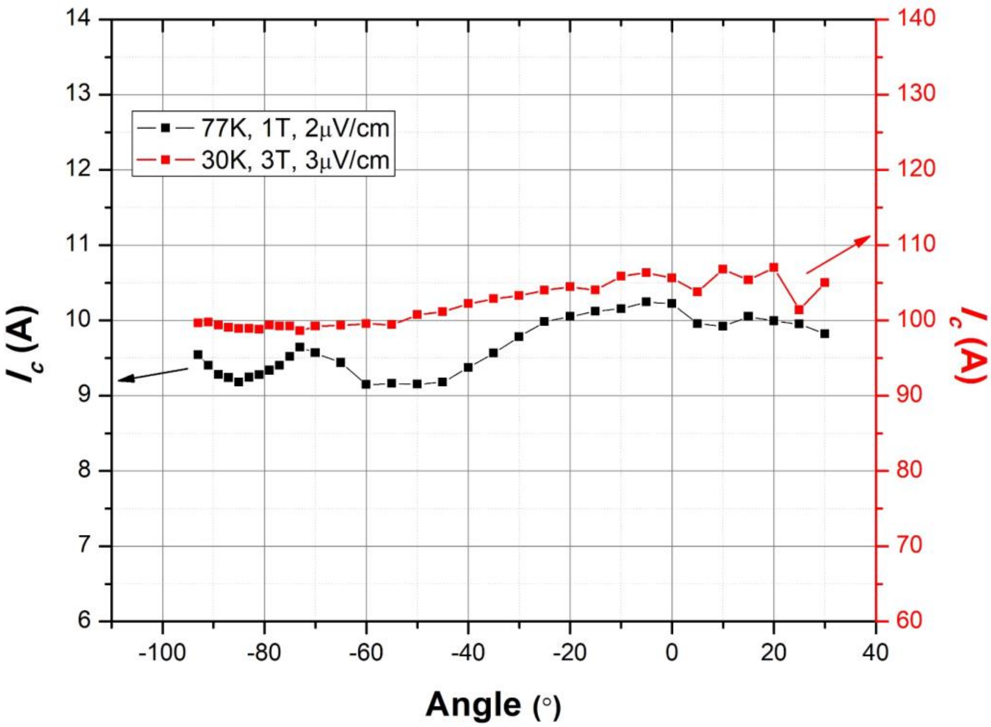

Fig. 4-20 Angular dependence of I_c of a single-layer STAR wire at 77K, 1T and 30K, 3T

In addition to the angular dependence of STAR wire, the magnetic field dependence of I_c was also measured. Another single-layer STAR wire, with the same specifications as the previous one, was made. The I_c values were measured over a temperature range between 30 K and 77 K in a up to 9 T magnetic field perpendicular to the axis of the wire.

The field dependences of I_c are plotted in Fig. 4-21 [89]. As can be seen from the plot, at 30 K, in the highest magnetic field of 9 T, the critical current of the STAR wire was 42 A. Comparing the zero-field I_c of 50 A at 77 K and the in-field I_c of 132 A at 30 K, 2.5 T reveals a lift factor of 2.64. Because of the isotropic structure of the STAR wire, the lift factor is maintained at the same value as the wire rotates about its axis. For the same Zr-added REBCO tapes, in magnetic fields applied parallel to the tape surface (B ∥ a–b), a lift factor of 5.7 was calculated between the I_c values at 77 K, 0 T and 30 K, 2.5 T; in magnetic fields that were applied perpendicular to the tape surface (B ∥ c), a lift factor of 2.63 was calculated under the same conditions [60]. It is observed that the lift factor of the STAR wire is very close to that of the tape in magnetic fields perpendicular to the tape surface. In a magnetic field perpendicular to the axis of a STAR wire, because of the spiral shape of the tapes in the wire, the angle between the tape surface and the field changes periodically between 0° and 90°. This indicates that the in-field performance of STAR wire is limited by the point in the tape where the magnetic field is perpendicular to the tape surface.

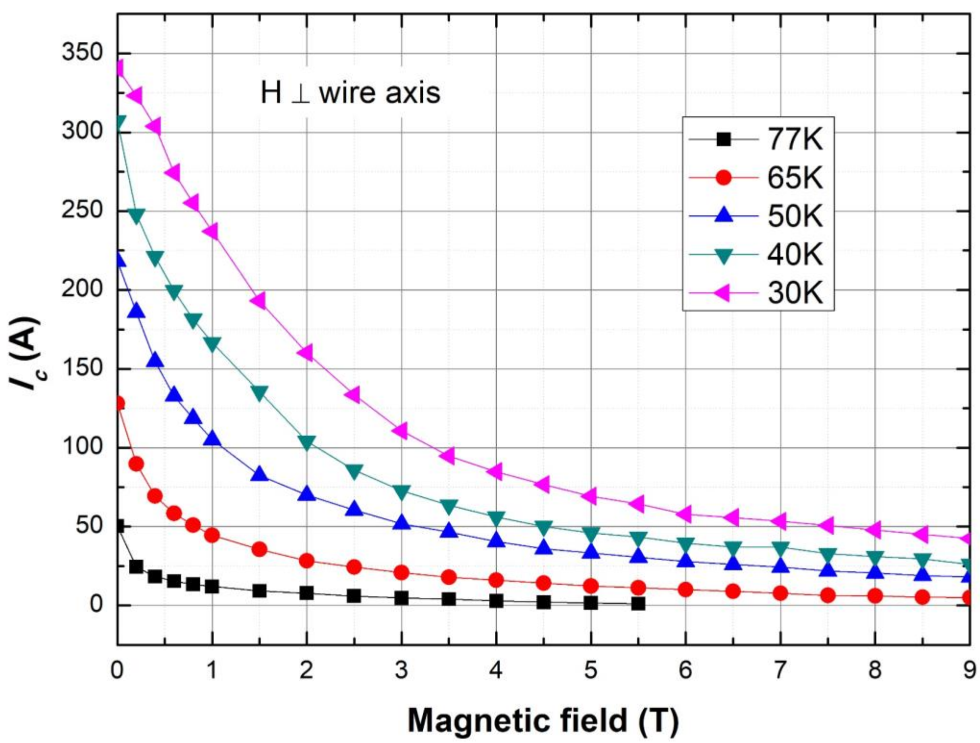

Fig. 4-21 Magnetic field dependence of I_c of a single-layer STAR wire in fields perpendicular to the wire axis

4.2.2 Performance of multi-layer STAR wires without indium filling

4.2.2.1 Sample holder structure and STAR wire specifications

To test the performance of STAR wires in high magnetic fields, several multi-layer STAR wires were prepared and tested in a 31.2 T, 50 mm bore magnet at the NHMFL. Since the inner size of the bore is only 38 mm, considering the STAR wire size and the clearance for loading and unloading samples, the maximum allowed bending diameter for the STAR wire is 32 mm. For a better comparison with previous bending test results at 77 K, the bending diameter of STAR wire in the magnet was set to the same value of 30 mm. To support the huge Lorentz force applied on the STAR wires in high field tests, a sample holder, displayed in Fig. 4-22 [90], was designed.

A two-piece main body of the holder was made from G10 and connected together with non-magnetic, stainless-steel screws. The long STAR wire copper terminals, which were designed to provide a large contact area with the wire, were mounted on the main body and aligned along the magnet bore axis. The STAR wire was bent in a 30 mm diameter half-circle and rested on the stage-shape edge of the main body. In this configuration, the magnetic field is perpendicular to the center of the wire and the current direction is arranged such that the resulting Lorentz force presses the wire against the holder. The middle part of sample is positioned at the magnet center and the field distribution of the magnet ensured a field strength variation less than 3% along the bore axis in a range of ±10 mm.

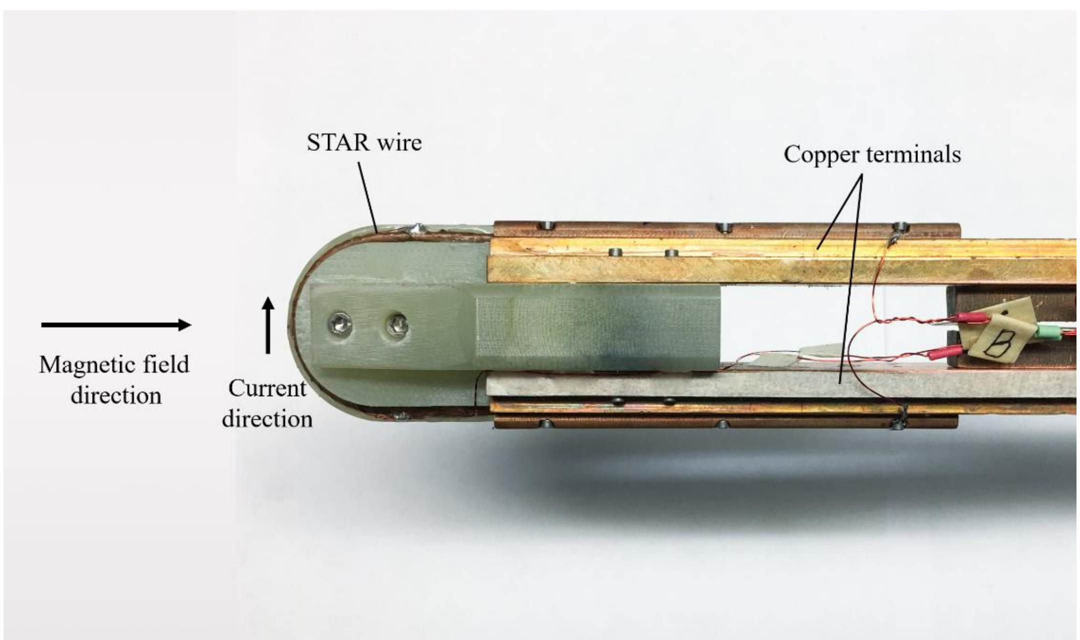

Fig. 4-22 G-10 sample support with a STAR wire mounted on it

Tab. 4-8 Specifications of STAR wires without indium filling

Wire No.	Former size	Wire O.D. (mm)	No. of layers	Tape width (mm)×No. of tapes	Total tape width (mm)
R1	18 AWG	1.89	8	2.5×8	20
R2		1.91	8	2.5×8	20
R3		1.70	6	2.5×6	15
R4		1.69	6	2.5×6	15
R5		1.68	6	2.5×6	15

Five STAR wires were fabricated and their specifications are listed in Tab. 4-8. The 9 cm long wires used the optimal tape width structure so that six or eight layers of 2.5 mm wide symmetric tapes were wound on 18 AWG copper cores. The cross-section photographs of both the 6-layer and 8-layer STAR wires are shown in Fig. 4-23 [90, 98]. The parent 12 mm wide REBCO tapes, which were used to produce the symmetric tapes, have a nominal I_c of 490 A at 77 K, self-field and 849 A at 4.2 K, 15 T.

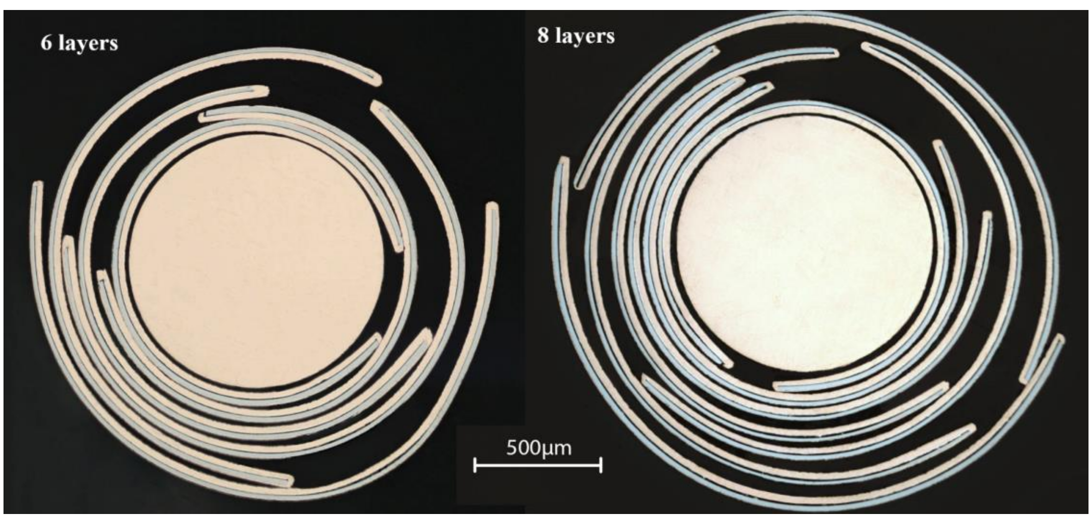

Fig. 4-23 Cross-section photographs of 6-layer and 8-layer STAR wires

The STAR wires were first tested in a straight form and the 3 cm diameter bent form at 77 K, self-field, with a 1 μV/cm criterion. The I_c and J_e values and retentions are listed in Tab. 4-9, where retention-1 is the ratio between the tape I_c summation and the straight wire I_c, whereas retention-2 is the ratio between the straight wire I_c and the bent wire I_c. Due to the different symmetric tapes used for winding, the current per unit width of the tapes varies by about 5 A/cm. Except for R1, the optimal tape wide structure makes the J_e value of the different STAR wires similar to each other in both the straight and bent forms. For R1, because of the relatively small outer diameter and high tape I_c summation, the J_e value of 218 A/mm^2 in the bent form is 14% higher than the average value of the other wires. For the I_c values, STAR wires with an 8-layer structure have an average 32% higher I_c values than that of the wires with a 6-layer structure, which corresponds to their total tape widths.

Tab. 4-9 I_c, J_e values and retentions of STAR wires without indium filling at 77 K, self-field

Wire No.	Tape I_c sum.	Total tape width (mm)	Straight form			Bent form		
			I_c (A)	J_e (A/mm^2)	Retention-1 (%)	I_c (A)	J_e (A/mm^2)	Retention-2 (%)
R1	819	20	>610	>223	>74.5	611	218	N/A
R2	754	20	608	212	80.6	542	189	89.1
R3	627	15	510	225	81.4	440	193	85.8
R4	635	15	476	213	75.0	418	187	87.8
R5	563	15	478	216	84.9	435	196	90.7

4.2.2.2 Test results at 4.2 K in background magnetic fields

After the 77 K tests, five STAR wires with a 3 cm bending diameter were tested in background fields at 4.2 K. Wax was applied around the STAR wire to prevent movement at high currents. The applied magnetic fields ranged from 14 to 31.2 T. In fields higher than 18 T, helium bubbles usually formed around the sample and were trapped because of the magnetic force. These bubbles obstructed the thermal contact between the wire and liquid helium. Therefore, the magnetic field

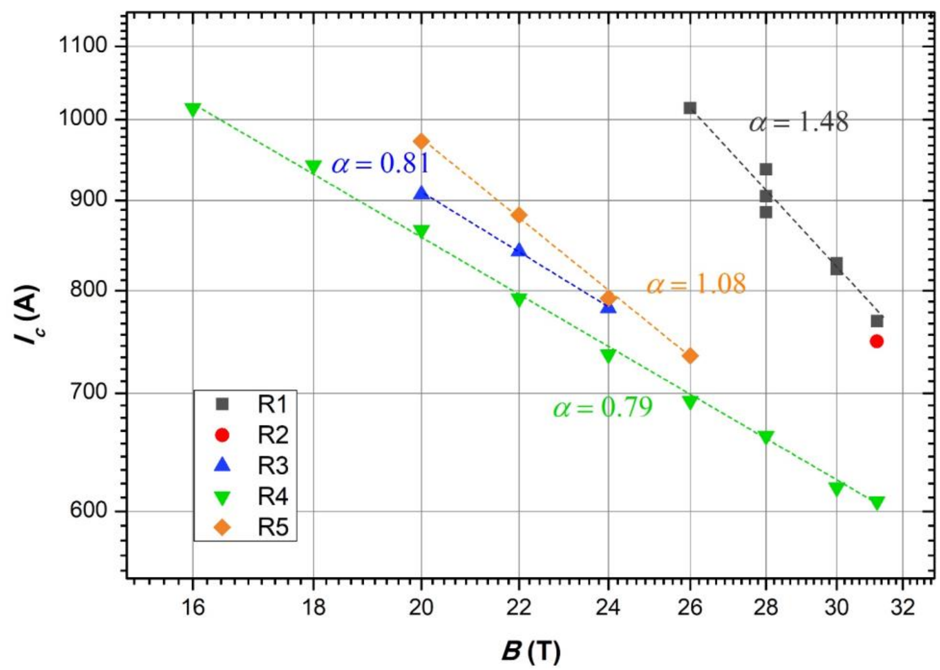

Fig. 4-24 Magnetic field dependence of I_c of STAR wires without indium filling between 16 and 31.2 T at 4.2 K

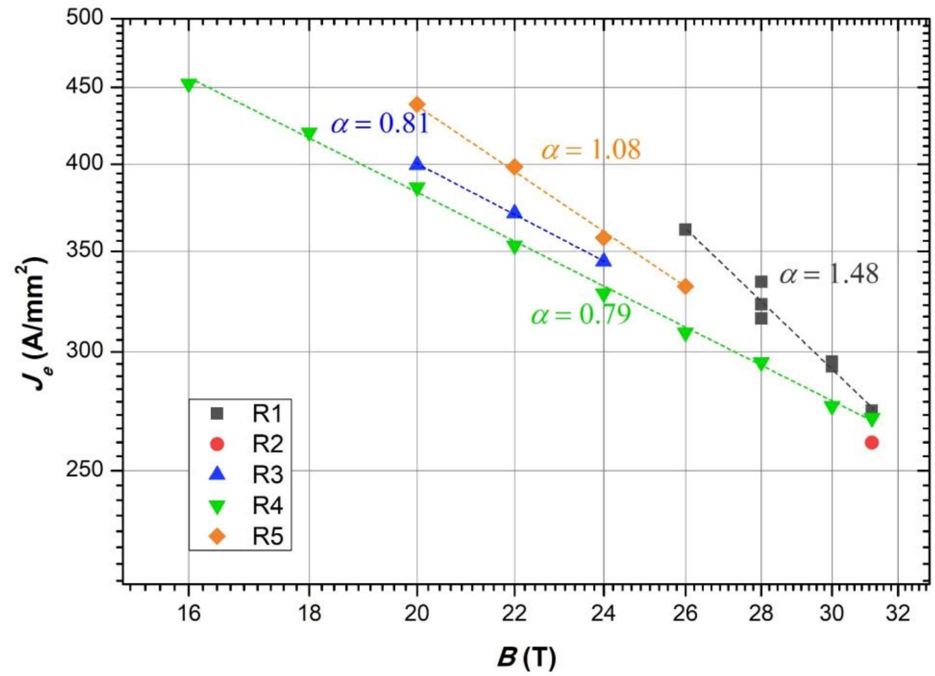

Fig. 4-25 Magnetic field dependence of J_e of STAR wires without indium filling between 16 and 31.2 T at 4.2 K

was ramped down to fields lower than 18 T between each test to release the bubbles. R2 and R4 were measured from the highest field of 31.2 T to lower fields, whereas R1, R3, and R5 were measured from the 20 T field to higher fields.

Due to the power source limitation, currents were limited to 1050 A and the ramping rate in normal mode was 17 A/s. Pulse current mode was used for all wires in high magnetic fields. In this mode, currents higher than a threshold do not ramp up continuously; instead, the current pulses up to a desired high value, which increases gradually in each cycle, and then jumps back to a lower value between pulses. This mode allows the sample to cool thoroughly to prevent overheating. The voltage criterion used to determine the I_c values in all the 4.2 K measurements was 0.5 μV/cm.

The magnetic field dependence of the I_c and J_e of STAR wires between 16 and 31.2 T at 4.2 K are plotted in Fig. 4-24 and Fig. 4-25 [90], respectively. The short-dashed lines shown in the figures are linear fits of each sample's data and their slopes are the α values, which are also listed in the plots. The relationship can be described by the power-law functions

$$I_c(B) = I_c(0)B^{-\alpha}, \quad J_e(B) = J_e(0)B^{-\alpha}, \tag{4-13}$$

where $I_c(B)$ and $J_e(B)$ are the critical current and critical engineering current density at a magnetic field B.

For the 6-layer STAR wires R3, R4, and R5, because of their similar 77 K electrical performance and outer diameters, the I_c and J_e values were similar at 4.2 K. R3 had the highest 77 K electrical performance in 6-layer STAR wires, whereas at 4.2 K, 20 T, the I_c is 907 A and the corresponding J_e was 400 A/mm^2, which is around the average performance of the three wires. After performing three measurements between 20 T and 24 T, R3 was burned due to a thermal runaway. Quench protection voltage was adjusted to protect the remaining samples. R4 had the lowest 77 K and 4.2 K electrical performances among the three 6-layer wires, but it was the only sample that survived the all tests from 16 T to 31.2 T, without any degradation or thermal runaway, which may be due to the lower current and thus decreased Lorentz force. R4's measured I_c was 1015 A with a corresponding J_e of 452 A/mm^2 at 16 T and 608 A with a corresponding J_e of 271 A/mm^2 at 31.2 T. R5 had an I_c of 972 A with a corresponding J_e of 438 A/mm^2 at 20 T, which was the highest electrical performance at 4.2 K. However, degradation was observed after several repeated measurements at 26 T, and so measurements at higher fields were abandoned to prevent further damage.

Fig. 4-26 Burnt STAR wire R2 after testing at a 31.2 T background field

For the 8-layer STAR wire R1, because of the power source limitation, the transition to the normal state could be reached only above 26 T. At 26 T, the measured I_c was 1015 A, which was much higher than that of the 6-layer STAR wires. When comparing J_e, R1's value of 362 A/mm^2 is still 9% higher than that of R5. At 28 T and 30 T, measurements were repeated several times in pulse current mode. After three measurements at 28 T, the I_c dropped from 937 A to 886 A, which corresponds to a 6% decrease. At 30 T, the I_c dropped about 1% in two tests. After multiple degradations, the J_e value of R1 at 31.2 T was basically the same as that of R4. For R2, the wire was burned during the first test at 31.2 T and the I_c and J_e values were also much lower than expected.

After checking the burnt wire, it was observed that the half-circle region of the wire was squashed flat by the large Lorentz force, as shown in Fig. 4-26. The lack of proper support made the outer layers of R2 vulnerable to the Lorentz force and the damaged structural integrity caused the burns.

The α values of STAR wires, except R2, which could not be calculated due to the single data point, ranged from 0.79 to 1.48. This value can be used to estimate the I_c at different fields by extrapolation. As an example, assuming no degradation happens, STAR wire 4 is predicted to have an I_c of 1477 A and a corresponding J_e of 658 A/mm^2 at 10 T. Compared to the REBCO tape, the α values of STAR wires R3 and R4, which did not degrade during the tests, are close to the tape α value of 0.76. The slight difference could be caused by a different α value along the tape length or a change in the field dependence of the critical current under the bending strain.

4.2.2.3 Analysis of degradation in high magnetic fields

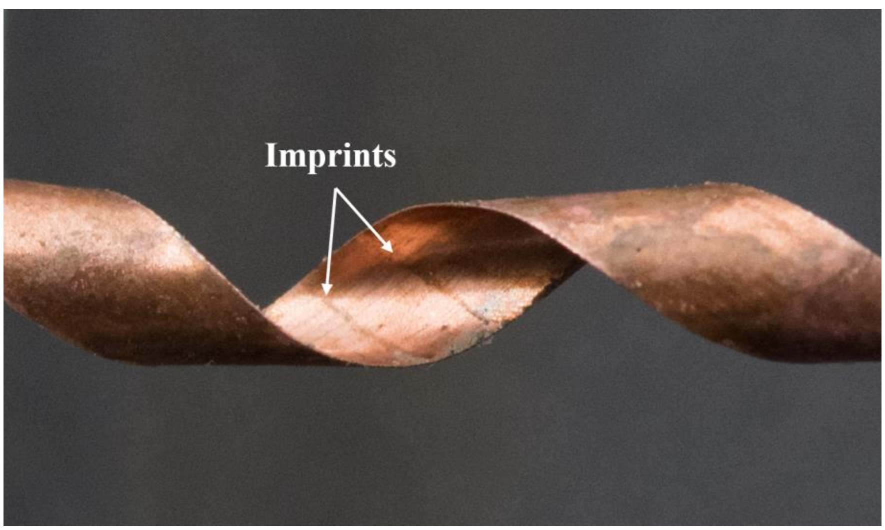

Fig. 4-27 Imprints found on the outmost layer of R1 after in-field tests

Without any impregnation, four out of five bare STAR wires burned or showed degradation during the tests. Therefore, STAR wire R1 was unwound after the in-field tests to check for any tape damage. Fig. 4-27 reveals the imprints found on the inner surface of the outmost layer of R1 [90], which were likely caused by the large Lorentz force. Since tapes with a fixed width of 2.5

mm were used for all layers, the gap between each turn increased as the number of layers increased. While the gradually increasing gap allows the tape to slide during bending, which can relieve the extra stress, it resulted in decreased support for the outer layers. In a high-field, high-current test, the Lorentz force might be large enough to press the outer layer inward, leaving imprints on the tapes or even squashing the wire into a flat shape.

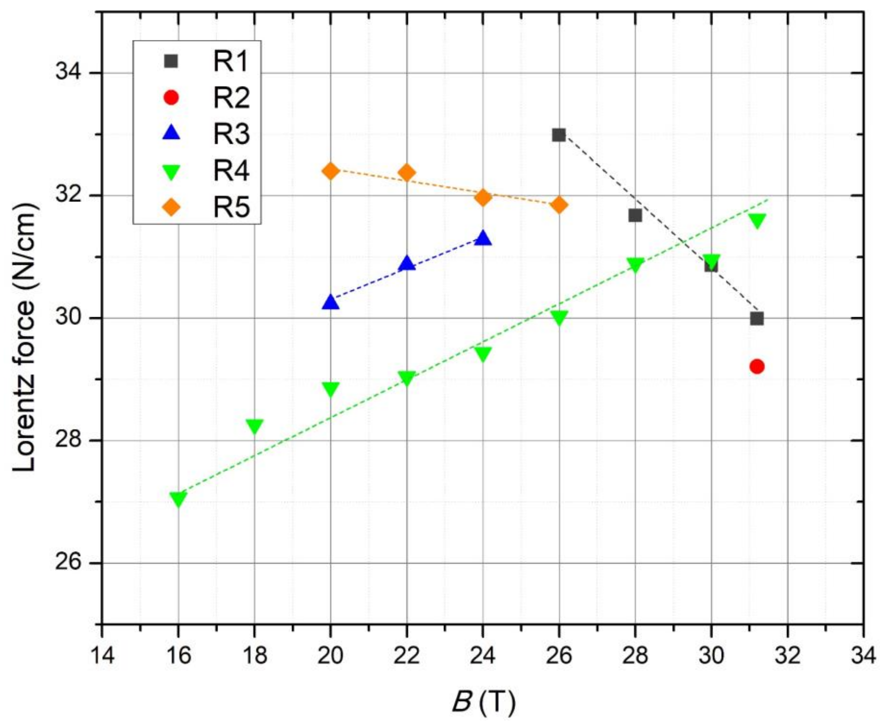

Fig. 4-28 Calculated maximum Lorentz forces applied on single layer of tape with 1 cm projection length

The maximum Lorentz force F applied on a layer in a certain magnetic field B can be expressed as

$$F = B \cdot I_c(B) \cdot L_{proj}, \tag{4-14}$$

where L_{proj} is the projection length of the tape perpendicular to the field. Assuming the current is uniformly distributed in each layer, the maximum forces applied on a single layer of tape with a 1 cm projection length are plotted in Fig. 4-28, where the dashed lines are linear fits of each sample's data. As can be observed, the Lorentz force on the tape is larger than 27 N/cm. For wires without degradation, such as R3 and R4, the Lorentz forces applied on each tape increased as the magnetic field increased, whereas the decreasing Lorentz forces of R1 and R5 were caused by the degradation of the I_c.

In general, the STAR wires without indium filling exhibited I_c and J_e values as high as 769 A and 274 A/mm^2 in magnetic fields up to 31.2 T. The lack of support of the outer layers, however, caused multiple performance degradations or even wire burns. A stronger mechanical structure is needed to improve the in-field performance of the STAR wire.

4.2.3 Performance of multi-layer STAR wires with indium filling

4.2.3.1 STAR wire specifications

Tab. 4-10 Specifications of STAR wires with indium filling

Wire No.	Former size	Wire O.D. (mm)	No. of layers	Tape width (mm)×No. of tapes	Total tape width (mm)
R6	18 AWG	1.96	8	2.5×8	20
R7		1.97	8	2.5×8	20
R8	20 AWG	1.78	8	2×2, 2.5×6	19
R9		1.75	8	2×2, 2.5×6	19
R10		1.98	9	2×2, 2.5×6, 2×2	23

To increase the mechanical strength of the STAR wire, indium was selected as the material to fill the gaps between tapes for the following reasons: it has good electrical conductivity, hence the advantage of current sharing between the layers of STAR wire is maintained and increased; the melting point of indium is 157°C, and therefore the filling process is performed at a temperature that does not degrade the REBCO layer; in addition, the wetting of copper to indium makes it easy to use indium to fill gaps and provide good support. The filling process is as follows: after bending a STAR wire into a 3 cm diameter, the exposed wire between terminals is treated with acid soldering flux and dipped in molten indium at 169 °C for a short time to allow the indium filling the gaps.

Another five STAR wires were fabricated to test the indium filling method; the specifications of the wires are listed in Tab. 4-10. In addition to the optimal tape width structure used in R6 and R7, the structure of substituting the 18 AWG former with a 20 AWG copper former wound with two layers of 2 mm wide tapes was used in R8 and R9 and the MTISL structure was used in R10, whereas the ninth layer contained two 2 mm tapes. It is worth noting that since the indium also covered the surface of the wires, the outer diameters were approximately 0.1 mm larger than the wire with the same structure but without indium filling. The parent 12 mm wide thin REBCO tapes used to produce the symmetric tapes were the same as described in section 4.2.2 except for a lower nominal I_c of 430 A.

Tab. 4-11 I_c, J_e values and retentions of STAR wires with indium filling at 77 K, self-field

Wire No.	Tape I_c sum.	Total tape width (mm)	Straight form			Bent form		
			I_c (A)	J_e (A/mm^2)	Retention-1 (%)	I_c (A)	J_e (A/mm^2)	Retention-2 (%)
R6	712	20	>600	>199	>84.3	610	202.3	N/A
R7	695	20	>600	>197	>86.3	556	182.5	N/A
R8	719	19	576	231	80.1	514	206.6	89.2
R9	724	19	570	237	78.7	494	205.5	86.6
R10	858	23	>600	>195	>69.9	548	178	N/A

At 77 K, self-field, the five STAR wires were first tested in the straight form without indium filling and then tested in the 3 cm bent form before and after the indium filling to make sure no degradation occurred during the filling process. The test results are listed in Tab. 4-11, where the

voltage criterion was 1 μV/cm. As can be observed, the wider total tape widths of STAR wires with indium filling compensated for the larger wire diameters and the lower current per unit width of the parent 12 mm tapes, resulting in comparable wire I_c and J_e values to those of STAR wires without indium filling.

4.2.3.2 Test results at 4.2 K in background magnetic fields

After the 77 K tests, the STAR wires with indium filling were tested in the same magnet in the NHMFL, which provided a background field up to 31.2 T at 4.2 K. The power sources were upgraded to provide a maximum current of 1350 A. In addition to the voltage reading, for R9 and R10, a cryogenic temperature sensor was installed to measure the temperature change during the test. The sensor was glued, by GE varnish, to the terminal end of R9 and the middle part of R10, as indicated in Fig. 4-29 [102].

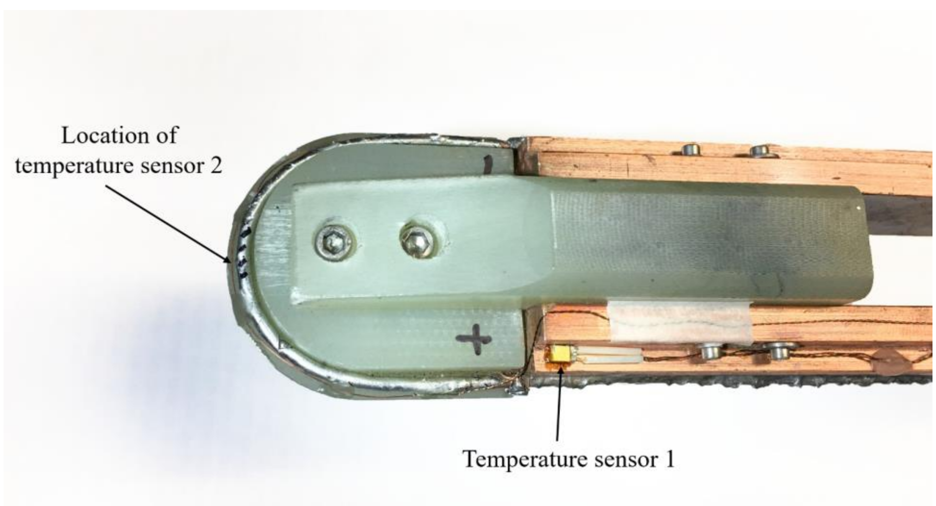

Fig. 4-29 Location of temperature sensors

The magnetic field dependences of the I_c and J_e values of R6 to R10 are plotted in Fig. 4-30 and Fig. 4-31, respectively. The data of R1, which had the best performance among the non-indium-filled STAR wires, are also plotted in the same figure for comparison. The α values of the five STAR wires with indium filling were between 0.61 and 0.87 and distributed in a smaller range than

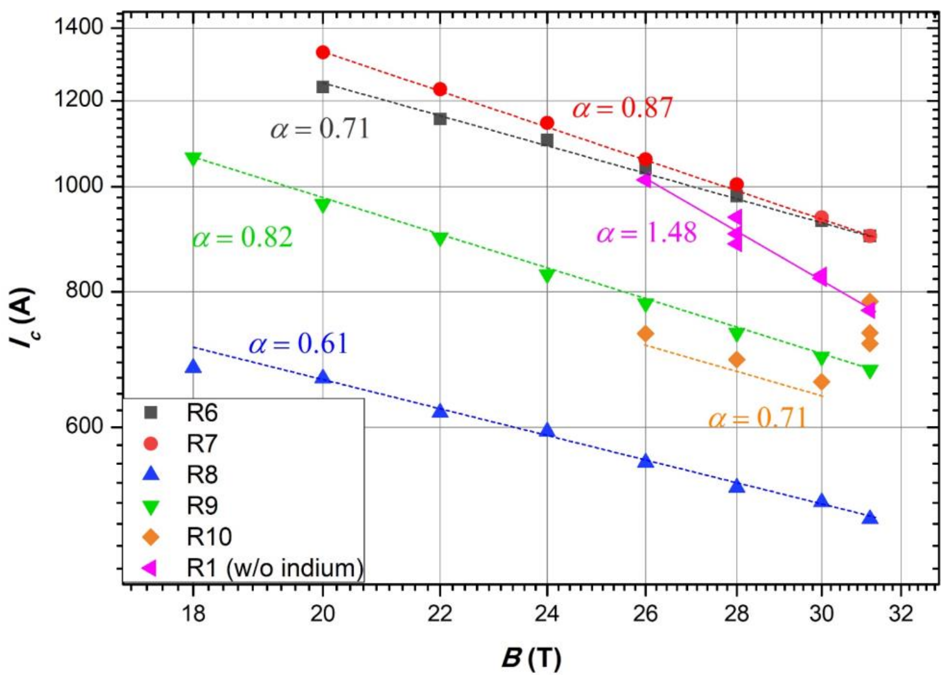

Fig. 4-30 Magnetic field dependence of I_c of STAR wires with indium filling between 18 and 31.2 T at 4.2 K

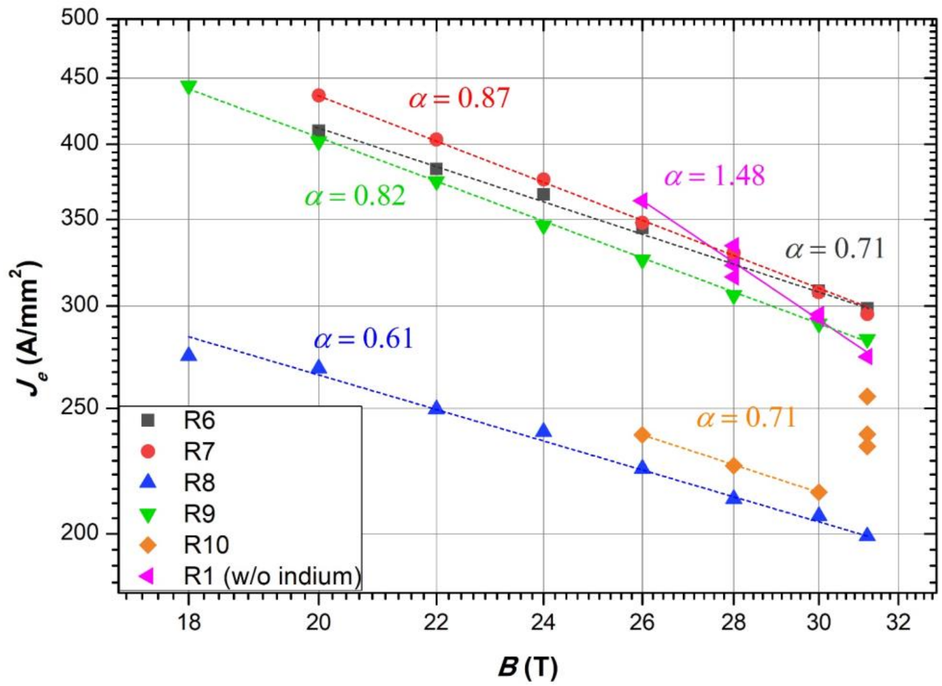

Fig. 4-31 Magnetic field dependence of J_e of STAR wires with indium filling between 18 and 31.2 T at 4.2 K

the wires without indium filling. As can be observed, the two STAR wires with optimal tape width structure, R6 and R7, had the best performance from 20 T to 31.2 T. At 31.2 T, both R6 and R7 reached an I_c of 901 A, with corresponding J_e values of 299 A/mm^2 and 296 A/mm^2, respectively. At 20 T, R6 carried an I_c of 1236 A with a J_e of 410 A/mm^2 and R7 carried a slightly higher I_c of 1330 A with a J_e of 436 A/mm^2. Because of the indium filling structure, no degradation was observed for these two wires and therefore the I_c-B curves fit well with straight lines. Compared to R1, the wire that had the same structure but no indium filling, the I_c and J_e values of R6 to R7 were 17% and 9% higher at 31.2 T, as a result of the stronger mechanical structure, in the high magnetic field.

For the 20 AWG wires R8, R9, and R10, the test results were not as good as those of the 18 AWG wires. Although no degradation was found, the 8-layer wire R8 had the lowest I_c and J_e values of all the tested samples. Examination after the tests found a kink on R8 near the copper terminals. It is believed that the Lorentz force applied on the sample caused a relative movement between the G10 mount and the copper terminal, thereby partially damaging the wire. R9 had the same structure as R8 and exhibited an I_c of 678 A and a J_e of 283 A/mm^2 at 31.2 T. Compared to R7, the I_c was about 33% lower and the J_e about 5% lower over the entire range. The smaller former did not increase the wire's performance at 4.2 K, which is consistent with the conclusion from the 77 K test results. R10 had the widest equivalent tape width of 23 mm; however, the initial degradation was observed in the 77 K bend test. In the 4.2 K test, further degradation happened at 31.2 T and 30 T. The disassembly of R10 after the test found that the tight tape arrangement prevented the indium from filling all the gaps, resulting in a weak structure. In addition, STAR wires with more tapes, like R10, are expected to have better performance with longer terminals since increased contact area is needed for the increased number of tapes.

4.2.3.3 Repeatability test and temperature changes of STAR wires

In order to be used in magnets, repeatable performance is expected from STAR wires. A repeatability test was performed on R7, which had the highest performance of all the tested wires. The critical current of R7 was reached eight times at 31.2 T, and the magnetic field was lowered to 18 T between each test. The results are shown in Fig. 4-32 [90] and the critical current values obtained in all tests were within a 1% variation, showing the repeatability and mechanical robustness of STAR wire with the indium-filled structure.

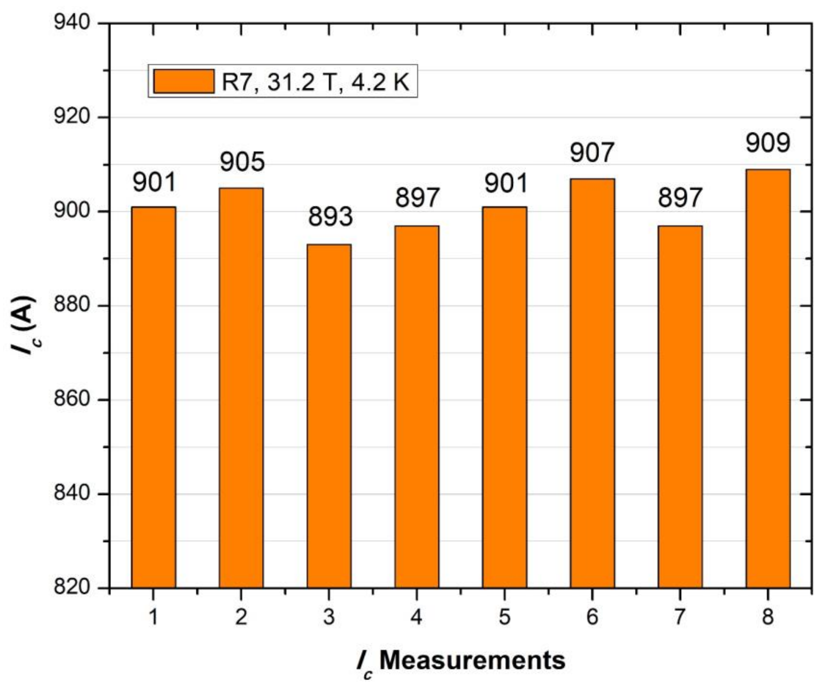

Fig. 4-32 Repeatability test of R7 at 31.2 T background field

Fig. 4-33 shows a plot of temperature *T* versus time *t* during the 4.2-K tests [102]. A temperature sensor was installed on the copper terminal of R9 and in the center part of R10, as demonstrated in Fig. 4-29. For R9, the temperature curve corresponds to tests between 24 T and 31.2 T. Because of the low terminal resistance, the temperature rise in the copper terminal was less than 0.5 K. For R10, the temperature curve corresponds to tests between 26 T and 31.2 T. Since R5 was partially damaged, multiple temperature increases, with a maximum value of 3 K, can be observed. The generated heat raised the temperature of the whole wire and, in turn, degraded the wire's performance. However, the low temperature between each test proved the efficacy of cooling in the pulse current mode.

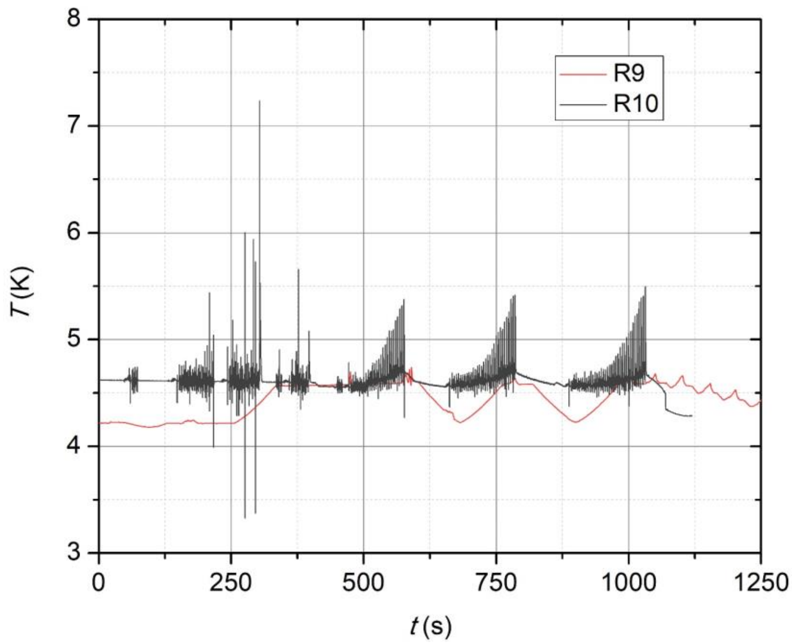

Fig. 4-33 Temperature change of R9 and R10; sensor was installed on the copper terminal of R9 and in the center part of R10

4.2.3.4 Summary

In this section, the in-field performance of STAR wires was discussed. Single-layer STAR wires and multiple-layer STAR wires with different structures were tested in background fields. Based on the test results, the following conclusions can be made:

1) Single-layer STAR wire exhibits an angular dependence of around 10% at both 77 K and 30 K, which is much smaller than that of the flat REBCO tapes.
2) Because of the spiral shape of the tapes in a STAR wire, the in-field performance of the STAR wire is limited by the point where the magnetic field is perpendicular to the tape surface (B ∥ c).

3) Without any reinforcement, the gaps in STAR wire make it vulnerable and easily damaged in high magnetic field tests; the highest I_c and J_e values achieved at 31.2 T were 769 A and 274 A/mm^2, respectively.

4) Indium is a good material to fill the gaps in STAR wire; such filling can increase the wire's mechanical strength in high magnetic field tests. With the help of indium filling, the highest I_c and J_e values achieved at 31.2 T were 901 A and 299 A/mm^2, respectively.

5) STAR wires with the optimal tape width structure exhibit better in-field performance than other structures, which is consistent with the 77 K test results.

4.3 Resistance and defect detection of STAR wires

This section discusses the resistance, including the terminal resistance and interlayer resistance, of STAR wire and several attempts to detect defects in STAR wire. The influence of the terminal resistance and measured data are analyzed in the beginning. Afterwards, the inter-layer resistance of STAR wires with different structures, such as wires with and without indium filling, are compared. Several attempts to locate defects in a STAR wire, including section-by-section *I-V* measurement and magnetic bridging, are discussed at the end.

4.3.1 Terminal resistance of STAR wires

The terminal plays an important role in the performance of STAR wires. Current is distributed into each layer of a STAR wire through its terminal and the contact resistance between the terminal and REBCO tapes affects the initial distribution. If one layer of the tape has a lower I_c than others, then when the current in this layer reaches the I_c value, it is transferred into other layers via the terminal or the interlayer contact; thus a lower terminal resistance is beneficial. In addition, in large-current situations, the temperature increase in the terminal also affect the performance of STAR wires; thus a low terminal resistance is favorable.

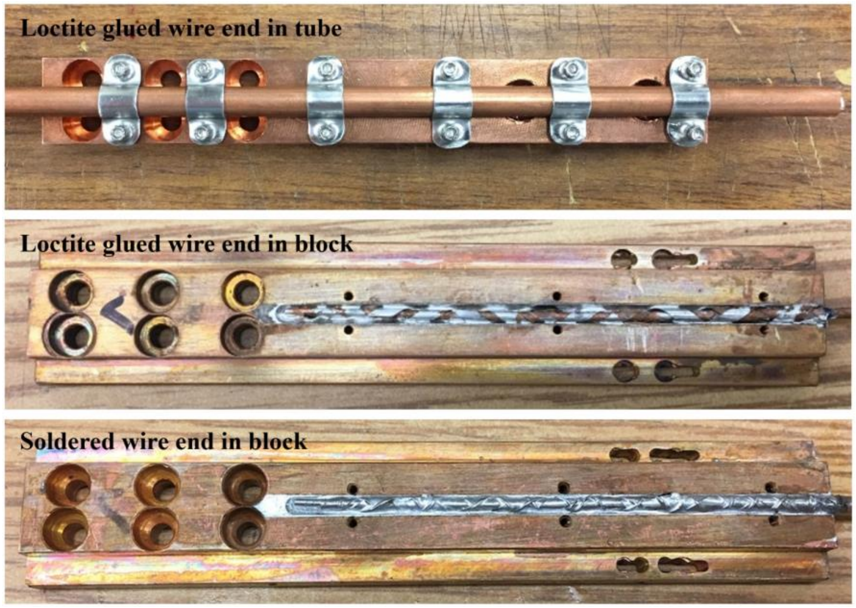

Fig. 4-34 Three different terminal structures measured in resistance tests

The resistance of three different terminal structures, as shown in Fig. 4-34, were measured. The wire ends of the first two structures were glued using Loctite 404, which was discussed in section 2.4.2.2, and then soldered with 60/40 tin lead alloy in a copper tube or a copper block. Since the cured Loctite 404 formed insulation layers between the tapes, current was shared via copper tube or block between tapes. These two structures were adopted in the early development of machine-wound STAR wires. The third structure had a soldered wire end and tin lead alloy filled all the gaps between the copper block and the tapes. This structure was used in later-developed STAR wires, including the 10 m long wire and the wires tested in magnetic fields.

Fig. 4-35 is a schematic diagram of the current distribution in a STAR wire, where only three layers are shown for simplification. Current flows into the copper terminal and is distributed into three layers, L1, L2, and L3, through the solder. R_{1t}, R_{2t}, and R_{3t} are the contact resistances between the copper terminal and the three layers, respectively, and R_t is the copper terminal resistance. For terminals made from oxygen-free copper, the R_t at 77 K is one to two magnitudes smaller than R_{1t}

and is negligible. In the first two terminal structures, because of the insulation between each layer, the layers are in a parallel connection and the terminal resistance R can be simply expressed as

$$\frac{1}{R} = \frac{1}{R_{1t}} + \frac{1}{R_{2t}} + \frac{1}{R_{3t}}. \tag{4-15}$$

Therefore, direct measurements can be performed on the first two terminal structures.

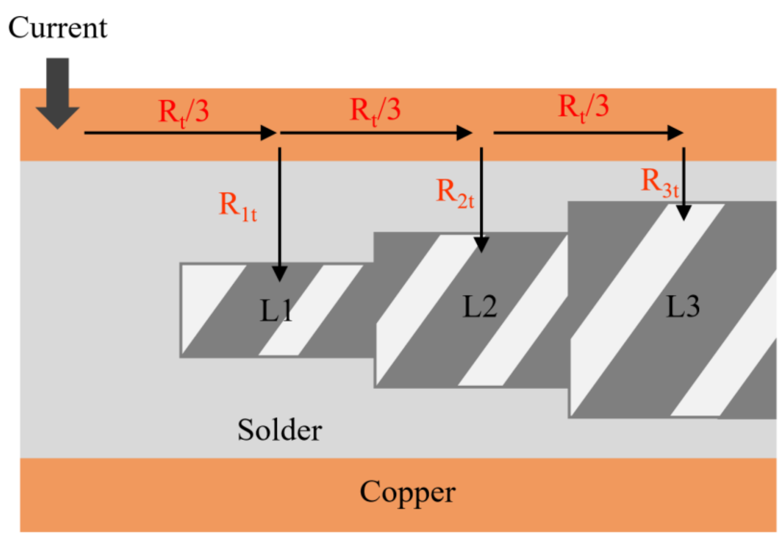

Fig. 4-35 Schematic diagram of current distribution in a 3-layer STAR wire, not to scale

Fig. 4-36 Unwound STAR wire for direct measurement of the terminal resistance

A 6-layer STAR wire soldered with the first terminal structure, the Loctite-glued wire end in tube, was cut and unwound carefully to expose each layer, as shown in Fig. 4-36. Afterward, a Keithley 2400 Sourcemeter was used to provide current and measure the voltage on the six tapes in pairs by using a standard 4-point method at 77 K. For each test, the wire was excited by currents of ±10 mA, ±100 mA, or ±1 A, where the change of current polarity was used to compensate for the thermoelectric effect.

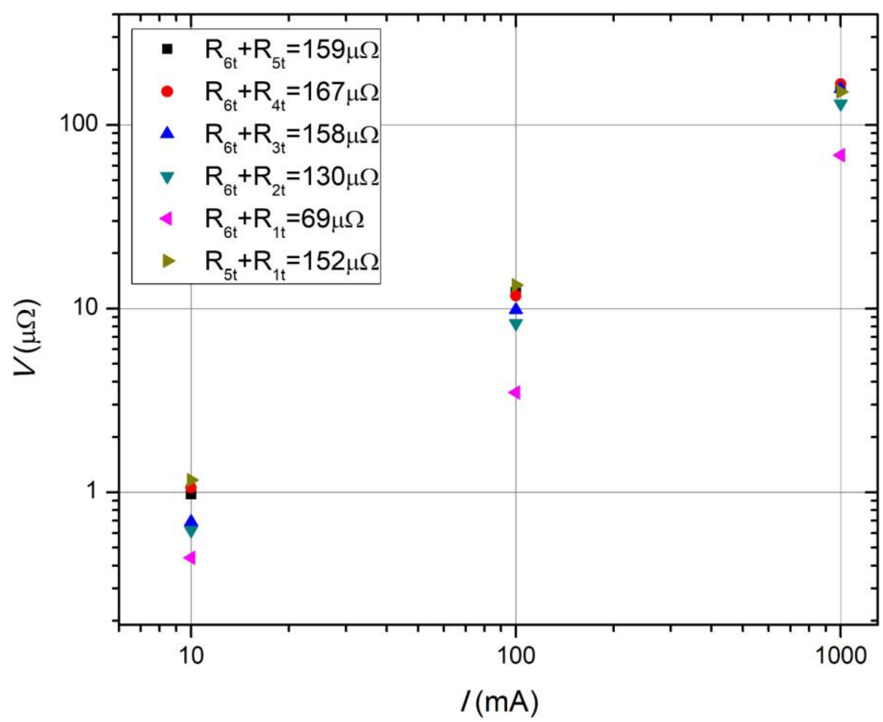

Fig. 4-37 Resistance between pairs of tape in a STAR wire with tube terminal

The results are plotted in Fig. 4-37 and linear fittings were used to determine the resistance of pairs of tape. Based on the test results, $R_{1t} = 31\mu\Omega$, $R_{2t} = 92\mu\Omega$, $R_{3t} = 120\mu\Omega$, $R_{4t} = 129\mu\Omega$, $R_{5t} = 121\mu\Omega$, $R_{6t} = 38\mu\Omega$, and the total terminal resistance R is 10.7 μΩ. As can be observed, the contact resistances between each layer of tape and the copper terminal are not uniform and the total terminal resistance is at a magnitude of 10 μΩ. This is caused by the tube structure of the terminal, which makes solder filling in the tube unobservable and uncontrollable. The same test was performed on a STAR wire with the second terminal structure, the Loctite-glued wire end in block. With better control over the solder filling process, the terminal resistance was decreased to a much lower value of 2.8 μΩ at 77 K.

For the third terminal structure, since the solder fills the gap between each layer, current was shared between layers via either the copper terminal or the solder between layers. Therefore, the terminal resistance cannot be simply expressed by Eq. 4-15 and the result of the same test was the interlayer resistance in the terminal, rather than the contact resistance between the tape and the terminal. To get the real terminal resistance, the non-linear fitting expressed in Eq. 4-1 was used.

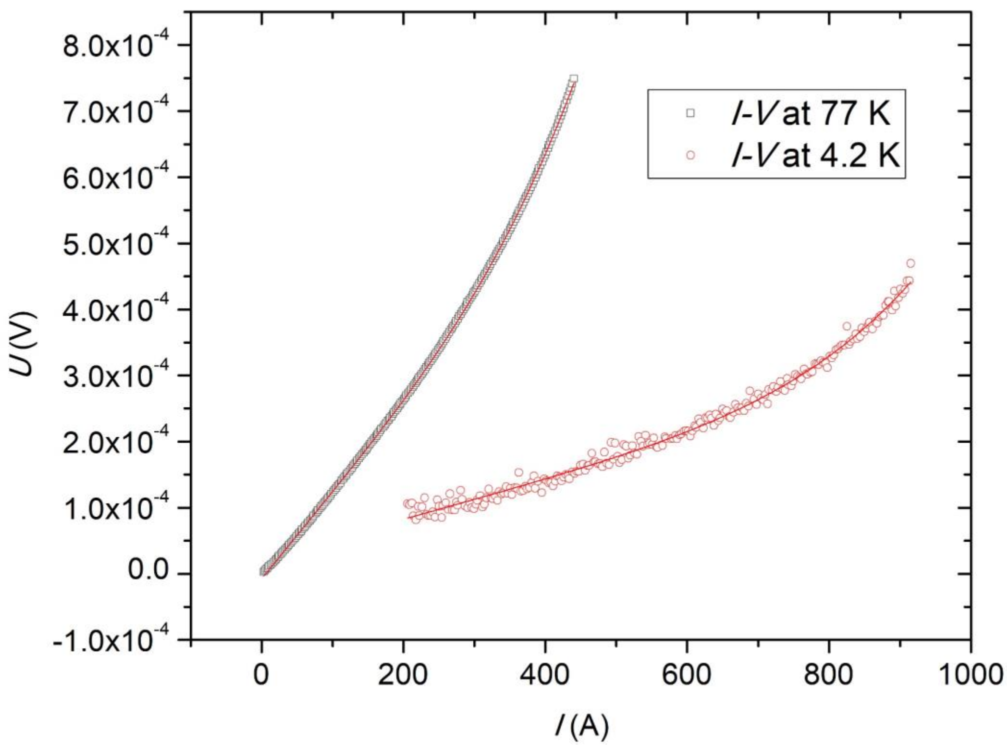

Fig. 4-38 *I-V* characteristics of a STAR wire used to determine terminal resistance

Fig. 4-38 shows the *I-V* curves of R2 discussed in section 4.2.2, where the voltage was read from the copper terminal so that both the terminal resistance and the superconducting transition were measured [102]. The solid lines in the plot are the non-linear fittings of the data. The calculated terminal resistance at 77 K was 1.31 μΩ for both terminals. At 4.2 K, 20T, the terminal resistance dropped to 300 nΩ due to the lower copper resistance. The single terminal resistance of 655 nΩ at 77 K is one magnitude smaller than that of the second terminal structure, proving that a good electrical contact was achieved in the third terminal structure.

4.3.2 Inter-layer resistance of STAR wires

When fabricating long STAR wires, it is difficult to guarantee that all the symmetric tapes are free from defects. In addition, from the results of the 10 m long STAR wire experiments in section 4.1.5, a certain extent of current sharing between the tapes was observed. Therefore, it is necessary to investigate the interlayer resistance and current sharing ability of STAR wires.

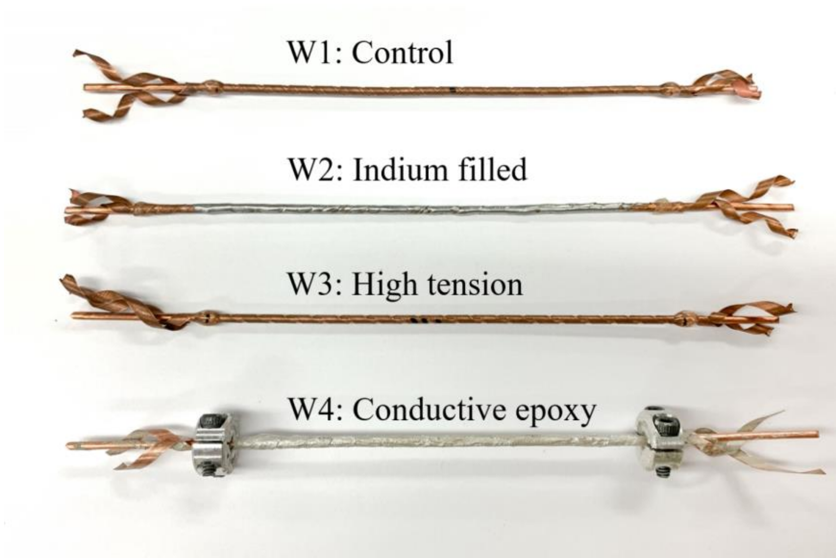

Fig. 4-39 Four STAR wires used for interlayer resistance test

Four STAR wires with different structures were fabricated, as shown in Fig. 4-39. To unwind tapes easily after winding, 14 AWG copper rods were used as formers. Two layers of 2.5 mm symmetric tape were wound in a crisscross structure and the total wire lengths were 10 cm for W1 to W3, and 9 cm for W4. W1 was the control sample, which used standard winding parameters; W2 was filled with indium after winding; W3 used a two-fold higher winding tension than W1, so that the electrical contact between tapes was better; and W4 was wet-wound with conductive epoxy and then cured after winding. The resistivity of the conductive epoxy is 3.1×10^{-4} Ω·cm at room temperature.

Tab. 4-12 Results of interlayer resistance measurements

Sample	Measured Resistance (μΩ)			Contact area (cm^2)	Interlayer resistance R (μΩ·cm^2)	Length for sharing 50 A of current (cm)
	R_{12}	R_{21}	R_{avg}			
W1	35	44	39.5	2.13	84.1	131
W2	21	17	19	2.13	40.5	92
W3	34	31	32.5	2.13	69.2	119
W4	14	20	17	1.88	32.0	81

After winding, the wires were unwound at two ends to expose each layer, as demonstrated in Fig. 4-39. Similar to the terminal resistance test, a Keithley 2400 Sourcemeter was used to provide the current and measure the voltage by the four-point method. The resistance between the left end of the first layer and the right end of the second layer is resistance R_{12} and the resistance between the right end of the first layer and the left end of the second layer is resistance R_{21}. The final resistance R_{avg} is the average of R_{12} and R_{21}, and the interlayer resistance R is R_{avg} times the contact area. Both the change of current polarity and the change of left and right ends were conducted to compensate for the thermoelectric effect.

The test results are shown in Tab. 4-12. As can be seen from the table, the R_{avg} of the control wire W1, which was 39.5 μΩ in a 10 cm length, is the largest among the four wires. Because of the surface roughness of the tape, only a small fraction of the surface area, the asperity spots, had good electrical contact [103]. With a higher applied winding tension, the number of asperity spots increased and the R_{avg} of W3 decreased accordingly. With conductive material filling the space between layers, such as the indium in W2 and the conductive epoxy in W4, the R_{avg} was reduced even further. Since the conductive epoxy was applied during winding, the filling rate was much better than that of the indium filling after winding, which is why the R_{avg} of W4 is still lower than the R_{avg} of W2 despite the higher resistance of the filling material used in W4.

At a winding angle of 45 degrees, the contact area A_{cont} between two tapes in a given length L is expressed as

$$A_{cont} = nw^2 = 2\frac{L}{\pi d}w^2, \tag{4-16}$$

where n is the number of areas where tapes overlap, w is the tape width, and d is the outer diameter of that layer. The contact area of each wire is also listed in Tab. 4-12. Therefore, the interlayer resistance R can be calculated accordingly and W4 has the lowest R of 32.0 $\mu\Omega\cdot cm^2$. As a comparison, typical REBCO-to-REBCO soldered joints have R values at the magnitude of 0.01 $\mu\Omega\cdot cm^2$ [104, 105], and REBCO-to-substrate pressed joints under 144 MPa pressure have R values between 20 and 100 $\mu\Omega\cdot cm^2$ [103].

When current is shared between tapes, the voltage U induced by the interlayer resistance can be expressed as

$$U = I_{Shr}\frac{R}{A_{cont}}, \tag{4-17}$$

where I_{Shr} is the current shared between tapes. In terms of the electric field E, the voltage is given by

$$U = E \cdot L. \tag{4-18}$$

Equaling Eq. (4-17) and Eq. (4-18) yields

$$L = \sqrt{\frac{I_{Shr}R\pi d}{2Ew^2}}. \tag{4-19}$$

Using 1 μV/cm as the electric field limit, to share 50% of the original tape current of 100 A, the length required for current sharing is listed in the last column of Tab. 4-12. For different STAR wire structures, lengths of 81 cm to 131 cm are required to share 50 A between two tapes. It is worth noting that for multi-layer STAR wires, except for the first and last layers, tapes in the middle layer contact the inner and outer layers at the same time; therefore, the length required for current sharing is reduced by a factor of $\sqrt{2}$.

4.3.3 STAR wire defect test

Because of the winding tension and bending stress, defects may be induced into STAR wires during the winding process; mechanical damage also may happen in a certain layer of the STAR wire after tests in high magnetic fields. Unlike REBCO tapes, where trapped magnetic field mapping, such as TapeStar and SHPM, can be used to locate defects, the three-dimensional structure of STAR wire makes detecting defects by this method very difficult as the signal-to-noise ratio of the magnetic field decreases substantially with increasing detection distance. To locate the damaged area in a STAR wire, several other non-destructive methods were tested.

4.3.3.1 Section-by-section *I-V* method

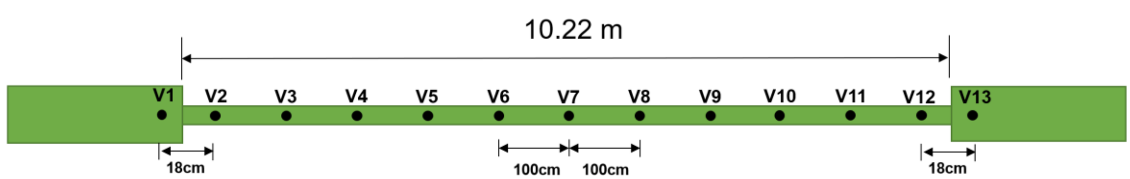

Fig. 4-40 Schematic diagram of locations of voltage tap on 10 m STAR wire

The most straightforward method is to measure the *I-V* characteristics of a long STAR wire section by section. Because of the multi-layer structure of STAR wire, the voltage increase of the inner layer is difficult to measure from outside in a short wire length. As discussed in the previous section, a typical length of 1 m is needed for a 100 A tape to transfer 50% of its current into other layers. Therefore, a section-by-section *I-V* test with 1 m intervals was performed on the 10 m STAR wire which was discussed in section 4.1.5.

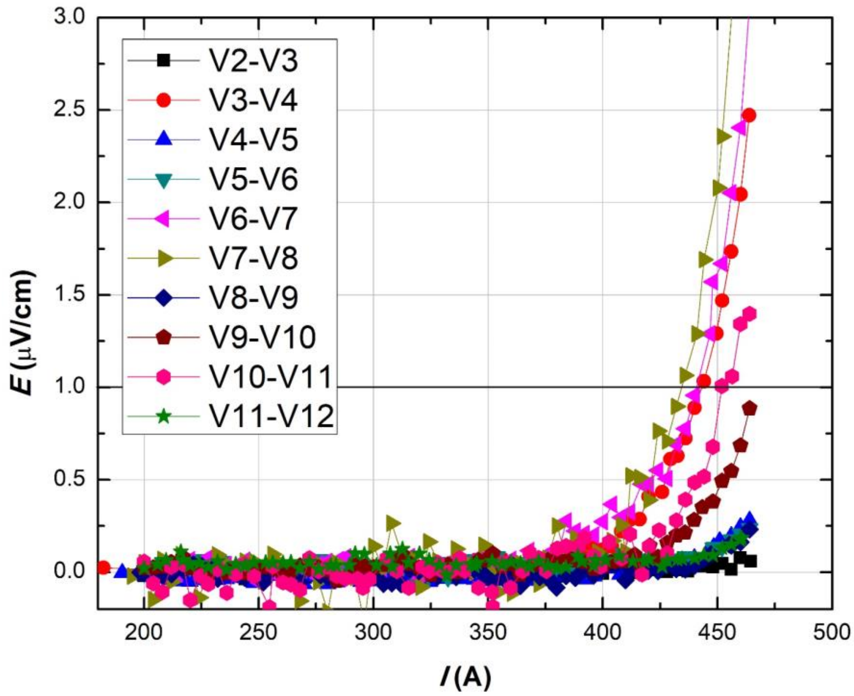

Fig. 4-41 Section-by-section *I-V* characteristics of 10 m STAR wire

Fig. 4-40 is a schematic diagram of the locations of 13 voltage taps on the 10 m STAR wire. The voltage tap pairs V1-V13 and V2-V12 were used to define the I_c of wire, which were 467 A and 476 A, respectively. The *V-I* curves between voltage tap pairs in the middle, such as V2-V3, V3-V4, and so on, are plotted in Fig. 4-41. To protect the wire from over-current damage, the maximum current was limited to the wire's I_c of 467 A. As can be seen, with a 1 μV/cm criterion, four sections reached their I_c values and the other six sections did not reach the transition. The section I_c values are plotted in Fig. 4-42. In other words, with the same current, the induced voltage in each section is not the same, which indicates that the section with a higher voltage contains more defects than the section with a lower voltage. However, if a defect is located on a tape of the inner layer, since the voltage increase of that tape can only be measured in a relatively long wire length, the accuracy of the defect location by using the section-by-section method is limited to the order of meters for STAR wires.

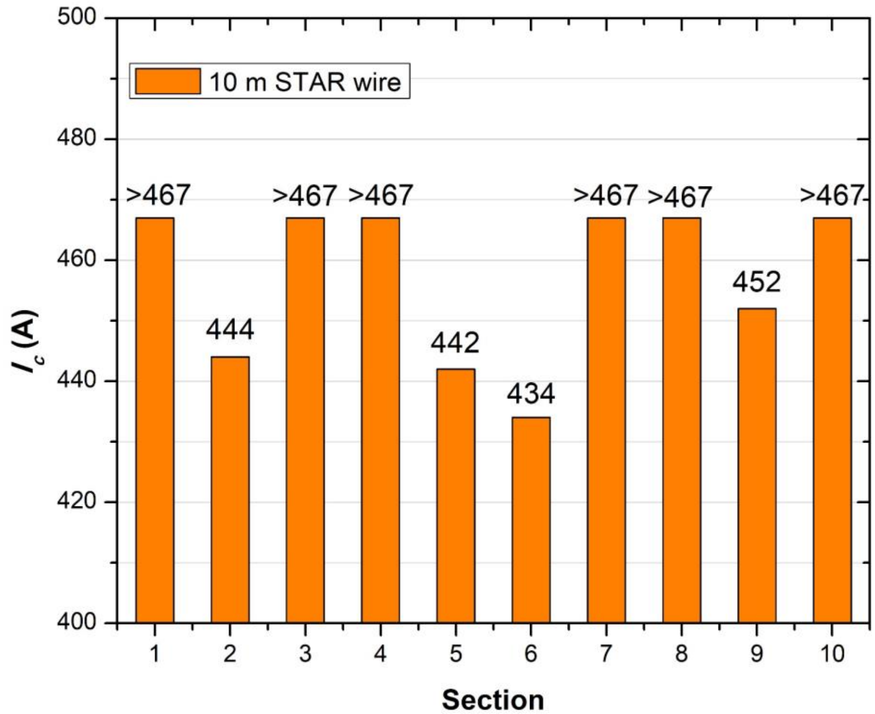

Fig. 4-42 Section I_c of the 10 m STAR wire

4.3.3.2 Magnetic bridging method

To precisely locate a defect in STAR wire, an I_c measurement method in local magnetic fields, which is called magnetic bridging, was proposed. The initial idea is that the local I_c of a STAR wire is reduced, or bridged, in a local magnetic field; by adjusting the location of the magnetic field, the section with defects can be filtered out.

As an example, a 7 cm long STAR wire has an I_c of 100 A at locations without defects, whereas the defects at 2 cm and 4 cm reduce the local I_c to 70 A and 80 A, respectively; the local I_c curve of the wire in self-field is shown as the black line in Fig. 4-43. In a magnetic field, the local I_c of the wire is reduced to 80% of the original value at every location, which is shown as the red line in Fig. 4-43. When a localized magnetic field moves along the wire, at a location without a defect, the wire's I_c is limited by the local I_c of the defect at 2 cm, which is 70 A; however, when the localized magnetic field overlaps with the defect at 2 cm, the wire's I_c drops to 56 A since the local I_c of the defect at 2 cm is 56 A in the magnetic field. Therefore, after 7 tests, a curve of the wire's I_c versus magnetic field location is obtained, which is shown as the blue line in Fig. 4-43. By analyzing this curve, the locations of defects can be determined.

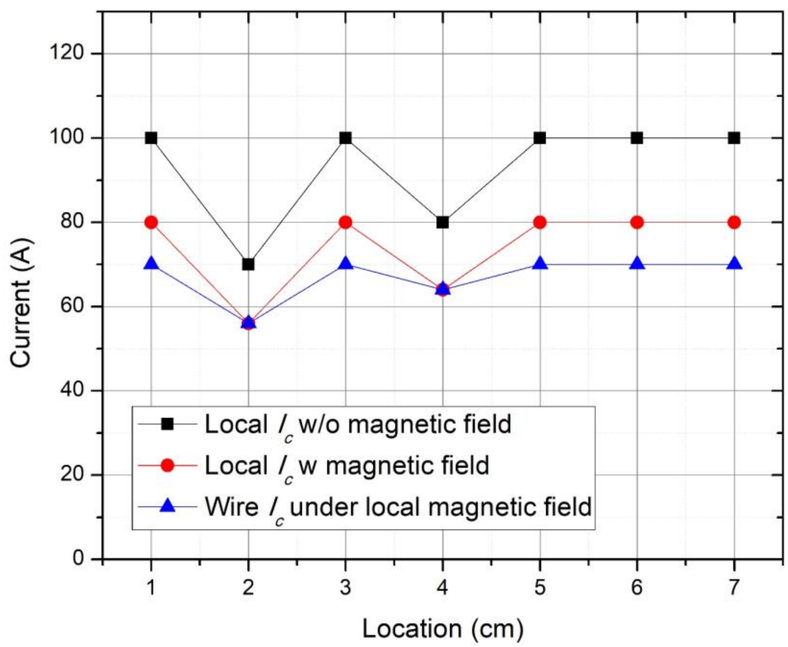

Fig. 4-43 Schematic plot of magnetic bridging method

To verify this method, a preliminary test was performed. A single-layer, 5 cm long STAR wire, with an artificial defect at 3 cm, was made. The flat tape I_c was 108 A without defects and 68 A with the artificial defect. Winding from the tape with the defect, the STAR wire had an I_c of 64 A, which corresponded to a 94% retention rate. Therefore, assuming the retention rate is the same along the wire, the local I_c of STAR wire at locations without any defects was 102 A. A NdFeB permanent magnet installed on an iron core with a 4 mm air gap was used to create the localized magnetic field. The magnetic field was 1 cm wide and the field strength was 0.7 T in the air gaps. The experimental setup is shown in Fig. 4-44, where the magnet moved along the wire 5 times at

1 cm intervals. It is worth noting that the defect was carefully placed in the location where the magnetic field was perpendicular to the tape surface since the in-field performance of STAR wire was also limited by the tape at that point.

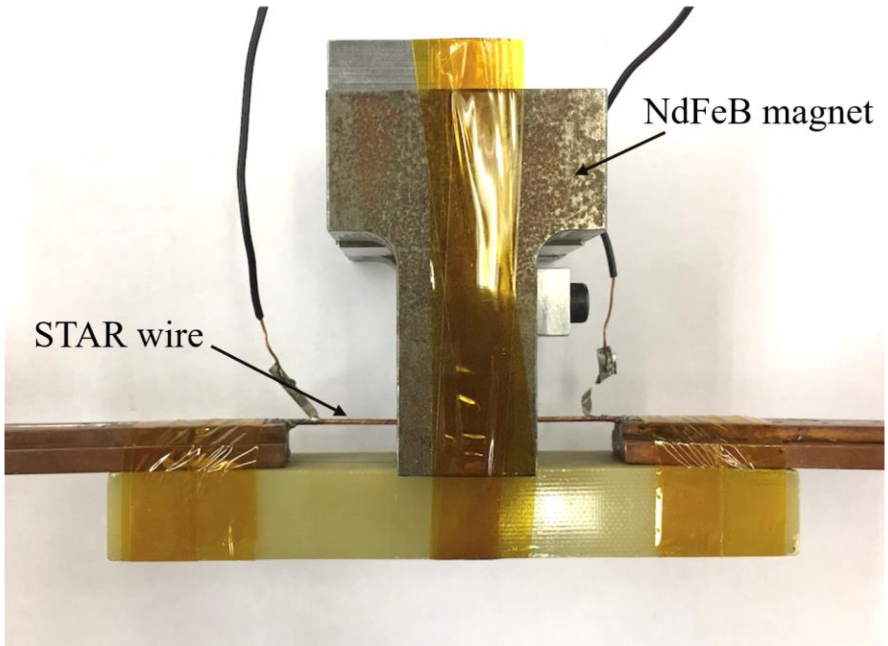

Fig. 4-44 Magnetic bridging measurement on a STAR wire

The estimated local I_c without a magnetic field and the measured local I_c under a magnetic field are shown in Fig. 4-45. As can be seen, with the localized magnetic field, the section of STAR wire with the defect has a significantly lower local I_c than other sections, whereas the sections without a defect show uniform local I_c values. The I_c drops at the defect are 37% without a magnetic field and 28% with a magnetic field, which indicate that the electrical behavior of the defect region under a magnetic field is slightly different from the normal region.

The preliminary experiment proves the possibility of using the magnetic bridging method to detect defects in STAR wire at a much higher accuracy. However, several challenges need to be solved before the technique is ready for practical usage. For a real STAR wire with defects, the number of defects and their local I_c drops are unknown; therefore, choosing a suitable magnetic field strength is critical since a too-weak magnetic field cannot expose small defects, whereas a too-strong magnetic field will reduce the I_c difference between the normal region and the defect region. In addition, because of current sharing in long STAR wires, the influence of shared current on magnetic bridging also needs to be investigated.

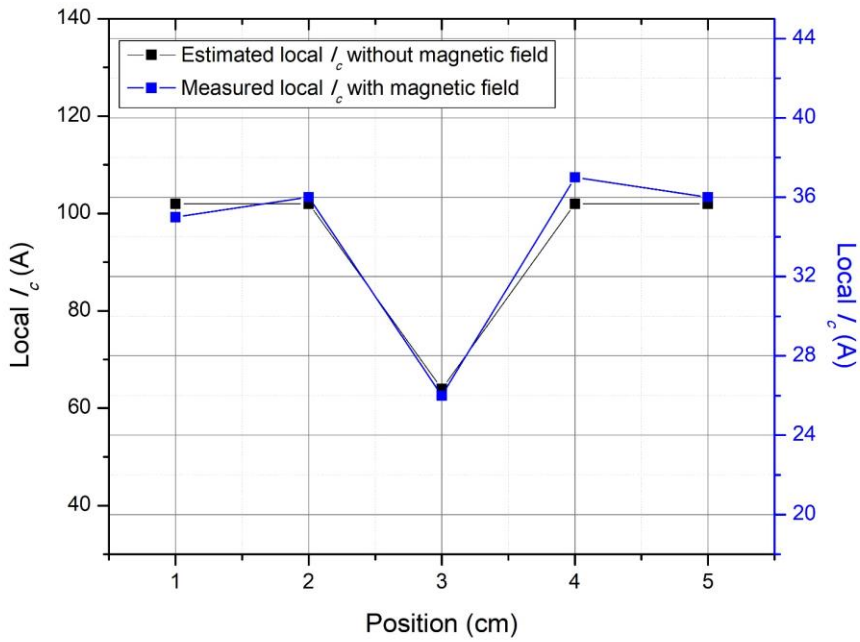

Fig. 4-45 Comparison of estimated I_c and measured I_c under magnetic bridging

Chapter 5. Conclusions and future works

5.1 Conclusions

A full fabrication process of symmetric tape round (STAR) REBCO wires, including ultra-thin REBCO tape processing and cable winding, has been established. The influence of the substrate thickness, copper thickness, and twist pitch on the electromechanical properties of symmetric tape was investigated. On this basis, STAR wires with different structures were fabricated and tested. The straight and bending performances of STAR wires at 77 K in self-field and 4.2 K in background fields were analyzed in detail. In addition, the resistance of and defect detection in STAR wires were studied.

Mechanical dry grinding is an effective way to reduce the thickness of REBCO tapes. By using a multi-wheel grinding system, the thickness of tape can be reduced to 20 μm with less than 10% I_c degradation. The pulse width and Q frequency of the laser affect the tape slitting quality. After optimizing the laser parameters, an average roughness of 7 μm and less than 3 μm of burnt area at the tape edge were achieved. A single-side electroplating shield was designed and proven to be effective in controlling the current distribution uniformity. After single-side electroplating, the average tape edge roughness was less than 10 μm. Based on experience with manual winding, an automatic cable winding system was established. Multiple winding parameters, including the tape width, number of layers, winding tension and angle, etc., can be precisely controlled. STAR wires with different parameters were fabricated.

The distance between the REBCO layer and tape neutral axis is the key factor that influences the tape bending properties. By reducing the thickness of Hastelloy substrate and then electroplating a copper stabilizer onto the REBCO side, the neutral axis is moved close to the REBCO layer. Tapes with such a structure are called symmetric tapes. With 20 μm thick substrate and 22 μm thick copper layer on the REBCO side, a symmetric tape maintained 97% of the original

I_c at a 0.8 mm bending diameter under compressive strain. Bending test under tensile strain yielded comparable results at the same bending diameter. To optimize the bending properties of ultra-thin REBCO tapes, optimal copper thicknesses for different tape thicknesses were determined. After copper thickness optimization, the tapes with thicknesses less than 25 μm maintained at least 80% of the original I_c at a 0.8-mm bending diameter. The thinner the tape, the higher the I_c retention. It was also observed that tapes wound at a twist angle of 45° had the best I_c retention.

Studies of STAR wires with different structures revealed that these wire structures are suitable for different applications. The variable tape width structure is suitable for use in the straight form or under large bending diameters; as the bending diameter decreases, the tape width should be narrowed to maintain a good bending performance. The MTISL structure increases the filling rate while maintaining the bending performance, but STAR wires with large diameters are preferred due to the difficulties in winding. At a 3 cm bending diameter, the optimal wire structure is 6 to 8 layers of 2.5 mm wide tape on an 18 AWG former. In short samples (9 cm), at 77 K in self-field, the highest achieved I_c and J_e values were >610 A and 237 A/mm^2 in the straight form and 611 A and 218 A/mm^2 in the 3 cm diameter bent form, respectively. In the long wire (10 m), an I_c of 465 A and a J_e of 165 A/mm^2 were achieved in a solenoid form at 77 K.

At 77 K and 30 K, a single-layer STAR wire exhibited a 10% variation in the angular dependence of I_c. At 4.2 K in a 31.2 T background field, STAR wires without any impregnation carried the highest I_c and J_e values of 769 A and 274 A/mm^2, respectively. However, multiple degradations indicated that the gaps between tapes negatively affected the wires' mechanical strength; the indium filling method after cabling was adopted to address this issue. With the help of indium filling, at 4.2 K in a 31.2 T background field, the I_c and J_e values were improved to 901 A and 299 A/mm^2, respectively.

To reduce the resistance of the STAR wire terminal, several terminal structures were designed and tested. It was observed that the wire end soldered inside a larger copper block exhibited the lowest resistance, which was 655 nΩ at 77 K. The interlayer resistance of STAR wires was also investigated. A larger winding tension and conductive filling materials reduced the contact resistance between the layers effectively, which was helpful for sharing current. With a better filling rate, the conductive epoxy-filled STAR wire had an interlayer resistance of 32 $\mu\Omega\cdot cm^2$, which made it able to transfer 50 A of current between two layers in a length of 81 cm. To detect defects in a STAR wire, section-by-section *I-V* measurement was a simple way to roughly locate weak regions in long wires. The magnetic bridging method showed potential for use in precisely positioning defects.

5.2 Future work

The ultimate goal of this research is to develop and fabricate high-performance, long-length STAR wires at a large scale. Based on the findings described in this dissertation, the following future works are recommended:

Improve the grinding uniformity and quality. With the current grinding setup, the thickness difference between the middle point and the edge of the tape is difficult to eliminate. This issue makes getting a thinner tape difficult since the tape edge becomes too thin and fragile, whereas the middle section is still relatively thick. Improving the grinding quality is also important as any severe weak sections in the middle of a tape reduces the usability of the entire tape.

Improve the current-sharing ability and filling technique. Since fabricating long STAR wires will become more and more important in the future, the current-sharing ability in long STAR wires needs more investigation. The current indium filling technique is suitable for short wires with a few layers, but it is difficult to use the same technique for long STAR wires. A new method that can improve the current-sharing ability and mechanical strength at the same time is preferred.

With a better filling method, increasing the number of layers in STAR wires is also recommended. To use STAR wires in compact accelerator winding, a higher critical current is also required; the simple way to solve this issue is to wind more layers and use the MTISL wire structure. Another possible method is to incorporate the thick-film REBCO tapes fabricated at UH, which can substantially increase the current-carrying ability of STAR wire.

The defect detection methods for STAR wire are still at a preliminary stage. To industrialize STAR wire, it is necessary to locate regions with inferior performance. Therefore, further study on this topic is necessary.

References

[1] H. K. Onnes, "Further experiments with liquid helium," in *Proceedings of the KNAW*, 1911, vol. 13, pp. 1910-1911.

[2] W. Meissner and R. Ochsenfeld, "Ein neuer effekt bei eintritt der supraleitfähigkeit," *Naturwissenschaften,* vol. 21, no. 44, pp. 787-788, 1933.

[3] B. Seeber, Handbook of applied superconductivity. Institute of Physics Pub, 1998.

[4] C. Walters, "Design of multistrand conductors for superconducting magnet windings," 1974.

[5] H. S. Edelman and D. C. Larbalestier, "Resistive transitions and the origin of the n value in superconductors with a Gaussian critical-current distribution," *Journal of applied physics,* vol. 74, no. 5, pp. 3312-3315, 1993.

[6] M. Lubell, "Empirical scaling formulas for critical current and critical field for commercial NbTi," *IEEE Transactions on magnetics,* vol. 19, no. 3, pp. 754-757, 1983.

[7] J. E. Kunzler, E. Buehler, F. a. Hsu, and J. H. Wernick, "Superconductivity in Nb 3 Sn at high current density in a magnetic field of 88 kgauss," *Physical review letters,* vol. 6, no. 3, p. 89, 1961.

[8] W. Goldacker, A. Frank, A. Kudymow, R. Heller, A. Kling, S. Terzieva, and C. Schmidt, "Status of high transport current ROEBEL assembled coated conductor cables," *Superconductor Science Technology,* vol. 22, no. 3, p. 034003, 2009.

[9] M. Takayasu, J. Minervini, L. Bromberg, M. Rudziak, and T. Wong, "Investigation of twisted stacked-tape cable conductor," in *AIP Conference Proceedings*, 2012, vol. 1435, no. 1, pp. 273-280: AIP.

[10] J. Emanuelson and S. Pike. (1994). *Resistance vs. temperature and persistent current in a ring*. Available: http://www.futurescience.com/manual/sc1000.html

[11] Superconductors.org. (1999). Available: http://www.superconductors.org/type1.htm

[12] A. A. Abrikosov, "On the magnetic properties of superconductors of the second group," *Sov. Phys. JETP,* vol. 5, pp. 1174-1182, 1957.

[13] B. N. Taylor, P. J. Mohr, and M. Douma, "The NIST Reference on constants, units, and uncertainty," 2007.

[14] B. Rosenstein and D. Li, "Ginzburg-Landau theory of type II superconductors in magnetic field," *Reviews of modern physics,* vol. 82, no. 1, p. 109, 2010.

[15] P. Anderson, "Theory of flux creep in hard superconductors," *Physical Review Letters,* vol. 9, no. 7, p. 309, 1962.

[16] B. Maiorov, S. Baily, H. Zhou, O. Ugurlu, J. Kennison, P. Dowden, T. Holesinger, S. Foltyn, and L. Civale, "Synergetic combination of different types of defect to optimize pinning landscape using BaZrO 3-doped YBa 2 Cu 3 O 7," *Nature materials,* vol. 8, no. 5, p. 398, 2009.

[17] M. H. Gharahcheshmeh, E. Galstyan, J. Kukunuru, R. Katta, G. Majkic, X.-F. Li, and V. Selvamanickam, "MOCVD of Heavily-Doped 25 mol.% Zr-Added (Gd, Y) Ba2Cu3O7− δ Coated Conductors," *IEEE Trans. Appl. Supercond,* vol. 27, no. 4, pp. 1-5, 2017.

[18] V. Selvamanickam, R. Mallick, X. Tao, Y. Yao, M. H. Gharahcheshmeh, A. Xu, Y. Zhang, E. Galstyan, and G. Majkic, "Improved flux pinning by prefabricated SnO2 nanowires embedded in epitaxial YBa2Cu3Ox superconducting thin film tapes," *Superconductor Science Technology,* vol. 29, no. 8, p. 085016, 2016.

[19] V. Selvamanickam, M. H. Gharahcheshmeh, A. Xu, Y. Zhang, and E. Galstyan, "Critical current density above 15 MA cm− 2 at 30 K, 3 T in 2.2 μm thick heavily-doped (Gd, Y) Ba2Cu3Ox superconductor tapes," *Superconductor Science Technology,* vol. 28, no. 7, p. 072002, 2015.

[20] E. Galstyan, M. H. Gharahcheshmeh, L. Delgado, A. Xu, G. Majkic, and V. Selvamanickam, "Microstructure characteristics of high lift factor MOCVD REBCO

coated conductors with high Zr content," *IEEE Transactions on Applied Superconductivity*, vol. 25, no. 3, pp. 1-5, 2015.

[21] V. Selvamanickam, M. H. Gharahcheshmeh, A. Xu, E. Galstyan, L. Delgado, and C. Cantoni, "High critical currents in heavily doped (Gd, Y) Ba2Cu3Ox superconductor tapes," *Applied Physics Letters*, vol. 106, no. 3, p. 032601, 2015.

[22] Wikipedia. (2019). *Timeline of superconducting materials*. Available: https://en.wikipedia.org/wiki/Superconductivity

[23] B. Matthias, T. Geballe, S. Geller, and E. Corenzwit, "Superconductivity of Nb 3 Sn," *Physical review letters*, vol. 95, no. 6, p. 1435, 1954.

[24] A. El Bindari and M. Litvak, "Upper Critical Field of Nb-Zr and Nb-Ti Alloys," *Journal of Applied Physics*, vol. 34, no. 9, pp. 2913-2913, 1963.

[25] T. Berlincourt and R. Hake, "Superconductivity at high magnetic fields," *Physical review letters*, vol. 131, no. 1, p. 140, 1963.

[26] H. Suhl, B. Matthias, and L. Walker, "Bardeen-Cooper-Schrieffer theory of superconductivity in the case of overlapping bands," *Physical Review Letters*, vol. 3, no. 12, p. 552, 1959.

[27] J. G. Bednorz and K. A. Müller, "Possible highT c superconductivity in the Ba− La− Cu− O system," *Zeitschrift für Physik B Condensed Matter*, vol. 64, no. 2, pp. 189-193, 1986.

[28] C. Barth, "High Temperature superconductor cable concepts for fusion magnets," vol. 7, 2013.

[29] T. Ishida, M. Nishikawa, Y. Fujita, S. Okayasu, M. Katagiri, K. Satoh, T. Yotsuya, H. Shimakage, S. Miki, and Z. Wang, "Superconducting MgB 2 thin film detector for neutrons," *Journal of Low Temperature Physics*, vol. 151, no. 3-4, pp. 1074-1079, 2008.

[30] M. Parizh, Y. Lvovsky, and M. Sumption, "Conductors for commercial MRI magnets beyond NbTi: requirements and challenges," *Superconductor Science Technology*, vol. 30, no. 1, p. 014007, 2016.

[31] H. Müller and T. Schneider, "Heat treatment of Nb3Sn conductors," *Cryogenics,* vol. 48, no. 7-8, pp. 323-330, 2008.

[32] S. Mukoyama, M. Yagi, M. Ichikawa, S. Torii, T. Takahashi, H. Suzuki, and K. Yasuda, "Experimental results of a 500 m HTS power cable field test," *IEEE Transactions on Applied Superconductivity,* vol. 17, no. 2, pp. 1680-1683, 2007.

[33] H. Weijers, U. Trociewitz, W. Markiewicz, J. Jiang, D. Myers, E. Hellstrom, A. Xu, J. Jaroszynski, P. Noyes, and Y. Viouchkov, "High field magnets with HTS conductors," *IEEE transactions on applied superconductivity,* vol. 20, no. 3, pp. 576-582, 2010.

[34] R. Gupta, M. Anerella, A. Ghosh, S. L. Lalitha, W. Sampson, J. Schmalzle, J. Kolonko, R. Scanlan, R. Weggel, and E. Willen, "Hybrid high-field cosine-theta accelerator magnet R&D with second-generation HTS," *IEEE Transactions on Applied Superconductivity,* vol. 25, no. 3, pp. 1-4, 2015.

[35] N. Bay and M. S. Nielsen, "Mechanical processing of Ag/BSCCO high temperature superconductor tape," *Journal of materials processing technology,* vol. 151, no. 1-3, pp. 18-26, 2004.

[36] C. Rosner, M. Walker, P. Haldar, and L. Motowidlo, "Status of HTS superconductors: Progress in improving trransport critical current densities in HTS Bi-223 tapes and coils," *Cryogenics,* vol. 32, no. 11, pp. 940-948, 1992.

[37] R. Job and M. Rosenberg, "Lower critical field, remanent magnetization and irreversibility line of ceramic (Bi, Pb)-2223-HTSC," *Physica C: Superconductivity,* vol. 172, no. 5-6, pp. 391-399, 1991.

[38] E. Hellstrom. (2014). *BSCCO (Bi-2212)*. Available: https://nationalmaglab.org/magnet-development/applied-superconductivity-center/research-areas/bscco

[39] J. L. Reeves, M. Polak, W. Zhang, E. E. Hellstrom, S. E. Babcock, D. C. Larbalestier, N. Inoue, and M. Okada, "Overpressure processing of Ag-sheathed Bi-2212 tapes," *IEEE transactions on applied superconductivity,* vol. 7, no. 2, pp. 1541-1543, 1997.

[40] Z. Fisk, J. Thompson, E. Zirngiebl, J. Smith, and S. Cheong, "Superconductivity of rare earth-barium-copper oxides," 1987.

[41] K. Verbist, O. Lebedev, M. Verhoeven, R. Winchern, A. Rijnders, D. Blank, F. Tafuri, H. Bender, and V. Tendeloo, "Microstructure of Josephson junctions in relation to their properties," *Superconductor science technology*, vol. 11, no. 1, p. 13, 1998.

[42] Wikipedia. *Yttrium barium copper oxide*. Available: https://en.wikipedia.org/wiki/Yttrium_barium_copper_oxide

[43] W. Yang, L. Zhou, Y. Feng, P. Zhang, S. Chen, M. Wu, C. Zhang, J. Wang, Z. Du, and F. Wang, "The grain-alignment and its effect on the levitation force of melt processed YBCO single-domained bulk superconductors," *Physica C: Superconductivity*, vol. 307, no. 3-4, pp. 271-276, 1998.

[44] A. Kursumovic, R. Tomov, R. Hühne, J. MacManus-Driscoll, B. Glowacki, and J. Evetts, "Hybrid liquid phase epitaxy processes for YBa2Cu3O7 film growth," *Superconductor Science Technology*, vol. 17, no. 10, p. 1215, 2004.

[45] SuperPower, "Configuration of SuperPower® 2G HTS Wire."

[46] Y. Xu and D. Shi, "A review of coated conductor development," *Tsinghua science technology*, vol. 8, no. 3, pp. 342-369, 2003.

[47] J. M. Phillips, "Substrate selection for high-temperature superconducting thin films," *Journal of Applied Physics*, vol. 79, no. 4, pp. 1829-1848, 1996.

[48] Y. Yamada, Y. Yamada, and T. Ohkuma, "Bending characteristics of RE123 wires," *Teion Kogaku*, vol. 46, no. 5, pp. 246-253, 2011.

[49] A. Sundaram, Y. Zhang, A. Knoll, D. Abraimov, P. Brownsey, M. Kasahara, G. Carota, R. Nakasaki, J. Cameron, and G. Schwab, "2G HTS wires made on 30 µm thick Hastelloy substrate," *Superconductor Science Technology*, vol. 29, no. 10, p. 104007, 2016.

[50] X. Xiong, K. P. Lenseth, J. L. Reeves, A. Rar, Y. Qiao, R. M. Schmidt, Y. Chen, Y. Li, Y.-Y. Xie, and V. Selvamanickam, "High throughput processing of long-length IBAD MgO

and epi-buffer templates at SuperPower," *IEEE Transactions on Applied Superconductivity,* vol. 17, no. 2, pp. 3375-3378, 2007.

[51] J. Groves, P. Arendt, S. Foltyn, Q. Jia, T. Holesinger, L. Emmert, R. DePaula, P. Dowden, and L. Stan, "Improvement of IBAD MgO template layers on metallic substrates for YBCO HTS deposition," *IEEE transactions on applied superconductivity,* vol. 13, no. 2, pp. 2651-2654, 2003.

[52] C. Wang, K. Do, M. Beasley, T. Geballe, and R. Hammond, "Deposition of in-plane textured MgO on amorphous Si 3 N 4 substrates by ion-beam-assisted deposition and comparisons with ion-beam-assisted deposited yttria-stabilized-zirconia," *Applied Physics Letters,* vol. 71, no. 20, pp. 2955-2957, 1997.

[53] P. N. Arendt and S. R. Foltyn, "Biaxially textured IBAD-MgO templates for YBCO-coated conductors," *MRS bulletin,* vol. 29, no. 8, pp. 543-550, 2004.

[54] A. Goyal, M. P. Paranthaman, and U. Schoop, "The RABiTS approach: Using rolling-assisted biaxially textured substrates for high-performance YBCO superconductors," *MRS bulletin,* vol. 29, no. 8, pp. 552-561, 2004.

[55] V. Selvamanickam, Y. Xie, J. Reeves, and Y. Chen, "MOCVD-based YBCO-coated conductors," *MRS bulletin,* vol. 29, no. 8, pp. 579-582, 2004.

[56] D. W. Hazelton, V. Selvamanickam, J. M. Duval, D. C. Larbalestier, W. D. Markiewicz, H. W. Weijers, and R. L. Holtz, "Recent developments in 2G HTS coil technology," *IEEE Transactions on Applied Superconductivity,* vol. 19, no. 3, pp. 2218-2222, 2009.

[57] H. Yamada, H. Yamasaki, K. Develos-Bagarinao, Y. Nakagawa, Y. Mawatari, J. Nie, H. Obara, and S. Kosaka, "Flux pinning centres correlated along the c-axis in PLD-YBCO films," *Superconductor Science Technology,* vol. 17, no. 1, p. 58, 2003.

[58] T. F. Lehner. (2013). *Production of 2G HTS Conductor at SuperPower: progress and Ongoing Improvements*. Available: http://www.superpower-inc.com/system/files/2013_0312+MEM13_SP_FINAL_Web+Ver.pdf

[59] S. Oh, H. Kim, H. Ha, R. Ko, D. Ha, H. Lee, S. Moon, and S. Yoo, "Progress in research and development for REBCO coated conductors by reactive co-evaporation," *Progress in Superconductivity Cryogenics,* vol. 15, no. 4, pp. 1-5, 2013.

[60] V. Selvamanickam, Y. Yao, Y. Chen, T. Shi, Y. Liu, N. Khatri, J. Liu, C. Lei, E. Galstyan, and G. Majkic, "The low-temperature, high-magnetic-field critical current characteristics of Zr-added (Gd, Y) Ba2Cu3Ox superconducting tapes," *Superconductor Science Technology,* vol. 25, no. 12, p. 125013, 2012.

[61] G. Majkic, R. Pratap, A. Xu, E. Galstyan, H. C. Higley, S. O. Prestemon, X. Wang, D. Abraimov, J. Jaroszynski, and V. Selvamanickam, "Engineering current density over 5 kA mm− 2 at 4.2 K, 14 T in thick film REBCO tapes," *Superconductor Science Technology,* vol. 31, no. 10, p. 10LT01, 2018.

[62] G. Janeschitz, R. Heller, W. Fietz, W. Goldacker, G. Kotzyba, R. Lietzow, R. Nast, B. Obst, S. Schlachter, and C. Schmidt, "High temperature superconductors for future fusion magnet systems–status, prospects and challenges," in *21st IAEA Fusion Eng. Conf., Chengdu, China*, 2006, vol. 16, no. 21, p. 10.2006: Citeseer.

[63] Y. Sutoh, K. Kakimoto, N. Kaneko, Y. Iijima, and T. Saitoh, "Mechanical bending property of YBCO coated conductor by IBAD/PLD," *Physica C: Superconductivity and its applications,* vol. 426, pp. 933-937, 2005.

[64] M. Sugano, S. Machiya, M. Sato, T. Koganezawa, K. Shikimachi, N. Hirano, and S. Nagaya, "Bending strain analysis considering a shift of the neutral axis for YBCO coated conductors with and without a Cu stabilizing layer," *Superconductor Science Technology,* vol. 24, no. 7, p. 075019, 2011.

[65] L. Roebel, "Electrical conductor," ed: U.S. Patent No. 1,144,252, 1915.

[66] W. Goldacker, R. Nast, G. Kotzyba, S. Schlachter, A. Frank, B. Ringsdorf, C. Schmidt, and P. Komarek, "High current DyBCO-ROEBEL assembled coated conductor (RACC)," in *Journal of Physics: Conference Series*, 2006, vol. 43, no. 1, p. 901: IOP Publishing.

[67] CERN. (2015). *A luminous future for the LHC*. Available: https://cerncourier.com/a-luminous-future-for-the-lhc/

[68] W. Goldacker, F. Grilli, E. Pardo, A. Kario, S. I. Schlachter, and M. Vojenčiak, "Roebel cables from REBCO coated conductors: a one-century-old concept for the superconductivity of the future," *Superconductor Science Technology*, vol. 27, no. 9, p. 093001, 2014.

[69] C. Barth, K. Weiss, M. Vojenčiak, and S. Schlachter, "Electro-mechanical analysis of Roebel cables with different geometries," *Superconductor Science Technology*, vol. 25, no. 2, p. 025007, 2011.

[70] J. Fleiter, A. Ballarino, L. Bottura, and P. Tixador, "Electrical characterization of RE-123 Roebel cable," (in English), *Superconductor Science Technology*, vol. 26, p. 065014, 2013 2013.

[71] W. Goldacker. (2015). *HTS Roebel Cable Research from KIT and Partners*. Available: http://snf.ieeecsc.org/abstracts/crp59-hts-roebel-cable-research-kit-and-partners

[72] M. Takayasu, L. Chiesa, L. Bromberg, and J. V. Minervini, "HTS twisted stacked-tape cable conductor," *Superconductor Science Technology*, vol. 25, no. 1, p. 014011, 2011.

[73] M. Takayasu. (2014). *Development of REBCO Twisted Stacked-Tape Cables for Magnet Application*. Available: https://indico.cern.ch/event/308828/contributions/1680713/attachments/589814/811821/WAMHTS-1_Takayasu.pdf

[74] V. Selvamanickam. (2005). *Progress in scale-up of 2G conductor at SuperPower*. Available: http://superpower-inc.com/files/T363+2005+DOE+Peer+Review+2G.pdf

[75] V. Selvamanickam, "Superconductor components," ed: US Patent 7,417,192, 2008.

[76] D. C. van der Laan, "YBa2Cu3O7− δ coated conductor cabling for low ac-loss and high-field magnet applications," *Superconductor Science Technology*, vol. 22, no. 6, p. 065013, 2009.

[77] D. C. van der Laan, P. D. Noyes, G. Miller, H. W. Weijers, and G. Willering, "Characterization of a high-temperature superconducting conductor on round core cables in magnetic fields up to 20 T," *Superconductor Science Technology,* vol. 26, no. 4, p. 045005, 2013.

[78] J. D. Weiss, T. Mulder, H. J. ten Kate, and D. C. van der Laan, "Introduction of CORC® wires: highly flexible, round high-temperature superconducting wires for magnet and power transmission applications," *Superconductor Science Technology,* vol. 30, no. 1, p. 014002, 2016.

[79] D. C. van der Laan, D. Abraimov, A. Polyanskii, D. C. Larbalestier, J. Douglas, R. Semerad, and M. Bauer, "Anisotropic in-plane reversible strain effect in Y0. 5Gd0. 5Ba2Cu3O7− δ coated conductors," *Superconductor Science Technology,* vol. 24, no. 11, p. 115010, 2011.

[80] T. Mulder, J. Weiss, D. van der Laan, M. Dhalle, and H. Ten Kate, "Development of ReBCO-CORC Wires With Current Densities of 400–600 A/mm 2 at 10 T and 4.2 K," *IEEE transactions on applied superconductivity,* vol. 28, no. 3, 2018.

[81] D. Meyer and R. Flasck, "A new configuration for a dipole magnet for use in high energy physics applications," 1970.

[82] S. Caspi, D. Dietderich, P. Ferracin, N. Finney, M. Fuery, S. Gourlay, and A. Hafalia, "Design, fabrication, and test of a superconducting dipole magnet based on tilted solenoids," *IEEE Transactions on Applied Superconductivity,* vol. 17, no. 2, pp. 2266-2269, 2007.

[83] W. Wan, L. Brouwer, S. Caspi, S. Prestemon, A. Gerbershagen, J. M. Schippers, and D. Robin, "Alternating-gradient canted cosine theta superconducting magnets for future compact proton gantries," *Physical Review Special Topics-Accelerators Beams,* vol. 18, no. 10, p. 103501, 2015.

[84] X. Wang, S. Caspi, D. R. Dietderich, W. B. Ghiorso, S. A. Gourlay, H. C. Higley, A. Lin, S. O. Prestemon, D. van der Laan, and J. D. Weiss, "A viable dipole magnet concept with

REBCO CORC® wires and further development needs for high-field magnet applications," *Superconductor Science Technology,* vol. 31, no. 4, p. 045007, 2018.

[85] K. Mehta, P. Mukhopadhyay, R. Mandal, and A. Singh, "Mechanical properties anisotropy of cold-rolled and solution-annealed Ni-based Hastelloy C-276 alloy," *Metallurgical Materials Transactions A,* vol. 45, no. 8, pp. 3493-3504, 2014.

[86] X.-F. Li, A. B. Yahia, G. Majkic, M. Kochat, S. Kar, and V. Selvamanickam, "Reel-To-Reel Critical Current Measurement of REBCO Coated Conductors," *IEEE Transactions on Applied Superconductivity,* vol. 27, no. 4, pp. 1-5, 2017.

[87] X.-F. Li, A. B. Yahia, G. Majkic, and V. Selvamanickam, "Scanning hall probe microscopy on laser striated multifilament coated conductor," *IEEE transactions on applied superconductivity,* vol. 3, no. 25, pp. 1-4, 2015.

[88] X.-F. Li, M. Kochat, G. Majkic, and V. Selvamanickam, "Critical current density measurement of striated multifilament-coated conductors using a scanning Hall probe microscope," *Superconductor Science Technology,* vol. 29, no. 8, p. 085014, 2016.

[89] W. Luo, S. Kar, A. Xu, X. Li, A. B. Yahia, and V. Selvamanickam, "Fabrication and Electromagnetic Characterization of Ultrasmall Diameter REBCO Wires," *IEEE Transactions on Applied Superconductivity,* vol. 27, no. 4, pp. 1-5, 2017.

[90] W. Luo, S. Kar, X. Li, E. Galstyan, M. Kochat, J. S. Sandra, J. Jaroszynski, D. Abraimov, and V. Selvamanickam, "Superior critical current of Symmetric Tape Round (STAR) REBCO wires in ultra-high background fields up to 31.2 T," *Superconductor Science Technology,* vol. 31, no. 12, p. 12LT01, 2018.

[91] J. Lu, E. Choi, and H. Zhou, "Physical properties of Hastelloy® C-276™ at cryogenic temperatures," *Journal of applied physics,* vol. 103, no. 6, p. 064908, 2008.

[92] X. Cai, "Solution Fabrication for Multifilamentary tapes of the Second Generation High-Temperature Superconductor," 2016.

[93] F. C. Strong, "Faraday's laws in one equation," *Journal of Chemical Education*, vol. 38, no. 2, p. 98, 1961.

[94] D. Gabe, M. Li, and Z. Ding, "Conductivity of acid zinc and copper plating solutions," *Transactions of the IMF*, vol. 89, no. 2, pp. 76-79, 2011.

[95] G. Willering, D. van der Laan, H. Weijers, P. Noyes, G. Miller, and Y. Viouchkov, "Effect of variations in terminal contact resistances on the current distribution in high-temperature superconducting cables," *Superconductor Science Technology*, vol. 28, no. 3, p. 035001, 2015.

[96] H.-S. Shin and M. J. Dedicatoria, "Intrinsic strain effect on critical current in Cu-stabilized GdBCO coated conductor tapes with different substrates," *Superconductor Science Technology*, vol. 26, no. 5, p. 055005, 2013.

[97] S. Kar, W. Luo, and V. Selvamanickam, "Ultra-small diameter round REBCO wire with robust mechanical properties," *IEEE Trans. Appl. Supercond*, vol. 27, no. 4, p. 6603204, 2017.

[98] S. Kar, W. Luo, A. B. Yahia, X. Li, G. Majkic, and V. Selvamanickam, "Symmetric tape round REBCO wire with J e (4.2 K, 15 T) beyond 450 A mm− 2 at 15 mm bend radius: a viable candidate for future compact accelerator magnet applications," *Superconductor Science Technology*, vol. 31, no. 4, p. 04LT01, 2018.

[99] N. Tang, "Plastic-deformation analysis in tube bending," *International Journal of Pressure Vessels Piping*, vol. 77, no. 12, pp. 751-759, 2000.

[100] R. Agarwal, "Tube bending with axial pull and internal pressure," Texas A&M University, 2004.

[101] M. Miura, T. Kato, M. Yoshizumi, Y. Yamada, T. Izumi, T. Hirayama, and Y. Shiohara, "Rare earth substitution effects and magnetic field dependence of critical current in Y1-xRExBa2Cu3Oy coated conductors with nanoparticles (RE= Sm, Gd)," *Applied physics express*, vol. 2, no. 2, p. 023002, 2009.

[102] W. Luo, S. Kar, X. Li, E. Galstyan, M. Kochat, J. S. Sandra, J. Jaroszynski, D. Abraimov, and V. Selvamanickam, "In-field performance of Symmetric Tape Round (STAR) REBCO wire at 4.2 K in magnetic fields up to 31.2 T," *IEEE Trans. Appl. Supercond,* vol. Pending, 2018.

[103] J. Lu, R. Goddard, K. Han, and S. Hahn, "Contact resistance between two REBCO tapes under load and load cycles," *Superconductor Science Technology,* vol. 30, no. 4, p. 045005, 2017.

[104] N. Bagrets, A. Augieri, G. Celentano, G. Tomassetti, K.-P. Weiss, and A. della Corte, "Investigation of ReBCO conductor tape joints for superconducting applications," *IEEE Transactions on Applied Superconductivity,* vol. 25, no. 3, pp. 1-5, 2015.

[105] H.-S. Shin, A. Nisay, M. B. de Leon, and M. J. Dedicatoria, "Joining of REBCO coated conductor tapes using ultrasonic welding method," *IEEE Trans. Appl. Supercond,* vol. 25, no. 3, p. 1, 2015.